8-1-2015

Laser Ablation ICP-MS of Actinide Oxides as Simulated Used Nuclear Fuels

Keri Campbell
University of Nevada, Las Vegas, campb262@unlv.nevada.edu

LASER ABLATION ICP-MS OF ACTINIDE OXIDES AS SIMULATED USED NUCLEAR FUELS

By

Keri Rachel Campbell

Bachelors of Science in Chemistry

University of Nevada, Las Vegas

2009

A dissertation submitted in partial fulfillment of the requirements for the

Doctor of Philosophy – Radiochemistry

Department of Chemistry

College of Sciences

The Graduate College

University of Nevada, Las Vegas

August 2015

UNLV | GRADUATE COLLEGE

Dissertation Approval

The Graduate College
The University of Nevada, Las Vegas

April 27, 2015

This dissertation prepared by

Keri Rachel Campbell

entitled

Laser Ablation ICP-MS of Actinide Oxides as Simulated Used Nuclear Fuel.

is approved in partial fulfillment of the requirements for the degree of

Doctor of Philosophy - Radiochemistry
Department of Chemistry and Biochemistry

Kenneth R. Czerwinski, Ph.D.
Examination Committee Chair

Kathryn Hausbeck Korgan, Ph.D.
Graduate College Interim Dean

Patricia Pavier, Ph.D.
Examination Committee Member

Peter Stark, Ph.D.
Examination Committee Member

Gary Cerefice, Ph.D.
Examination Committee Member

William Culbreth, Ph.D.
Graduate College Faculty Representative

ABSTRACT

Laser Ablation ICP-MS of Actinide Oxides as Simulated Used Nuclear Fuel

By

Keri Rachel Campbell

Dr. Ken Czerwinski, Examination Committee Chair
Professor of Radiochemistry
University of Nevada, Las Vegas

The ability to examine elemental and isotopic ratios of fuels, waste forms, and other solids by direct analysis using laser ablation techniques can greatly reduce analysis costs and time. This is particularly true for actinide elements, as they contain useful information of the fuel cycle and nuclear forensics. Current methods to evaluate the composition of used fuel include a lengthy process of digestion, separations and often require multiple techniques and sample preparations to determine the elemental and isotopic composition. Furthermore all spatial information is lost during the digestion process, eliminating potentially useful data for detailed analysis. The goal of this project is to develop and optimize laser ablation inductively coupled mass spectrometry (LA-ICP-MS) for the analysis of fuel, used fuel and waste forms. This work focuses on uranium oxide simulated used nuclear fuels starting with binary systems of $(U,Pu)O_2$, $(U,Np)O_2$, $(U,Ce)O_2$ and $(U,Zr)O_2$. Methodology was successful in observing linearity of 0.995 and greater for these systems. This was achieved by

minimizing the particle size distribution of the aerosol and in turn decreases the time-dependent fractionation often observed in LA-ICP-MS.

The project is composed of four tasks. The first task is to prepare and characterize actinide matrices and standards. The characterization includes physical, thermodynamic, and chemical properties of the materials prepared. The second task is to develop methods for the analysis of actinide oxide materials using LA-ICP-MS evaluating the technique for: limit of detection, accuracy, and precision. The third task is to examine the ablation zone for any chemical or physical changes in the material to determine how destructive the technique is to the material. The final task is to develop a model to correlate the ablation behavior of the elements tested with physical and thermodynamic properties of the materials. The heat capacity of the materials was measured to determine trends with thermodynamic properties of the desired elements. The model will be a useful tool in determining laser power densities of the materials of interest.

This work is funded through Department of Energy National Nuclear Security Administration DE-NA0000979

ACKNOWLEDGEMENTS

First I would like to thank my advisor, Ken Czerwinski. Ken is an extraordinary teacher and mentor with tenacity and perseverance I hope to attain one day. He has encouraged me to succeed a task at times I thought was a fool's errand. I cannot express how thankful I am that Patricia Paviet and my paths crossed. Patricia helped me find my passion of Radiochemistry and saw potential in me as an undergraduate. She has been an inspiration in my life and a true friend. I cannot forget Julie Bertoia, who spent countless hours with me over the years troubleshooting the equipment. She kept me sane through the years and I will miss all our time in the bat cave.

I would like to thank Bill Kerlin for helping with the neptunium synthesis, Dan Koury for helping with analysis on the SEM, and Thomas Hartmann for countless hours helping with powder XRD analysis. Without the help of these great scientists, I would still be performing analysis and synthesis.

I would especially like to thank my husband, Charles Duncan. He has sacrificed much to support me to attain this degree and I love him with all my heart. I owe a debt of gratitude to my parents for their patience during my 15 year college career. I have been fortunate in my life to have an amazing support group of family and friends, with a list too long to thank them all here.

This work is dedicated to the most amazing person to ever walk this Earth, my Grandfather Linwood Wilkes Campbell (1911-2001). His love and admiration for nature inspired me to be a scientist.

TABLE OF CONTENTS

LIST OF TABLES

LIST OF FIGURES

LIST OF EQUATIONS

Chapter 1 – Introduction

1.1 Purpose

The ability to directly examine elemental and isotopic concentrations in nuclear fuels without dissolution of material is of interest to nuclear safeguards, nuclear forensics, the nuclear fuel cycle, and nuclear repository science. Nuclear safeguards, the emphasis of this work, are directed towards detecting the diversion of special nuclear materials, specifically the fissile isotopes ^{233}U, ^{235}U and ^{239}Pu. This work will explore the use of laser ablation mass spectrometry as a tool for evaluating element and isotopic ratios in actinide containing matrices.

The International Atomic Energy Agency (IAEA) is an independent intergovernmental science and technology based organization that serves as the global focal point for nuclear cooperation. The IAEA's overall mission is to verify through inspections that comply with non-proliferation agreements to only use nuclear material and facilities for peaceful purposes. The IAEA safeguards program has two objectives. The first is to ensure no significant quantities of nuclear material are diverted from peaceful nuclear activities to manufacture weapons. The second is to detect any undeclared nuclear materials and activities of a country (1). The IAEA defines non-destructive assay (NDA) techniques as systems to verify, check and monitor nuclear materials without changing their physical or chemical properties (2). Non-destructive assay techniques that are

fast and reliable are important to determine the nature of the source material and provide decision makers with the necessary information to protect and serve the community at risk. Some of the IAEA approved NDA techniques are described in section 1.2.

The application of Laser Ablation Inductively Coupled Plasma Mass Spectrometry (LA-ICP-MS) for isotope ratio measurements is a rapid technique for direct solid sampling in analytical chemistry. The advantages of this technique include reduced risk of contamination by direct sample analysis, no chemical dissolution, and determination of spatial distributions of elemental compositions (3). Using LA-ICP-MS as a safeguard technique would minimize the number of steps in the handling process, maximizing throughput and turn-around time than current non-destructive assay techniques with the ability to determine isotopic and concentrations in a multitude of matrices. With the advancements since inception, such as type of laser and geometry of ablation cell, laser ablation has grown from a semi-qualitative technique to a semi-quantitative technique for bulk or local analysis with high spatial resolution of trace and isotopic analysis. This work explores the advantages and limitations of LA-ICP-MS to determine elemental and isotope ratios on matrices of interest to nuclear safeguards.

1.2 Current Safeguard Techniques

The IAEA uses more than 100 different NDA techniques, which range in size and implementation (2). The most widely used instrumentation is stand-off techniques detecting either γ or neutrons. The K-edge densitometer (KEDG) is the most accurate gamma detector that requires the plutonium concentration in the sample of interest above 50 g/L (2). Neutrons produced either by α particle interaction with light elements, spontaneous fission, or induced fission can provide signatures. The neutron detectors can have error in accuracy up to 1% for determining plutonium concentrations in fresh fuel. The neutron and gamma measurements do not require sample processing but often have significant data analysis to identify and quantify isotopes of interest. An additional downside with these detectors is not all of the isotopes of interest emit γ or neutrons. Often the systems are detecting daughter products emissions which are not direct measurements. All of these detectors vary in accuracy and precision.

Modern safeguards require destructive assay on a multitude of samples for quality control of analyte concentration and isotopics during fabrication and analysis of used nuclear fuel. Radioanalytical techniques for long-lived α- and β-emitting nuclides have time consuming digestion and separation procedures (4). Figure 1 displays a common flow sheet for destructive analysis. Alpha spectroscopy is the most common quantification technique to determine plutonium isotopes. Unfortunately, α-spectroscopy cannot routinely resolve

isotopes with similar decay energies, such as the pairs ^{239}Pu and ^{240}Pu and ^{238}Pu and ^{241}Am. These are isotopes of interest for mixed oxide fuel fabrication and recycling in used fuel and would need to be quantified (5).

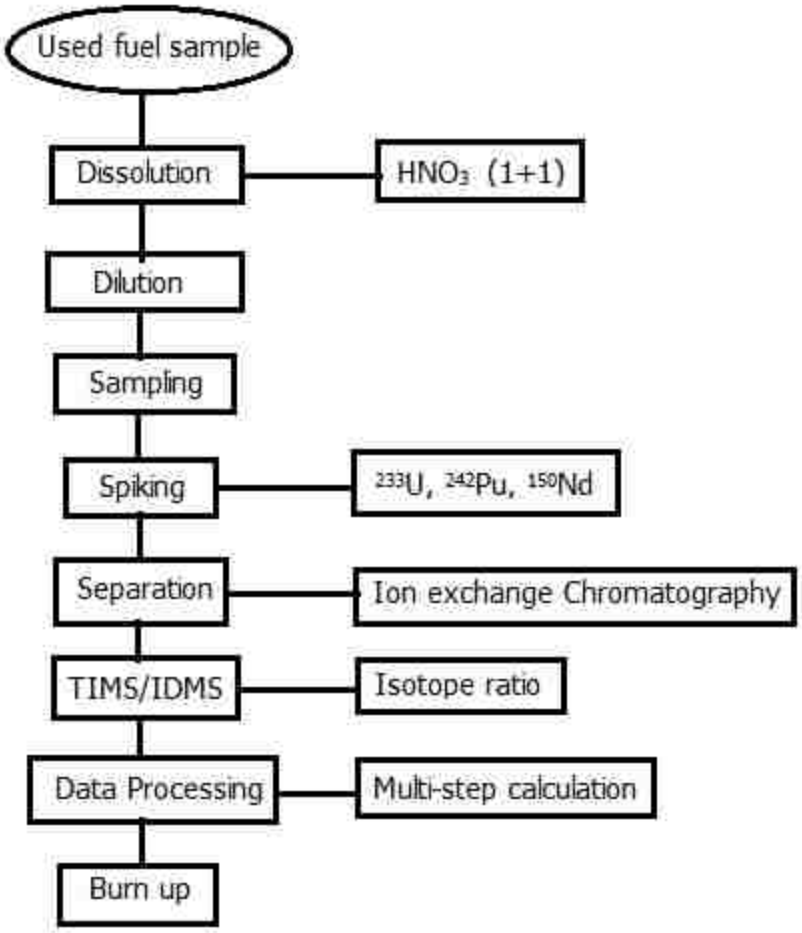

Figure 1: A common flow sheet for destructive analysis of used nuclear fuel (39)

1.3 Fresh and Used Fuel Composition

The most commonly used reactor is the light water moderated reactors (LWR) which use a uranium dioxide fuel (UO_2) enriched to 3-5% ^{235}U. Uranium oxide is a refractory material that is non-reactive with water (6). The light water moderated reactors can also burn mixed oxide (MOX) fuel which is a uranium oxide fuel with up to 5% plutonium oxide. The MOX fuel can only be 40% of the overall reactor core (7). The concentration of plutonium in MOX fuel needs to be quantified prior to use as well as the enrichment of ^{235}U in the uranium oxide fuel, and both values can be obtained using LA-ICP-MS. Uranium dioxide is known to form an extensive oxygen excess non-stoichiometric phase UO_{2+x} where x ranges from $0 \leq x \leq 0.05$ (8). The value of x greatly influences the thermodynamic properties and heat capacity of the material.

There are three main objectives for used fuel recycling: recover uranium and plutonium for re-use as fuel, remove fission products and reactor poisons, and convert the waste into a stable chemical form which is safe for long term storage (6). In these objectives, LA-ICP-MS can be used to quantify elements of interest prior to dissolving and separating the used fuel for the final composition of the waste form. In addition to providing the isotopic and elemental concentrations of the fuel, LA-ICP-MS can also provide spatial information for the elements of interest. The spatial information is of importance to fuel performance evaluations to determine if the accumulation of fission products is due to high

fission density areas or thermal gradient migration (51). Figure 2 shows the depth profile of uranium and plutonium at the outer pellet zone collected using x-ray microanalysis. The spatial information from this analysis is the accumulation of plutonium at the outer pellet zone indicative of a high fission density area. This analysis was performed using X-ray microanalysis techniques. The spatial information is of importance to fuel performance evaluations to determine if the accumulation of fission products is due to high fission density areas or thermal gradient migration (51).

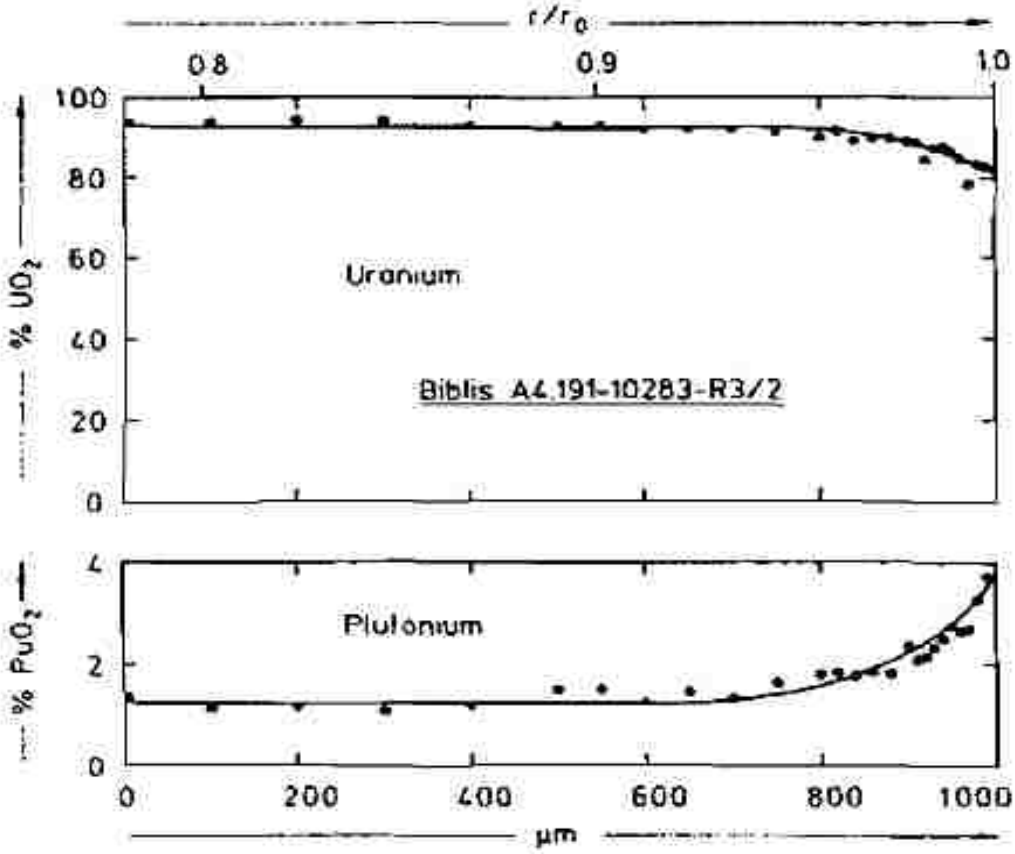

Figure 2: Uranium and plutonium concentrations in the surface region of a high burn-up oxide fuel pellet (51)

In LWR's only 3% of the uranium is fissioned before the fuel is removed from the core. The need to remove the fuel from the core is due to the loss of reactivity from increasing fission products, most notably the neutron absorbers or poisons which impact the thermal utilization factor (51). Neutron absorbers such as ^{135}Xe have a high neutron capture cross section and will impede the chain reaction needed for efficiency. The exact composition of the used fuel depends on the total burn-up, generally 95% of the used fuel is uranium dioxide and the remaining ~5% are fission products (6). The actinides from neptunium to einsteinium concentration range from 0.52 % to 1.48 % in burn-up rates from 13 MWd/kg to 65 MWd/kg. About 20% of the fission products are the noble gases krypton and xenon (9).These noble gases form closed intragranular and intergranular bubbles within the fuel. With increased burn-up, pores and grain boundaries are preferred sinks and form fission gas bubbles (10). These bubbles cause swelling and creep of the pellet resulting in possible fuel-cladding interactions which are undesirable for fuel performance.

Three main phases of the solid are found in the used fuel are listed in Table 1 (11). The main oxide matrix is considered as a solid solution where the fluorite structure is the most stable (12). The actinides, lanthanides, and zirconium in the main oxide phase are isomorphic substitutions in the fluorite structure. The secondary oxide, phase also known as the "grey phase", is formed because of miscibility limits within the main oxide phase (10). The miscibility limits are attributed mostly to barium, which only a small fraction of the barium

oxide forms a solid solution with the main oxide phase. The majority of barium is precipitated as a multi-component oxide called the grey phase. Zirconium dioxide has limited solubility in uranium dioxide which is dependent on temperature and extended by the presence of rare earth oxides in the main oxide phase (10). The metallic segregation phase, or Ɛ phase, is dependent on the oxygen potential of the fuel. The ruthenium, rhodium, palladium, molybdenum, and technetium form metallic precipitates in the grain boundaries and are the best indicators of burn-up rates since they have the highest linear correlation of concentration with burn-up (13).

Phase	Phase Composition
Main Oxide	Actinides, Lanthanides, Zr
Secondary Oxide	$(Ba,Sr)ZrO_3$
Metallic Segregations	Mo, Tc, Ru, Rh, Pd

Table 1: Three main phases found in LWR used fuel (10)

The concentrations of fission products depend on the type of reactor, fuel, and burn-up. Figure 3 relates elemental concentration of fission products with fuel burn-up rates of LWR UO_2 fuel. The fission product concentrations increase linearly as a function of burn-up, with Zr having the highest concentration of ~9 g/kg. The gold standard for determining burn-up is the ^{148}Nd reference method ASTM E321-69. This method is destructive analysis following the flow chart

shown in Figure 1. This isotope ^{148}Nd has ideal properties that classify it as a burn-up indicator: it is non-volatile and has no volatile precursors, it is non-radioactive and requires no decay corrections, it has good emission characteristics for mass analysis, its fission yields are nearly the same for ^{235}U and ^{239}Pu and is nearly independent of neutron energy (14).

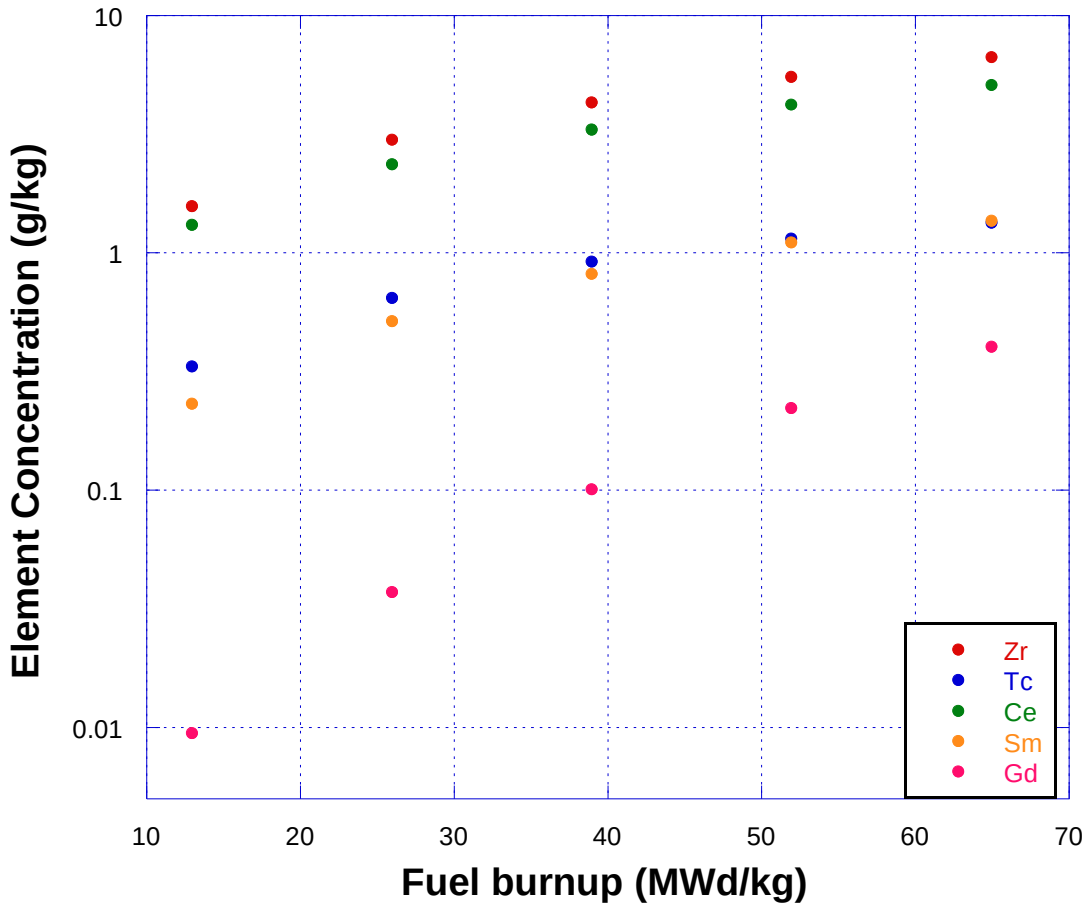

Figure 3: Elemental concentrations of fission products as a function of Fuel burn-up for LWR UO_2 fuel (15)

Used fuel analysis is of importance to nuclear safeguards because the analysis of the burn-up rates indicates whether the reactor is producing weapon grade plutonium. Figure 4 shows the calculation of plutonium isotope ratios as a function of irradiation time at a power level of 37.5 MW_t/t in a BWR fueled with uranium enriched to 3.2% in ^{235}U. Nominally the $^{240}Pu/^{239}Pu$ ratio is between 0.05 and 0.07 for weapon production (15). If the reactor is being used for peaceful means, such as energy, the plutonium isotopic ratio is not ideal for weapon production and the total burn-up tends to be above 40 MWd/kg.

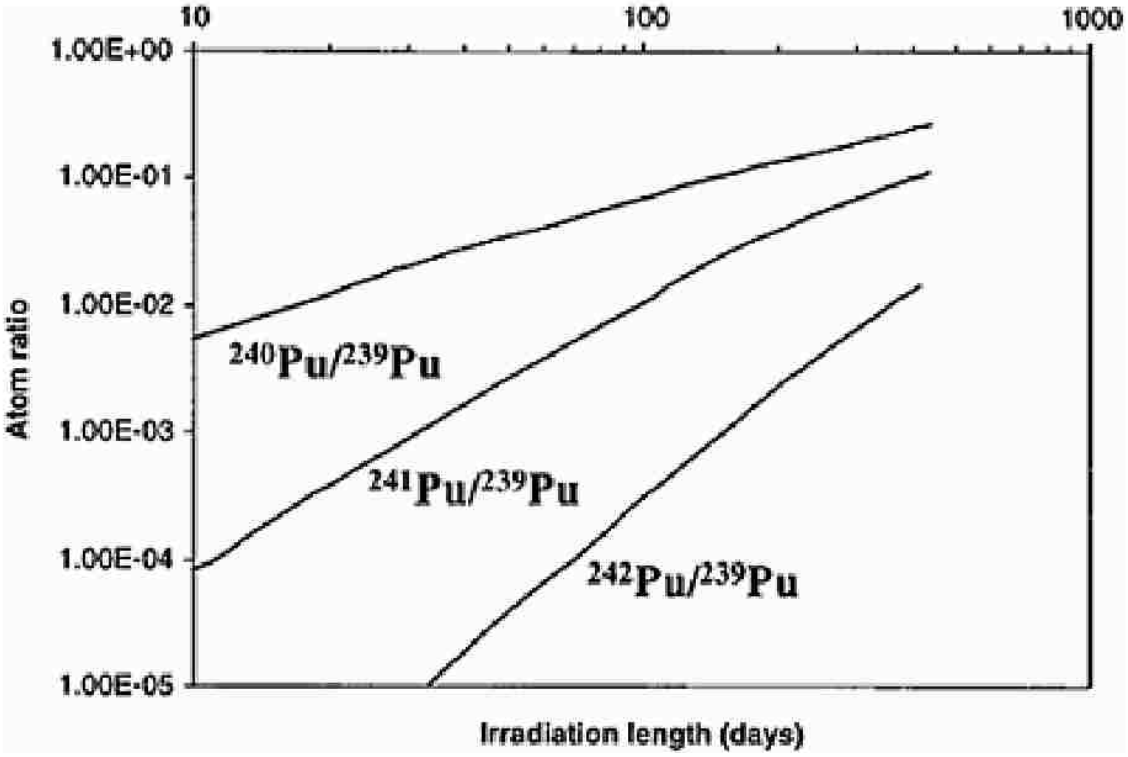

Figure 4: ORIGEN2 calculation of the indicated Pu isotope ratios as a function of irradiation time, at a power level of 37.5 MW_t/t in a BWR fueled with U enriched to 3.2% in ^{235}U (15).

1.4 Goals and Objectives

The goal of this project is to develop and optimize laser ablation inductively coupled mass spectroscopy techniques for the analysis of elemental and isotopic ratios in nuclear fuel, used nuclear fuel, and nuclear waste forms. In order to reach this goal, the oxide materials and standards will be prepared and characterized. Routes and techniques used in the material preparation will be provided. The characterization will include physical, thermodynamic, and chemical properties of the materials prepared. The methods developed for the LA-ICP-MS analysis will be evaluated for limit of detection, accuracy, and precision. The ablation zone will then be examined for any chemical or physical changes in the material to determine how destructive the technique is to the material. Lastly, a model will be developed to correlate the ablation behavior of the elements tested with physical and thermodynamic properties of the materials.

The first task will be to prepare actinide oxide materials as standards for LA-ICP-MS. These materials will be binary oxides consisting of bulk uranium with trace amounts of zirconium, cerium, neptunium and plutonium to provide fundamental information and best model used nuclear fuel. More complex materials such as a ternary oxide matrix of bulk uranium with zirconium and cerium will also be evaluated to determine if multiple elements with different ablation behaviors can be measured simultaneously. The physical properties of

the materials characterized include percent theoretical density and grain sizes. The materials heat capacity will be measured for characterization of thermodynamic properties. Lastly, the phase compositions of the materials will be characterized.

The second task is determining the limit of detection (LOD), accuracy, and precision for the LA-ICP-MS methods developed as well as any limitations of this technique. These parameters are important to understand in order to implement this method in nuclear safeguards, forensics, or the fuel cycle. Each area has different limitations and criteria for LOD, accuracy, and precision and different criteria for destructive and non-destructive assay.

The third task is to examine the ablation zone for any chemical or physical changes in the material to determine perturbations due to measurement. This study will classify the destructive level of the technique and determine where it could be best implemented as an analysis method. If the technique is minimally non-destructive, it could be used to determine the plutonium concentration in MOX fuel before irradiation. On the other hand, if it is destructive, then the technique would be better applied to safeguards to assist in determining used fuel burn-up rates, which can be indicative of weapons production.

The final task is to develop a model to correlate the ablation behavior of the elements tested with physical and thermodynamic properties of the materials. The heat capacity of the materials will be measured to determine trends with thermodynamic properties of the desired elements. If trends are established,

then the model will be a useful tool in determining laser power densities of the materials of interest.

Chapter 2 – Instrumentation and Methods

2.1 Synthesis of Materials

The pellets were prepared by dissolving the nitrate salts of the metals of interest: uranium, plutonium, neptunium, cerium, and zirconium in de-ionized water. All chemicals used are reagent grade obtained from Sigma-Aldrich except the actinides. The plutonium was obtained from Eckert and Ziegler Isotope Products. The neptunium was donated from Pacific Northwest National Laboratory in the form of a mixed metal and oxide. The uranium was purchased from J.T. Baker Laboratories as uranyl nitrate.

The metal ions are precipitated in a 50 mL centrifuge tube as oxy-hydroxides using concentrated ammonium hydroxide saturated in oxalate. The uranium is precipitated as ammonium diuranate ($(NH_4)_2U_2O_7$) under these conditions. The sample is vortexed for two minutes to ensure all the metals are in contact with the ammonium hydroxide solution, then centrifuged for five minutes. The supernatant is decanted from the precipitate. The process is then repeated with the supernatant to ensure all metals are precipitated. The precipitate was dried overnight at 100 °C or freeze-dried depending on the matrices.

The dried precipitate is then transferred in to a ceramic crucible and calcined at 600 °C for 12 hours. During the calcination process the oxy-hydroxides are converted to oxides. With these furnace conditions under air

atmosphere uranium forms U_3O_8. After calcination the precipitate was ball milled at 450 rpm for 5 minutes to obtain fine powders. The powders were reduced to MO_2 at 600 °C with Ar/5% H_2 gas in a clamshell furnace. The powder was mixed with 1% by weight zinc stearate binder and pressed using a Carver manual press. The pellets were cold pressed in a 6 mm steal die for 2 minutes with a load of about 350 MPa. The pellets were sintered at 1700 °C for 5 hours under reducing atmosphere (Ar/5% H_2) in a sealed corundum tube. The ramp rates were designated by the furnace manufacturer as 4.5 °C/min and held at 500 °C for 2 hours to burn off the zinc stearate binder. The 4.5 °C/min rate continued up to 1600 °C. From 1600-1700 °C the ramp rate was 2 °C/min. The cool down temperatures mirrored the ramping temperatures except for the hold at 500 °C.

2.2 Instrumentation

2.2.1 Powder X-ray Diffractometer

The chemical homogeneity of the material was characterized using a Bruker D8 Advance powder x-ray diffractometer (powder XRD). The powder XRD has been shown to identify crystalline phases present within a sample. The lattice parameters will determine whether the crystalline structures within the samples are in thermodynamic equilibrium. Two methods were used to prepare sintered pellets for measurement. To avoid grinding, the $(U,Pu)O_2$ and $(U,Np)O_2$ pellets were measured in entirety by mounting the pellet on clay in a depressed

sample holder. The remaining matrices were ground to a powder and spread in a thin layer over a low-background single crystal silicon wafer sample holder using acetone. Patterns were taken using 40 mV and 40 mA from 10 to 120 °2θ with a step size of either 0.008 or 0.01 °2θ depending on the peak shapes of the pattern. Bruker TOPAS 4.2 was then used to perform the Rietveld structure refinement. Inorganic Crystal Structure Database was used to input the structure parameters. Instrument parameters are listed in Table 2.

Parameter	**Value**
Primary radius	435 mm
Secondary radius	217.5 mm
Linear PSD 2Th angular range	3°
FDS angle	1°
Axial Convolution	Full
Filament length	12 mm
Sample length	5 mm
Receiving slit length	12 mm
Primary Sollers	2.3°
Secondary sollers	2.5°

Table 2: Powder XRD parameters

2.2.2 Laser Ablation Inductively Couple Mass Spectrometry

A Nd:YAG ultraviolet laser system at 266 nm (LSX-500, CETAC, Omaha, NE) was used to generate pulses of < 6 nsec duration. The laser radiation was focused onto the surface of the pellet positioned inside a cylindrical ablation cell

with a volume of 110 cm^3. Aerosols were transported under argon atmosphere and their composition measured with a quadrupole ICP-MS (ELAN DRC II, Perkin-Elmer, Waltham, MT).

Prior to analysis the ICP-MS parameters were optimized by measuring a NIST 610 glass standard until the ^{208}Pb:^{206}Pb ratio is 2.167 ± 0.0018 (16). The laser ablation parameters were optimized by varying the spot size, scan rate, laser power and pulse repetition rate until the signal profile was plateau shaped with deviations of the signal spikes less than 1000 counts. The nebulizer flow rate was then varied until the tailing of the signal was minimized. The signal was then integrated and normalized for time of integration. The parameters used in each study will be discussed in detail in subsequent chapters. The mechanics of LA-ICP-MS is discussed in section 3.1. The optimization of the system will be discussed in Chapter 4.

2.2.3 Scanning Electron Microscope (SEM) and Optical Microscopy

In order for bulk analysis using LA-ICP-MS to be successful the material of interest needs to be physically and chemically homogeneous on the tens of microns level (17). The grain size distribution and surface defects were measured using a Leica DM 2500P microscope to the 1 micron scale. The pellet is mounted onto a microscope slide using clay.

A JEOL-5610 scanning electron microscope (SEM) equipped with a secondary electron and backscatter electron detectors is also used to measure surface defects and post ablation features of the pellets. The SEM uses an electron beam to image the surface microstructure with magnification of 40 to 5000 times. The pellets are mounted onto the sample stage using double sided carbon tape. After mounting the sample is sputter coated using a Denton Vacuum DV-502A carbon coater to avoid charging on the surface. Non-conductive materials, such as uranium oxide, need to be carbon coated so the electron beam interacts with the carbon rather than the non-conductive surface. The SEM also has the capability to measure elemental analysis through energy-dispersive x-ray emission spectroscopy (EDS) using INCA mapping software. INCA is a measurement, calibration and diagnostic software published by Engineering Tools, Application and Services. The accelerating voltage used is 15 kV with a working distance of 20 mm. For the EDS analysis, x-ray energies of 0-10 keV were detected for elemental mapping. Surface images were collected in both secondary electron imaging and back scatter imaging modes.

2.2.4 Physical Property Measurement System (PPMS)

A quantum design model 6000 PPMS was used to determine the heat capacity of the materials. Heat capacity is defined as the amount of heat required to change a substance temperature one degree in the units J $°C^{-1}$. This

system measures the heat capacity (C_p) of the material at constant pressure, the general equation shown below where C_p is a path function of heat energy transferred (dQ) to an object and the increase of temperature of the object (dT).

$$C_p = \left(\frac{dQ}{dT}\right)_p$$

Equation 1: Heat Capacity at constant pressure

The PPMS Cryopump High-Vacuum pumps helium gas from a dewar to the PPMS sample chamber. The system is able to achieve thermal isolation for measurement when the base pressure is near 0.1 mTorr. Using a heat capacity puck (shown in Figure 5), the sample is mounted using cryogenic grease on a microcalorimeter platform. The platform is suspended by eight thin wires that serve as electrical leads for a thermometer and an embedded heater. The sample platform temperature is monitored throughout the heating and cooling process providing the raw data for the heat capacity measurements.

Figure 5: Image of heat capacity sample puck

The sintered pellets are broken into small pieces using a mortar and pestle. The sample size for the PPMS ranges from 10-50 mg and needs a flat side to have complete contact with the thermal grease to ensure proper heating. An addenda is first collected with just the cryogenic grease and then another addenda is collected with the grease and sample of interest. The system is calibrated using a sapphire standard (Al_2O_3) weighing 18.6 mg. The heat capacity is measured from 2 K to 300 K.

The software uses two mathematical models to convert raw data to heat capacity in J $mol^{-1}K^{-1}$ depending on the thermal contact of the sample with the sample platform. The simple model assumes the platform and sample are in good thermal contact and are the same temperature during the measurement.

The temperature (T) of the platform as a function of time (t) adheres to the following equation:

$$C_{total}\frac{dT}{dt} = -K_w(T - T_b) + P(t)$$

Equation 2: Heat capacity equation for simple model

C_{total} is the total heat capacity of the sample and sample platform. The term K_w is the thermal conductance of the supporting wires. The term T_b is the temperature of the puck frame, and P(t) is the power applied by the heater. The heater power P(t) is equal to P_0 during the heating portion of the measurement and equal to zero during the cooling portion. The system uses a nonlinear least square fitting algorithm comparing the solution to Equation 2 to the actual measurement. The fit deviation is then used to determine the standard errors of the measurement.

The software uses a more complex two tau statistical model if the thermal contact between the sample and sample platform is poor. This model simulates the effect of heat flowing between the sample platform and sample, and between the sample platform and puck.

$$C_{platform}\frac{dT_p}{dt} = P(t) - K_w\big(T_p(t) - T_b\big) + K_g\big(T_s(t) - T_p(t)\big)$$

$$C_{sample}\frac{dT_s}{dt} = -K_g\big(T_s(t) - T_p(t)\big)$$

Equation 3: Heat capacity equations for two tau model

$C_{platform}$ is the heat capacity of the sample platform, C_{sample} is the heat capacity of the sample, and K_g is the thermal conductance between the two due to the grease. The respective temperatures of the platform and sample are given by $T_p(t)$ and $T_s(t)$. If the fit of the two tau method does not converge, then the simple model is used to determine heat capacity.

2.2.5 Liquid Scintillation Counting (LSC)

A Packard TriCarb 2700 TR liquid scintillation counter was used to determine the concentration of plutonium and neptunium in solution. A 10 µL sample is mixed with 10 mL of Ultima Gold AB scintillation cocktail and counted for 5 minutes. Background was subtracted manually by a blank sample.
The LSC detection method requires specific cocktails to absorb the energy emitted from radioactive decay into detectable light pulses. The scintillation cocktail contains a scintillator, an emulsifier, and a wave shifter (15). An emulsifier or surfactant is added to the scintillation cocktail to ensure sample homogeneity. The scintillator transfers the ionizing radiation's excitation energy to the solvent, and then transferred to the scintillation molecules. This mechanism allows each alpha or beta emission to result in a pulse of light. Since the photomultiplier tubes used for detection are more sensitive to longer wavelengths, the wave shifter is an organic compound that absorbs the primary scintillator's photons and then re-emits the photon at a longer wavelength.

2.2.6 Utraviolet-visible Spectroscopy

A Cary 6000i ultraviolet-visible (UV-vis) spectrophotometer was used to determine the oxidation state of neptunium in solution. A molecule containing Π-electrons or non-bonding electrons absorbs the light and excites the electrons to higher anti-bonding molecular orbital. The spectrum provides valuable information about speciation through the band structure (24). Ultraviolet radiation interacts with the outer electronic levels, promoting electrons to higher energy levels, so this region of the spectrum will yield information on the bonding of the atoms into molecules, and their oxidation state. Changes in oxidation states of species have large effects of the absorption spectra. Table 3 lists the absorption wavelengths of neptunium oxidation states in perchloric and nitric acid. Regardless of the acid media, the absorption band for Np(VI) does not change, Np(IV) and Np(V) absorption bands are strongly dependent on the solution.

Oxidation State	Solution	Wavelength (nm)	Intensity
Np(III)	2 M $HClO_4$	500-700	weak
Np(IV)	2 M $HClO_4$	~700, 950	strong
Np(V)	2 M $HClO_4$	950	strong
Np(VI)	2 M $HClO_4$	below 400	strong
Np(IV)	1-6 M HNO_3	715	strong
Np(V)	1-6 M HNO_3	617	weak
Np(VI)	1-6 M HNO_3	below 400	strong

Table 3: Absorption bands for different oxidation states of Np in $HClO_4$ and HNO_3 solutions (59,18)

UV-vis spectrophotometer measures the intensity of light passing through a sample (I), and compares it to the intensity of light before it passes through the sample (I_0). The ratio I/I_0 is called the transmittance and is usually expressed as a percentage (%T). The absorbance (A) is based on the transmittance in Equation 4 (24). The instrument provides the transmittance value. The instrument collects the spectrum from 300 nm to 1100 nm with a scan rate of 600 nm/min.

$$A = -log\left(\frac{\%T}{100\%}\right)$$

Equation 4: Relationship between Absorbance and Transmittance of light.

Chapter 3 – LA-ICP-MS Background

3.1 System Overview

Laser ablation as a sample introductory system for ICP-MS was first reported in 1985 (19). The system used a J.K. Type 2000 ruby laser with results demonstrating uniform sensitivity for mass range 7-238 m/z and saturation of the detection system. Since 1985 great achievements have been made in laser technology including high quality optical materials. The laser most commonly used in LA-ICP-MS is a neodymium-doped yttrium aluminum garnet (Nd:YAG) solid state laser with a fundamental frequency of 1064 nm quadrupled to 266 nm. Ablation cell design and the transport process were also investigated in the 1990s to improve the dispersion of the particulate plume in order to enhance sensitivity (20).

During laser sampling the surface is subjected to extremely high temperatures and pressures resulting in heating, melting and vaporization of the surface. Many mechanisms are used to describe mass removal of solids using laser ablation. Depending on the irradiance of the laser desorption, thermal vaporization, phase explosion and other mechanisms are proposed. If the irradiance is below 3×10^8 W/cm^2 desorption and thermal vaporization are the dominant processes (3). Desorption involves the material absorbing the laser light and in turn the upper layer of the material is vaporized and ionized. Thermal vaporization involves a high temperature plasma initiation above the

sample surface in which mass is removed from the surface as a particulate plume. The particulate plume consists of atoms, molecules, large particulates, and vapor. Some of the particles are swept to the ICP-MS by the carrier gas. The larger particulates (>2μm) in the plume then condense and fall to the surface of the material. Phase explosion is a process where the sample is heated beyond its boiling point and becomes a meta-stable liquid near its critical state. Phase explosion is identified as a significant increase in the ablated volume resulting in a larger void in the material referred to as a crater (21).

Parameters such as laser energy, pulse duration, wavelength and carrier gas flow significantly influence the sensitivity and precision of the measurement. Laser ablation is applicable to all types of materials whether they are conducting, non-conducting, pressed powder, metallic, ceramic or organic. The laser parameters used significantly change depending on the type of material (22). Certain physical and chemical properties of the examined matrix influence ablation such as sublimation point, density and thermal expansion coefficient, thermal conductivity, specific heat of vaporization and heat capacity (23).

Once the sample is ablated the particles travel through a transport tube by carrier gas flow to the ICP-MS torch (Figure 6). The torch consists of concentric quartz tubes surrounded by a water-cooled radio-frequency induction coil. A spark from a Tesla coil initiates ionization of the argon gas in the central tube, these ions and electrons then interact with fluctuating magnetic field produced by the induction coil. The outer tube gas flow is tangential which cools

the walls of the center tube and centers the plasma radially (24). A vacuum is applied to the system to inhibit interactions of the gas molecules before reaching the detector. Further atomization and excitation of the sample vapor occurs in the argon plasma, which is then transmitted through a water cooled nickel sampling cone with a small orifice. After the sampling cone the hot plasma gas is expanded and cooled and a small fraction is pumped through the skimmer cone. Once the gas passed through the skimmer cone, a negative voltage is applied which separates the positive ions from the electrons and molecular species. The positive ions are then accelerated, focused by a magnetic ion lens, and introduced into the quadrupole.

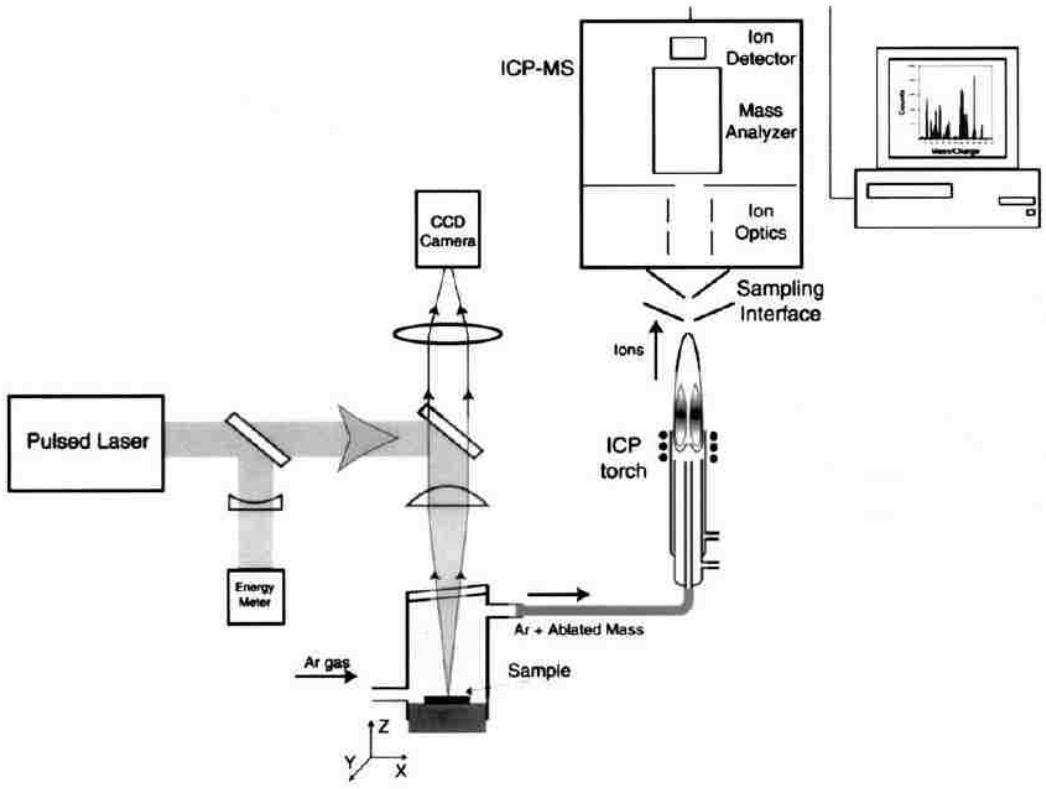

Figure 6: General LA-ICP-MS set-up (25)

The most common type of mass spectrometer used is the quadrupole mass analyzer shown in Figure 7. Four parallel cylindrical rods serve as electrodes. One pair is connected to a positive dc source while the other pair is a negative dc current. All rods are also in contact with an ac voltage 180° out of phase of each pair (24). The ions are then accelerated by a potential into the space between the rods. Two simple principles describe the trajectory and mass to charge (m/z) discrimination of the ions. The first is electrostatic interaction which is the attraction of the ion to the rod of opposing charge. The second principle uses the relation between kinetic energy and momentum, where the momentum of ions of equal kinetic energy is directly proportional to the square

root of mass of the ion. With these properties it is found that ions are either attracted or repelled while the current alternates in the rods and the ability for the ion to change trajectory depends on the mass of the ion. Once the ion interacts with a rod it is then neutralized and can no longer be detected. The positive rods attract the m/z less than the desired and the negative rods attract the m/z larger than the desired m/z. The remaining ion beam is then detected and the signal is collected.

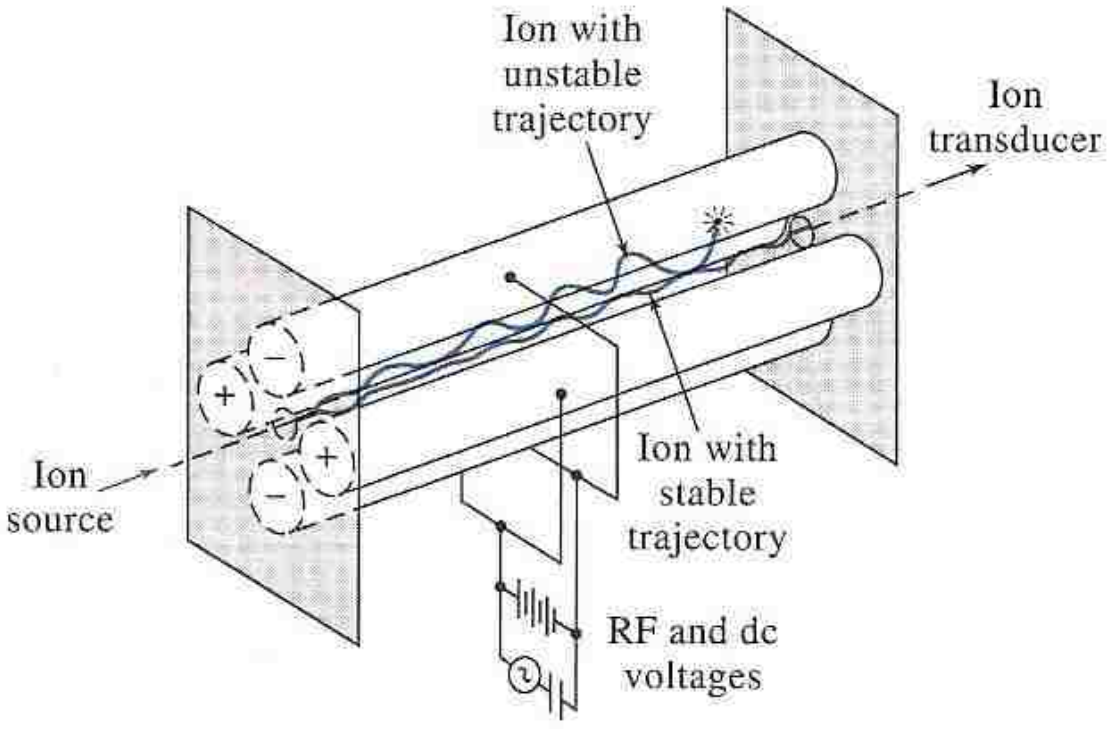

Figure 7: A quadrupole mass spectrometer (24)

3.2 Technical Issues with LA-ICP-MS

As in any analytical technique there are undesirable effects that must be understood and overcome in order to improve accuracy and precision of the measurement. With LA-ICP-MS such effects occur in the ablation, transport and detection processes. A major limitation is elemental fractionation which is the non-sample related variation of the analyte response during the ablation process (3). Preferential vaporization of elements from the sample and the possibility of the composition altering during transport can lead to deviations in analysis results with actual composition (3).

Particles of various sizes are generated during the ablation process which decrease the transport efficiency of the analytes and alter their signals. If a particle on the order of 1-1.5 μm enters the ICP its vaporization and excitation may be incomplete, resulting in a lower signal for the constituents still present as a particulate. Fractionation mainly occurs at the points of vaporization and ionization, ablation site and plasma torch, resulting in partial recondensation onto the sample surface or filtering of larger particles in the ion optics of the ICP-MS (22). The fractionation index is a measure of this time-dependent variation of elemental ratios during an ablation shown in Figure 8.

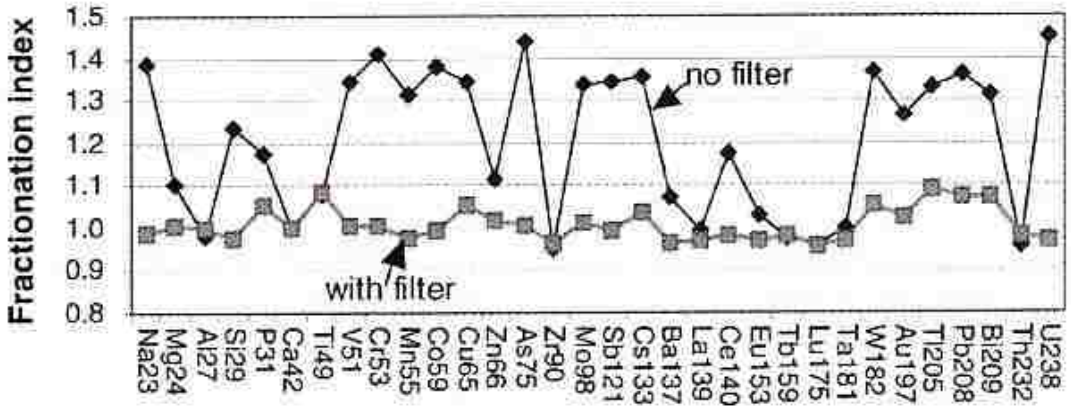

Figure 8: Fractionation indices calculated (26)

The fractionation index is derived by dividing the transient signal into two equal time segments and comparing the element intensity ratios normalized to an internal standard (calcium in Figure 8). Uranium is known to have a large time-dependent fractionation index of ~1.5 I (20-40s)/I (0-20s), where zirconium index is the lowest around 1 I (20-40s)/I (0-20s). Care must be taken when optimizing parameters for a matrix with two distinctly different analytes. It is important to verify if the variations in the signal intensity of the element is due to inhomogeneity of the sample or time-dependent fractionation.

Time-dependent fractionation results in preferential volatilization between elements within a large particle. In this case the more refractory element remains within the particle and is filtered in the ion beam. It is critical that the particle size distribution is reduced as much as possible. Previous groups have achieved this by glass wool placed or filter in the transport tube and helium as

the carrier gas (26,27). Mank et. al. (28) report for glass medium if the depth to diameter ratio is greater than 6 there is significant fractionation. Helium as the carrier gas significantly reduces large deposits surrounding ablation craters and the depth of penetration is 20-30% greater (25). Limiting the particle size distribution will be addressed in detail in Chapter 4.

It is difficult to calibrate the LA-ICP-MS in solid samples. Inductively Coupled Plasma-Mass Spectrometry is highly matrix-dependent and requires matrix-matched standards. Three general strategies are used for calibrating solid samples (21). The first is external calibration to a solid reference standard in combination with internal standardization (3). Most publications use an internal standard as it compensates for signal variations of the analyte of interest (25). The internal standard chosen must behave as the analyte during ablation, for this reason care must be taken in choosing the most suitable internal standard for the analyte of interest. This calibration method requires a known amount of a representative element in the sample. There are two strategies used to add an internal standard to a sample of unknown origins (29). First is micro-pipetting a known quantity of an internal standard onto the sample surface. Second is grinding and mixing an internal standard into the matrix. The second approach is undesirable for used nuclear fuel as it would increase sample handling.

The second strategy is calibration using solutions (29). One solution calibration approach is coupling an ultrasonic nebulizer to the laser ablation chamber where the desolvated standard solution is mixed with the ablated

sample and then introduced to the ICP torch. The second approach is having a y-junction attached to the tube where the solution is transported separately then introduced to the ICP. Another more direct system is using external solution calibration. The solution calibration is generally unsuccessful, due to the difference in solid and liquid mater laser beam absorption. Solids tend to have higher laser beam absorption than liquids. This can be explained by the effects of having a wet versus dry plasma introduction into the ICP source. A dry plasma improves atomization and reduces some matrix effects (29).

The third strategy is external calibration using solid reference standards which will be used in this research as it will take into account fractionation and ablation efficiencies. These matrix-matched standards are laboratory prepared and characterized to ensure homogeneity. This strategy ensures that the standards would behave in the same way as the samples of interest during the ablation process.

Spectroscopic interferences can occur in mass spectra within four categories: isobaric ions, refractory oxide ions, polyatomic ions, and doubly charged ions (24). Isobaric interferences for a quadrupole include isotopes that differ in mass by less than 1 mass unit. Polyatomic species form from interaction between species in the plasma, matrix and environment. These interferences are usually found below m/z of 82 and include $^{14}N_2^+$, $^{40}ArO^+$, and $^{40}Ar_2^+$. Oxides, hydroxides and hydrides are also known to form from the matrix components, analyte, or plasma gases. These interferences can be reduced by optimizing the

injector flow rate or nebulizer flow rate, radio frequency power, polished sample cone surface, and others. Matrix effects are also known to affect the analyte signal. If the concentration of one analyte is significantly larger than another a reduction or enhancement of a signal can be observed. Most of the isotopes of interest for safeguards and nuclear forensics in used nuclear fuel have m/z values above 82. For these isotopes, the spectroscopic interferences affecting quantitative analysis are the formation of oxides, hydroxides and hydrides as well as the concentration differences if analyzing multiple analytes at a time.

3.3 LA-ICP-MS with Nuclear Material

3.3.1 LA-ICP-MS in the Nuclear Fuel Cycle

Scientists have applied laser ablation sampling to a variety of materials relevant to the nuclear fuel cycle, such as alloys, ceramics, glass and minerals (30). The uranium content in the minerals for prospective mining sites can be quantified using LA-ICP-MS and has been studied extensively for the purpose of uranium-lead dating (22, 31, 32, 33). Using solution calibration procedures, Becker et. al. were successful in determining uranium and thorium concentration in basalt, andesite and zeolite geological samples (34). Laser ablation-ICP-MS was able to determine sub μg g^{-1} impurities in uranium fuel alloys prior to irradiation (35).

Used nuclear fuel can be dissolved for recycling, fabricated into its final waste form, or directly disposed. While theoretical modeling is able to evaluate fission product concentrations with acceptable uncertainty, used fuel aged over 20 years is expected to require further analysis (6). This is prominently valid for the United States as many used fuel assemblies have been stored at the plants for over 30 years. In France and Germany the content of about 60 radionuclides must be specified and limits are set for each nuclide per waste package with detection limits in the ng g^{-1} concentration range (4). Gastel et. al. tested the detection limits of ^{99}Tc, ^{129}I, ^{232}Th, ^{233}U, ^{235}U, ^{237}Np, and ^{238}U and found LA-ICP-MS meet the requirements for all nuclides except ^{129}I and ^{233}U in concrete matrices. This study was able to determine uranium and thorium concentrations with reproducibility of ± 20% RSD using calcium as an internal standard for the measurements. Becker et. al. were also successful in determining uranium and thorium isotope ratios in concrete and graphite matrices with precision of 1.2% RSD and accuracy of 0.43% for uranium (33).

Palmer et. al. (36) report LA-ICP-MS was superior to ICP-AES in quantifying the amount of palladium, rhodium, and ruthenium in used fuel slurry batches. This is due to the secondary lines of iron, thorium, uranium and other heavy elements coinciding with the major emission lines of the noble metals. The slurry batch samples were prepared in two ways: a dried powder and a lithium metaborate fusion which produces a nonhygroscopic glass matrix. It was found that the ruthenium selectively volatilized during the production of the glass while

the dried powder results were consistent with other waste analysis performed. Alexander et. al. performed LA-ICP-MS analysis on vitrified glass samples and tank waste stimulants from the Hanford Nuclear Waste site (37). After correcting the data for ablation efficiency using particle size distribution data, the percent deviation from known concentration of elements tested ranged from 5-20% for m/z range of 7-153.

3.3.1.1 LA-ICP-MS Sampling of Used Nuclear Fuel

Used fuel analysis and provide information related to operational performance and safety. Ha et. al. (38) performed a study on the compositional change of the used nuclear fuel along the diameter of the pellet to determine fuel performance at higher burn-up rates using LA-ICP-MS. Three samples were taken from two used fuel rods that had cooled for three years prior to analysis. Axial slices of 3 mm height were cut from the fuel rods along the cross-section of a pellet which including the fuel and cladding. The samples were then embedded in epoxy resin and polished. Ha et. al. found that the $^{236}U/^{235}U$ ratio remained constant across the pellet while the Pu isotopes to ^{235}U ratios significantly increase at the pellets rim. This can be explained by epi-thermal neutron capture of ^{238}U also known as the rim effect. These measurements precision ranged from 7-14% relative standard deviation. Ha et. al. also determined the distribution of the minor actinides ^{237}Np, ^{243}Am, and ^{244}Cm across the pellets and resulted in the

same build-up at the pellet periphery as the plutonium isotopes with precision ranging from 3.93-18.82% relative standard deviation. The lower precision in the minor actinide measurements can be explained by the low concentrations of these isotopes within the samples.

Ha et. al. performed a separate study determining $^{100}Mo/^{235}U$ ratios in used fuel using the same sample preparation (39). They found the same rim effect at high burn-up rates with molybdenum as the other isotopes in the previous study, with low precision ranging from 8.6 to 24% relative standard deviation. A section of each sample was dissolved and analyzed for average burn-up using thermal ionization mass spectrometer for comparison referred to as the Nd-148 method. Ha et. al. then used ORIGEN2 code to evaluate the relationship between the measured isotope ratios and burn-up rates shown in Table 4. The group found that burn-up profiles obtained by local isotopic ratios can be useful burn-up monitors.

Method	**Average specimen burn-up (GWd/tU)**		
$^{239}Pu/^{235}U$ distribution	32.4	42.6	56.8
$^{237}Np/^{235}U$ distribution	31.3	41	57.3
$^{243}Am/^{235}U$ distribution	27.3	40.1	58.9
$^{244}Cm/^{235}U$ distribution	27.4	41.1	60
Nd-148 method	33.3	41	57.6

Table 4: Average specimen burn-up calculated by the burn-up profile from the measured isotopic ratios and ORIGEN2 code (38)

Horvath et. al. measured the xenon concentration in fission gas bubbles of used nuclear fuel using LA-ICP-MS (40) for fuel performance evaluation. Fission gasses are known to accumulate as closed intragranular and intergranular bubbles within the fuel. When burn-up increases grain boundaries and pores are preferred sinks for the fission gas bubbles (10). If fission gasses are released into the free volume of the fuel rod they induce over pressurization and cladding failure (41). At high burn up rates the peripheral of the fuel pellets are known to accumulate fission gasses (10). Horvath et. al. studied two different calibration methods and found direct injection of a calibration gas of xenon while completely filtering the solid masses ablated results were in the same range as calculated models reported. The calibration was linear over 2.5 orders of magnitude with precision reported in the range of 5-10% relative standard deviation.

3.3.2 LA-ICP-MS for Forensic Purposes

The technical means by which nuclear materials, whether intercepted intact, or retrieved from post-explosion debris, are characterized and interpreted to determine the provenance, industrial history, and implications for nuclear device design is the definition of nuclear forensics (42). Hot particles or contamination in environmental matrices such as soil originating from releases from nuclear facilities or nuclear weapon tests characterization is of high importance to agencies such as the IAEA, the U.S. Department of Energy and the

Environmental Protection Agency. Varga analyzed depleted, natural, low and highly enriched uranium oxide particles (10-30 μm) for isotopic ratios using a laser ablation coupled with a sector field mass spectrometer and compared the solid sampling results with liquid sampling using the same spectrometer (43). The powder was transferred to a double sided tape and analyzed directly. Varga found the laser ablation method is able to determine isotope ratios of a 10 micron particle with precision of 0.9-5.1 % relative standard deviation. The method also leaves 80% of the particle intact.

Plutonium's isotopic composition varies according to its mode of production. Figure 9 illustrates how its isotopic ratios can be used to determine its source history. By measuring the $^{240}Pu/^{239}Pu$ and $^{238}Pu/^{240+239}Pu$ atom ratios, the reactor type and pre- or post-detonation nature of the Pu can be evaluated. Small changes in the global fallout ratios can be explained by different regions of the hemispheres (44). Cagno et. al. were able to distinguish between weapons grade, civilian grade and global fallout plutonium sources. Bottom sediments were collected from several reservoirs around the Mayak Production Association in the Urals, Russia. Two areas were tested, the first being the Asanov swamp and the areas down-stream of Mayak. This facility was the first weapons grade plutonium production site for the Soviet Union as well as later reprocessing civil nuclear waste. These samples were digested, radiochemical separations performed and electrodeposited on steel planchets prior to analysis on LA-ICP-MS. This study reports a limit of detection for ^{240}Pu to be 0.1 pg mm^{-2}. Although

the precision reported is significantly high 41.6-66.7% relative standard deviation, the accuracy of the measurements for $^{240}Pu/^{239}Pu$ was consistent with Accelerator Mass Spectrometry measurements.

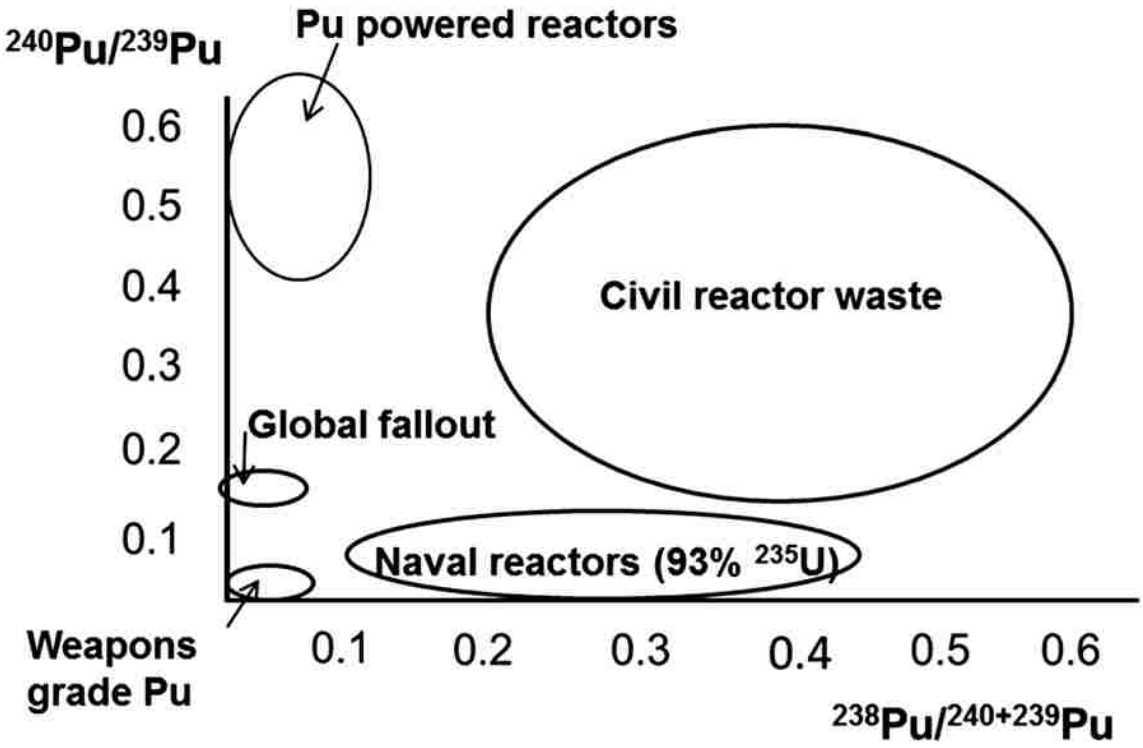

Figure 9: $^{240}Pu/^{239}Pu$ atom ratio vs. $^{238}Pu/^{240+239}Pu$ activity ratio of known sources (45)

Cizdziel et. al. examined plutonium isotopics to determine source history on soils collected in the western United States (44). The samples ablated were electrodeposited steel planchets that had undergone complete separations prior to analysis. This study found the LA-ICP-MS results were in agreement with the

alpha spectroscopy measurements previously studied, but do not report precision as replicates were not measured.

Chapter 4 – Minimizing Fractionation Effects of LA-ICP-MS

4.1 Abstract

Laser ablation-inductively coupled plasma mass spectrometry is desirable for measuring oxides due to the difficulties in dissolving the materials. An issue with laser ablation of oxides is the formation of aerosols with a range of particle sizes. This study uses centrifugal force and gravity within the transport tube to filter the larger particles and in turn minimize time-dependent fractionation. This is achieved by forming loops in the transport tube to permit settling of larger particles. Increasing the amount of loops in the transport tube considerably improved the accuracy of the measurements, from a linear correlation value of 0.9756 to 0.9997. The change in precision within the measurements using the loops as a filtration system was not as noticeable, with only a few percent gained with the average relative standard deviations. Standard materials were prepared to simulate used nuclear fuels rather than fresh fuels with pits and voids on the surface. Measurements were taken without polishing the surface of the materials.

4.2 Introduction

As in any analytical technique there are undesirable effects that must be understood and overcome in order to improve accuracy and precision of the measurement. With LA-ICP-MS such effects occur in the ablation, transport and detection processes. Laser ablation-inductively coupled plasma mass spectrometry has several limitations that can inhibit the utilization of this technique for many sample matrices and materials. A major limitation is elemental fractionation which is the non-sample related variation of the analyte response during the ablation process (28). Preferential vaporization of elements from the sample and the possibility of the composition altering during transport can lead to deviations in analysis results from actual composition (21). Particles of various sizes are generated during the ablation process which decrease the transport efficiency of the analytes and alter their signals. If a particle greater than 1 μm enters the ICP its vaporization and excitation may be incomplete, resulting in a lower signal for the constituents still present as a particulate as the particle is removed from sampling (26). Time-dependent fractionation results in preferential volatilization between elements within a large particle, favoring those species with a higher volatility. In this case, the more refractory element remains within the particle and is filtered in the beam. For this reason it is crucial that the particle size distribution is reduced as much as possible. Previous studies have limited time-dependent fractionation by placing glass wool or filter in the

transport tube and helium as the carrier gas (26, 27) or use cyclone-type spray chambers and other sample introduction devices (46, 47).

The purpose of this study is to demonstrate the ability of LA-ICP-MS to quantitatively determine the concentration of trace elements in a ceramic material with a rough surface without the need to polish or have a complex sample introduction system. The materials prepared and measured in this study are consistent with used nuclear fuel morphology and are directly ablated without any sample preparation. By forming large loops in the center of the transport tube, particle size distribution is minimized resulting in a stable, reproducible measurement.

4.3 Experimental

The instrumentation and optimization of LA-ICP-MS parameters are described in section 2.2.2. Table 5 lists the LA-ICP-MS parameters used to determine trace cerium in a uranium oxide matrix. The m/z value for ^{140}Ce measured was 139.905. The pellets were ablated for 30 seconds 3 times in different areas with the total signal collection time of 90 seconds. The average power density used for detection of cerium is 85.955 Wcm^2.

Laser Ablation	
Spot size	100 μm
Time per scan	30 sec
Scan rate	5 $\mu msec^{-1}$
Gas blank	20 sec
Average Power Density	85.944 Wcm^2
Pulse Rep Rate	5 Hz
ICP-MS	
RF Power	1050 W
Lens Voltage (V)	5.5 V
Analog Stage Voltage (V)	-1700 V
Pulse Stage Voltage (V)	825 V
Sweeps	10
Readings	800
Dwell Time	8 ms
Nebulizer flow (Ar)	0.8 L/min

Table 5: LA-ICP-MS Parameters for $(U,Ce)O_2$ pellets

TYGON transport tubing used in this study with an inner diameter of 0.3175 cm and outer diameter of 0.635 cm. The length of the tube was held constant at 96.52 cm with the distance of the laser ablation port to the ICP-MS torch of 33 cm. The diameter of the loops formed in the transport tube was 8.25 cm. A simple glass ball-joint adapter was used to couple the laser ablation to the ICP-MS torch instead of the standard spray chamber. The configuration of the transport tube is pictured in Figure 13.

Uranium-cerium oxide pellets composing of 1, 2, 5, and 10 mole % cerium were prepared with the final chemical form of $(U,Ce)O_2$ consistent with used nuclear fuel. The pellets were prepared by as described in section 2.1. The densities were measured using digital calipers and balance. A powder XRD was

used to confirm chemical homogeneity as described in section 2.2.1. Surface morphology was measured using a Leica DM 2500P microscope.

4.4 Results

4.1 Pellet Characterization

High burn-up used uranium oxide fuel analysis has shown three stable phases (11).The material in this study is a simplified version of the main oxide matrix that includes the actinide, lanthanides, and zirconium. Cerium is major fission product and forms solid solutions in the main oxide matrix (48). Cerium is also used as a surrogate for plutonium in ceramic materials as it has similar chemical and thermodynamic behavior (11). Cerium and plutonium have similar phase relationships, oxygen potentials and diffusion behavior in uranium oxide matrices (49). For these reasons $(U,Ce)O_2$ materials have been extensively studied and characterized in the literature and in turn chosen as a material of interest in this study.

Fresh, sintered, commercial light water reactor nuclear fuel is normally around 95-97 % of theoretical density (50). After irradiation and in-growth of fission products the theoretical density decreases between 1 % and 6 %, depending on length of irradiation and achieved burn-up (51). Table 6 lists the measured and theoretical densities obtained for the $(U,Ce)O_2$ pellet series. The theoretical densities range from 70.6 to 93.6% within the series. The 1-5 mole

percent cerium theoretical densities fall within those desired for simulated used nuclear fuel (10). The 10 mole percent cerium shows obvious swelling and bubbling within the pellet, with vertical swelling and bubbling evident on the top surface. The width of the 10 mole percent cerium pellets is 5.05 mm while the average of the other pellets is 4.94 ± 0.03 mm. It is common in used nuclear fuel for the material to experience swelling and creep (53), which are the main reason for plastic deformation but not at the scale observed for the 10 mole percent cerium. Although percent theoretical densities of used nuclear fuel are not expected to be observed below 90, the 10 mole percent cerium theoretical density of 70.6 ± 1.2 gives this study a range of porous material to observe the effects of laser-solid sampling.

Pellet (mol % Ce)	**Measured ρ [g cm^{-3}]**	**Theoretical ρ [g cm^{-3}]**	**% Theoretical ρ**
1	10.232 ± 0.213	10.937	93.6 ± 1.9
2	10.001 ± 0.177	10.904	91.7 ± 1.6
5	10.083 ± 0.196	10.804	93.3 ± 1.8
10	7.512 ± 0.126	10.638	70.6 ± 1.2

Table 6: Measured densities of $(U,Ce)O_2$ pellets

Porosity of ceramic material has adverse impacts on mechanical and thermophysical properties by lowering the theoretical density under 100 %.

Porosity is directly tied to thermal conductivity and microstructural pores do act as sinks for the accumulation of fission gas bubbles (10). Figure 10 displays the microstructure of the rough and untreated surface of the pellets analyzed in this study. The surface morphology is consistent with used nuclear fuel, which is not often thought as ideal for laser ablation analysis. The crater diameters averaged 59.4 ± 19.4 μm. Also shown in the 10 mol % cerium pellet are cracks and an uneven surface. The pits, cracks and voids on the surface of the material are the main physical feature of these ceramics that will impact and eventually complicate laser ablation analysis.

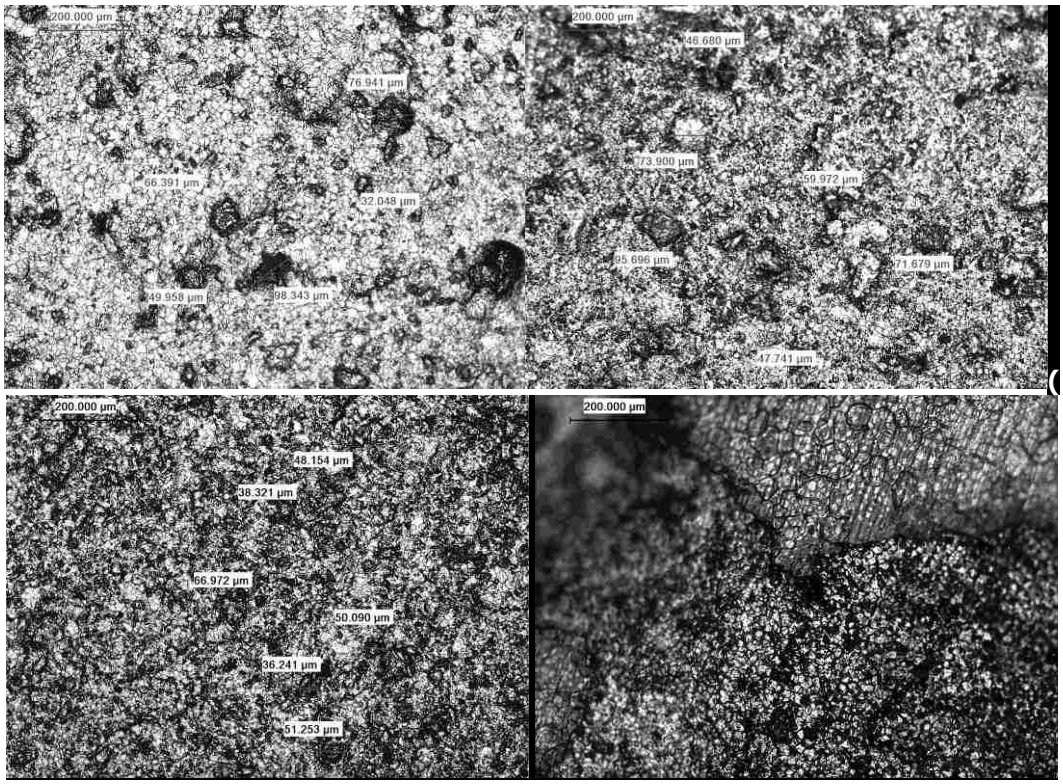

Figure 10: Microscope images of surface porosity of (U,Ce)O_2 pellets, top left 1 mol %, top right 2 mol %, bottom left 5 mol % and bottom right 10 mol % Ce. Measurements are the diameter of the pits observed on the surface.

The particle size distribution of the aerosol is increased significantly when the laser comes in contact with the edge of a crack or pit in the material (52). When the particle size distribution increases the probability of time-dependent fractionation also increases. Historically, laser ablation is successful with polished and uniform surfaces (53). However, for post irradiation analysis the surface is likely to be porous and rough, similar to the synthesized pellet. Furthermore, polishing the highly radioactive surface for analysis and create airborne particles and is therefore undesirable. For this reason the samples were not polished or treated prior to analysis by LA-ICP-MS.

A total of 30 mg of the pellets were ground using a mortar and pestle and analyze for homogeneity of phases using powder XRD (Table 7). The analysis was performed as described in section 2.2.1. The weighted profile factor, R_{wp}, is an indication of the agreement between the observed pattern and calculated diffraction pattern. A value less than 10 is indicative of an acceptable fit. All of the pellets consisted of a main face centered cubic (FCC) uranium dioxide pure phase in equilibrium with a $(U_{0.746}Ce_{0.244})O_2$ solid solution FCC phase with varying relative composition. Even though the pellets are not perfectly single phase, these results indicate that the pellets are homogeneous within the ablation area of 0.015 mm^2 since the grain sizes measured are in the micron range.

Pellet (mol % Ce)	UO_2 phase %	$(U,Ce)O_2$ phase %	R_{wp}
1	97.5	2.5	5.76
2	96.8	3.2	7.11
5	92.79	7.21	7.17
10	95.74	4.26	5.64

Table 7: Phase analysis of pellets in the UO2-CeO2 system by Rietveld structure refinement

Figure 11 and Figure 12 show the powder x-ray diffraction patterns for the 10 mol% cerium sample. The experimental measured pattern is in blue with a red overlay which is the fit. The grey line at the bottom is the difference between measured and fit. The middle blue pattern in Figure 11 is the known uranium dioxide FCC pattern and the middle black pattern in Figure 12 is the known FCC for (U0.746, Ce0.244)O_2 solid solution. The solid solution pattern appears as a shoulder on the main uranium dioxide pattern becoming more defined at higher 2 theta.

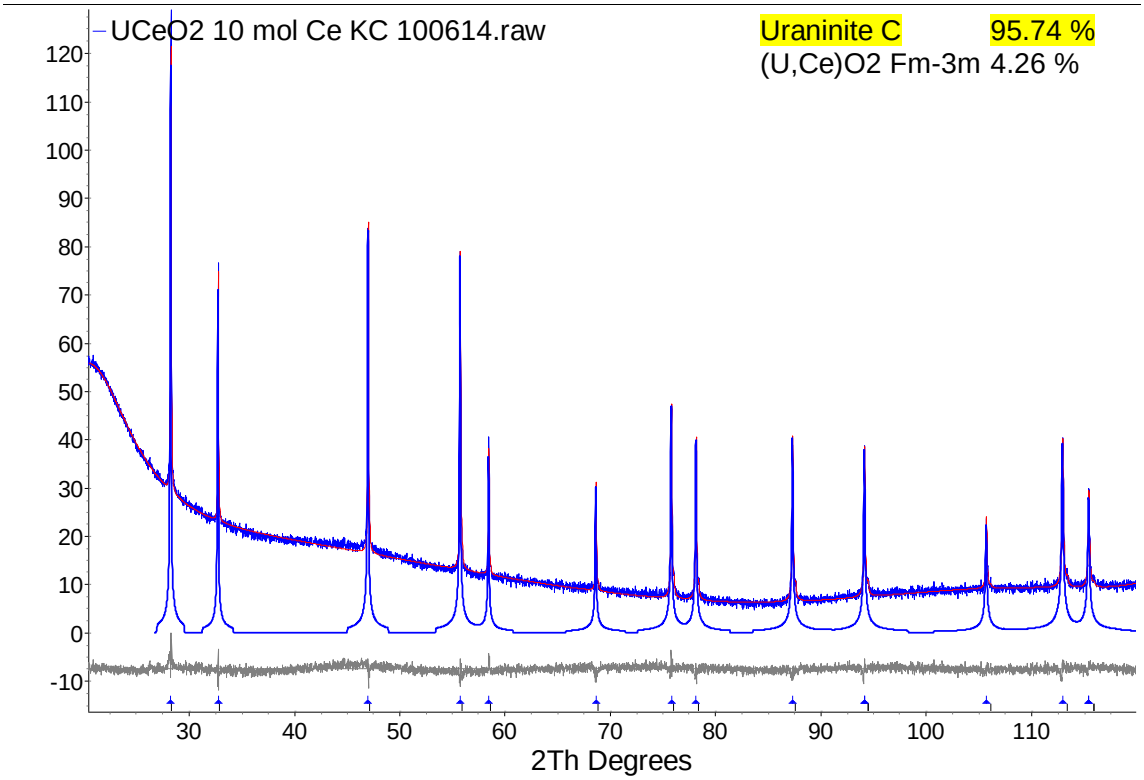

Figure 11: Powder XRD pattern of 10 mol% Ce in $(U,Ce)O_2$ sample with UO_2 phase highlighted in blue

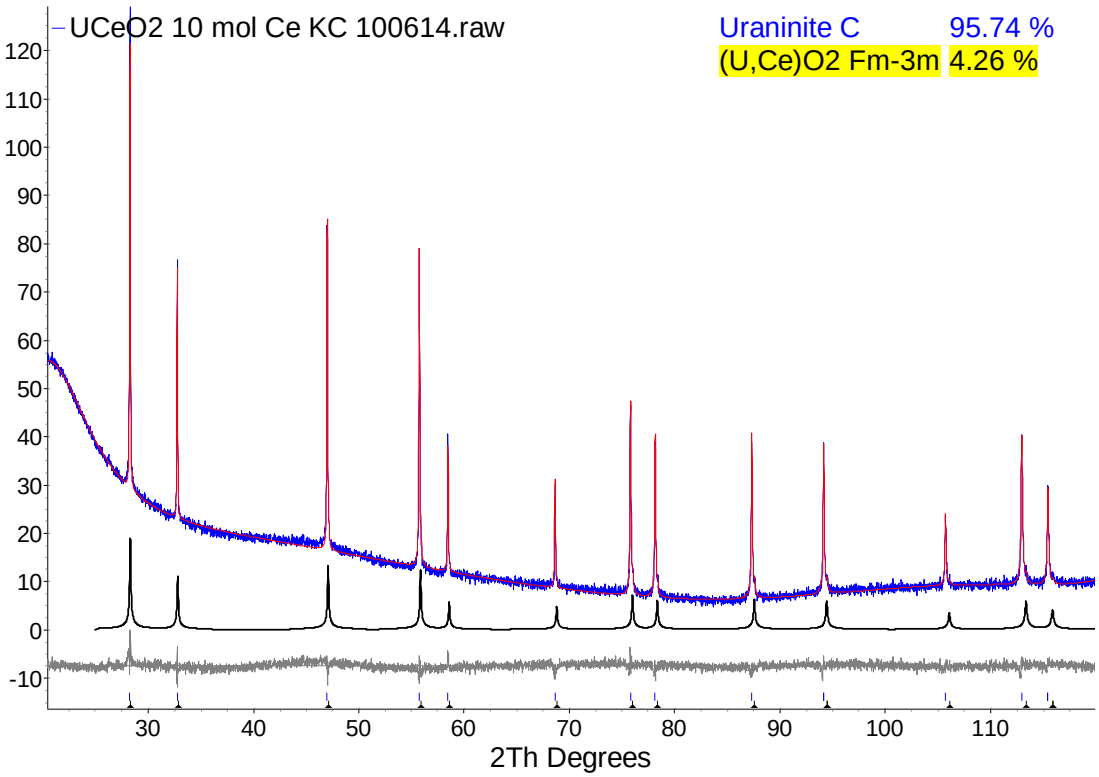

Figure 12: Powder XRD pattern of 10 mol% Ce in $(U,Ce)O_2$ sample with $(U,Ce)O_2$ phase highlighted in black

4.2 LA-ICP-MS Loop Study Results

To reduce large deviations in particle size of the aerosol during analysis, a comparative study was performed. Using the same length transport tube 0, 1, and 2 loops of 8.25 cm diameter were formed with the transport tube to mitigate the larger particles from reaching the ICP-MS shown in Figure 13. Previous work has shown that in order to acquire bulk analysis ratios for trace concentrations, the element with the highest concentration can come close saturating the detector in order to collect a stable signal for the trace elements. For this study

^{140}Ce signals were collected leaving ^{238}U to be filtered out of the ion beam in the ICP-MS. The large mass difference provided suitable separation to attain ^{238}U filtering. This technique was successful in achieving sufficient intensities of the trace elements thereby improving their limit of quantification.

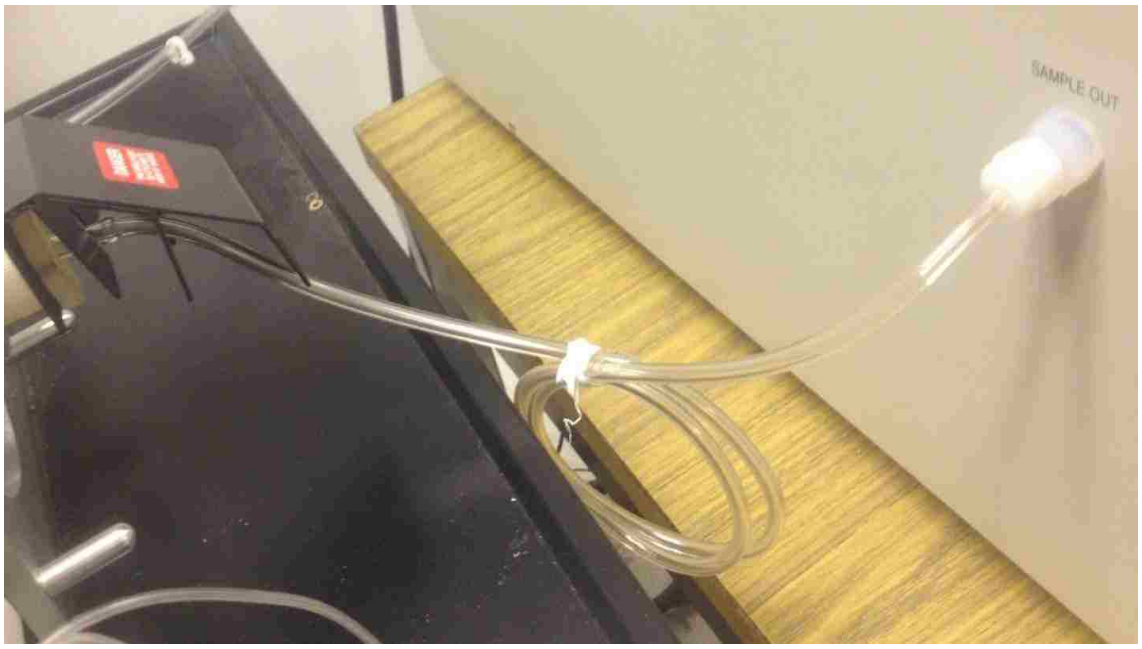

Figure 13: Photo of the transport tube configured with two loops

The traditional way to quantify concentration of an isotope using ICP-MS includes the analysis of a series of standards to establish a relationship between intensity of signal and concentration, which produces a calibration curve. The calibration curve should be linear within the range of interest in order to quantify the concentration of an unknown. Figure 14 shows the calibration curve with no

loops in the transport tube, providing a baseline for this study. The linear correlation is found to be 0.9756 with relative standard deviation ranging from 8.4 % to 33.6 % with an average of 17.3%.

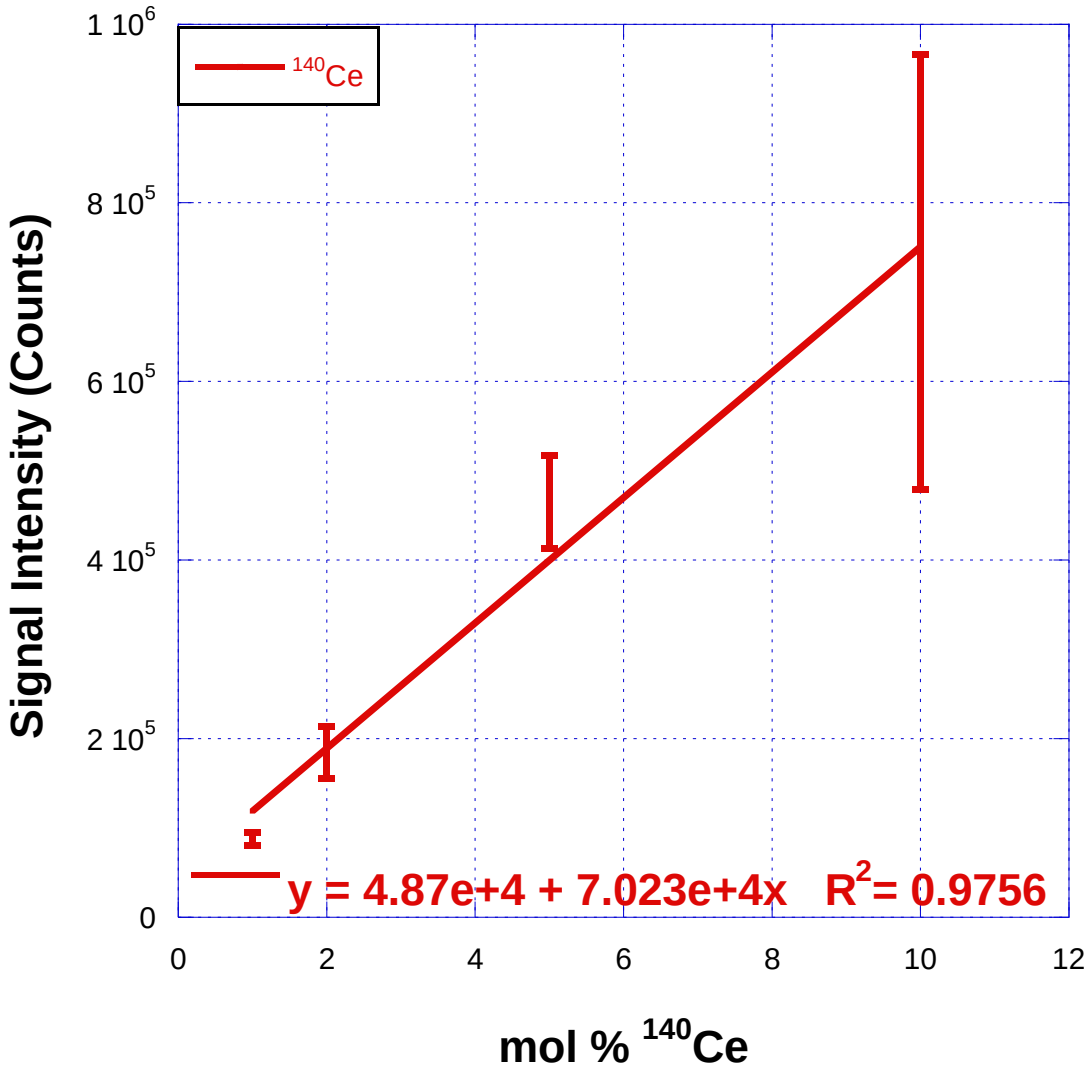

Figure 14: Calibration curve for the series using a straight transport tube

Figure 15 shows the calibration curve using one loop in the transport tube. The linear correlation is 0.9818 with relative standard deviation ranging from 2.9 % to 27.2 % with an average of 14.3 %. Comparing Figure 14 and Figure 15, there is an increase in the linear correlation factor and a decrease in the percent relative standard deviation. The centrifugal force the larger particles observe within the loop of the transport tube successfully hinders them from reaching the ICP-MS torch.

The two 8.25 cm loop results are presented in Figure 16. The linear correlation is 0.9997 with relative standard deviation ranging from 12.4 % to 20.8% with an average of 15.9%. When comparing 0, 1 and 2 loops, it is found that two loops have the highest linear correlation factor and the lowest percent standard deviation for the 10 mole percent cerium pellet. Having two loops in the transport tube increases the accuracy of the measurements significantly but the precision between the one and two loops has only slightly improved when compared to the zero loop measurements.

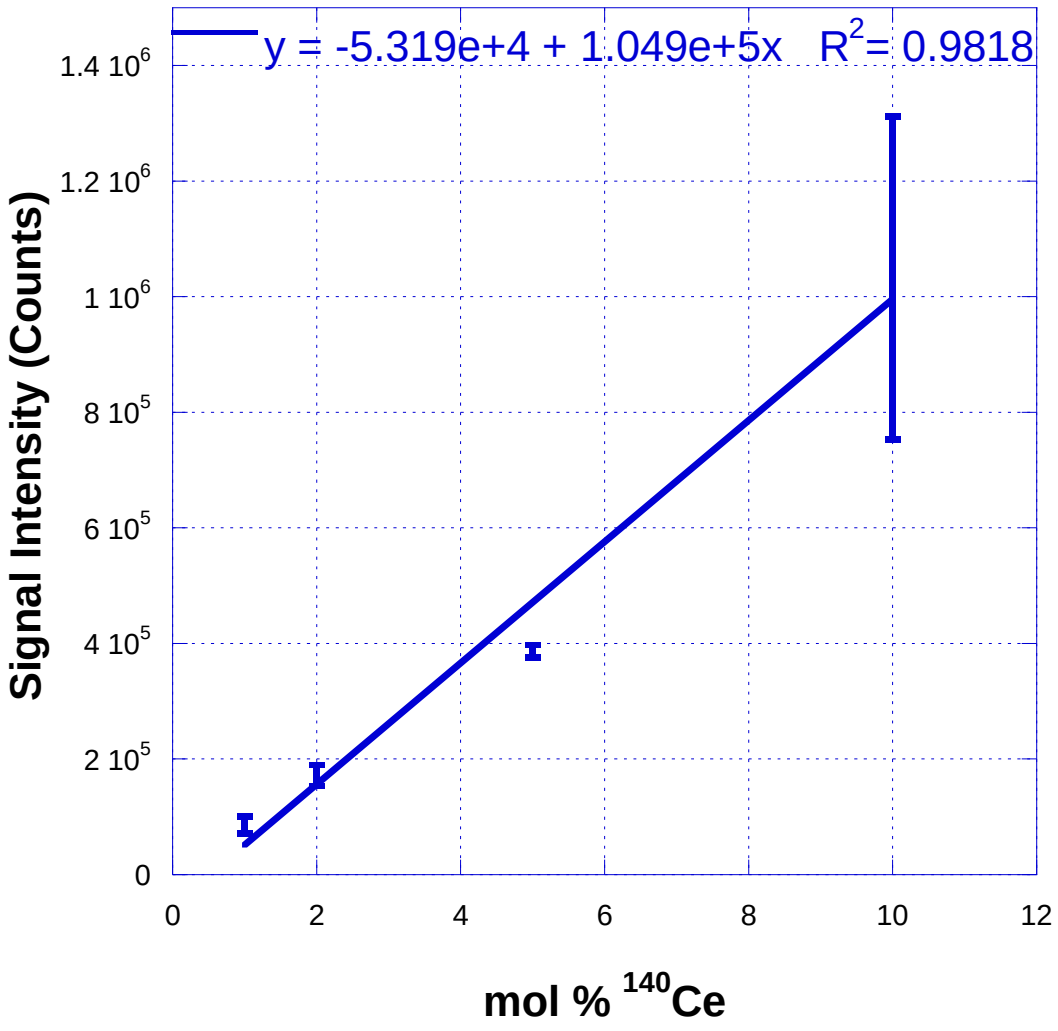

Figure 15: Calibration curve using 1 loop in the transport tube

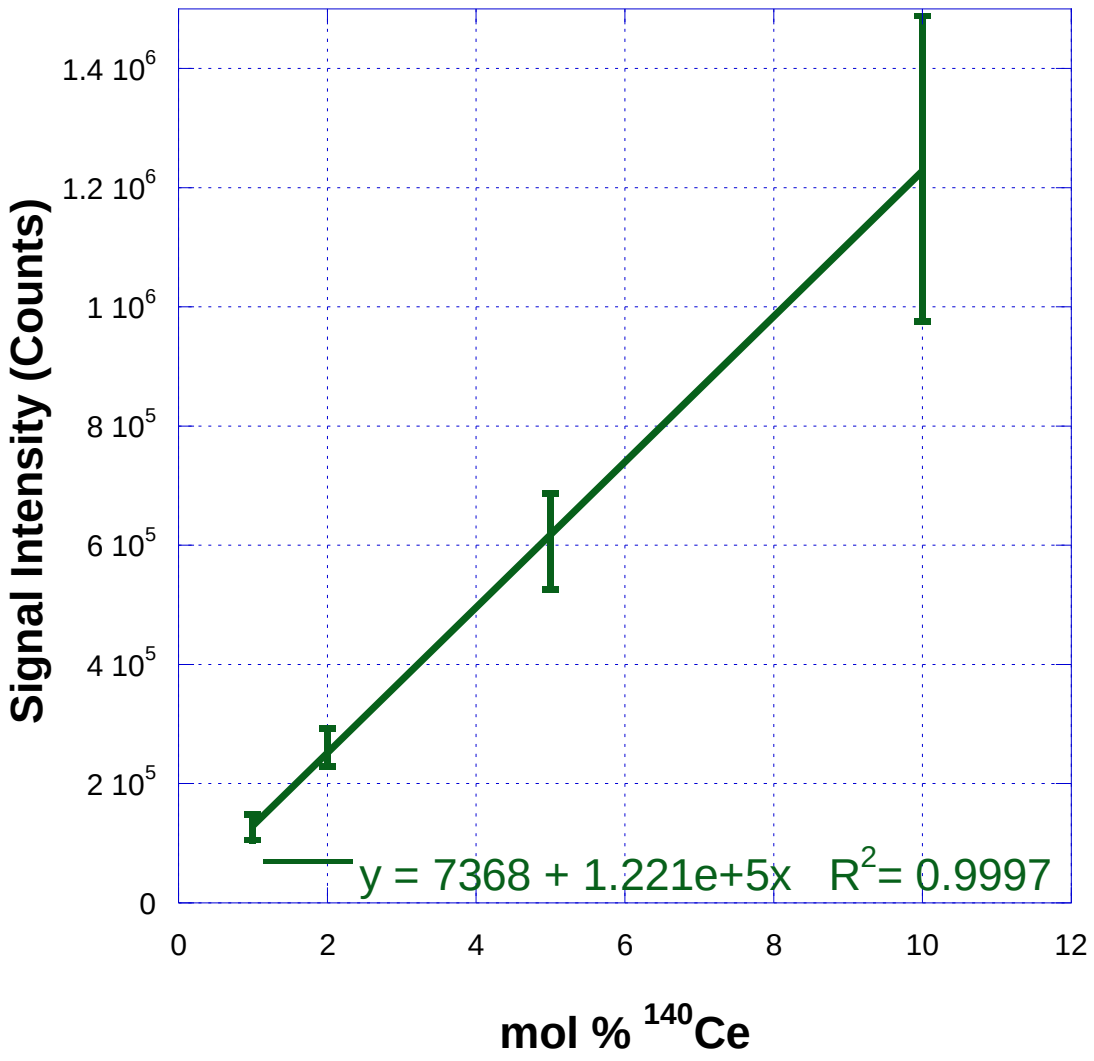

Figure 16: Calibration curve for 2 loops in the transport tube

Further studies were performed and found that having three loops in the transport tube suppressed the cerium signal and the linear correlation fell below 0.8 (Figure 17). The relative standard deviation ranged from 2.6 % to 21.1 % with an average of 12.9 %. The suppression of the cerium signal can be clearly seen when comparing the counts obtained for the 10 mole % cerium pellet. With

3 loops in the transport tube the 10 mole % cerium counts are 3.7E05, the counts with 2 loops are 1.2E06, almost an order of magnitude higher.

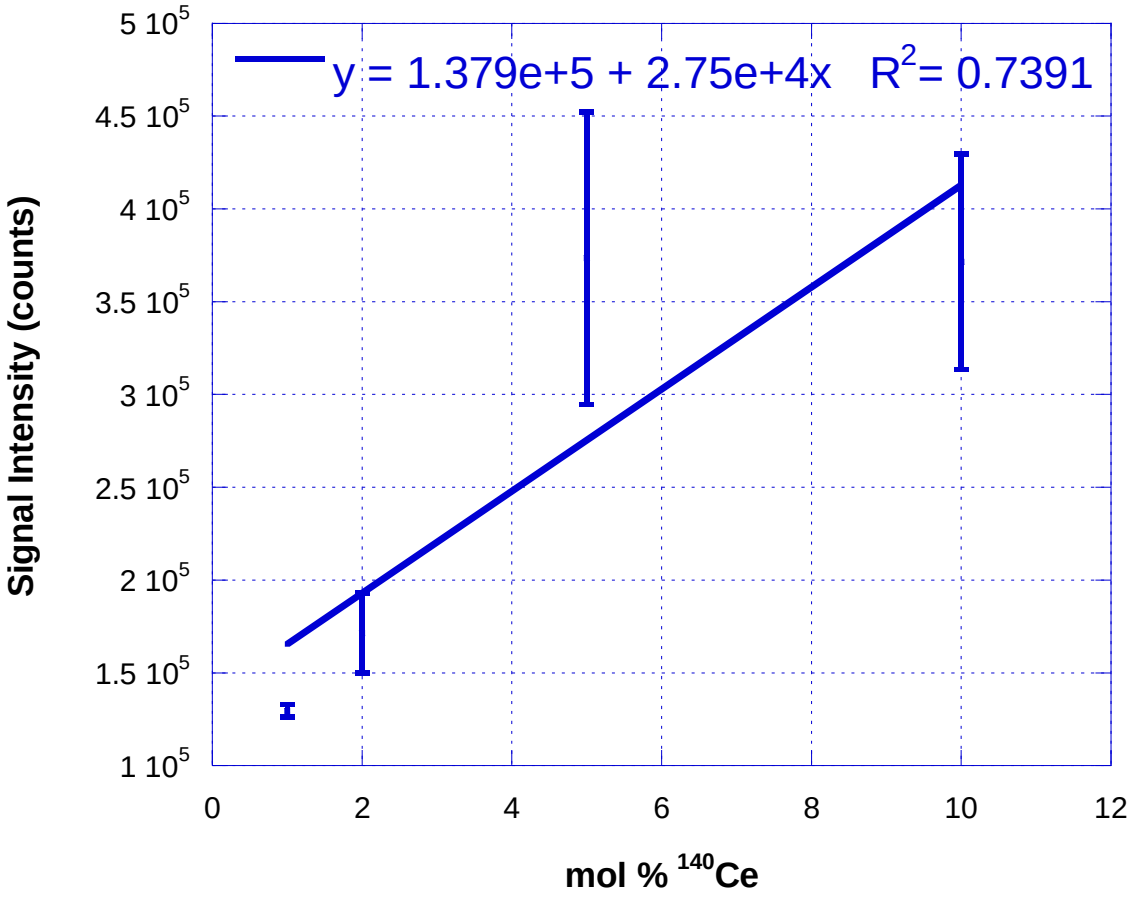

Figure 17: Calibration curve for 3 loops in the transport tube

4.5 Conclusion

Having loops in the transport tube successfully filtered the larger particles ablated from the untreated $(U,Ce)O_2$ surface. The smaller ablated particles that reach the plasma of the ICP-MS for detection limit element fractionation. By increasing the amount of loops in the transport tube the accuracy of the measurements considerably improved from a linear correlation value of 0.9756 to 0.9997. The change in precision within the measurements using the loops as a filtration system was not as noticeable with only a few percent gained with the average relative standard deviations within the series. The 10 mole percent cerium pellet's higher standard deviation can be attributed to its low theoretical density and higher porosity than the other pellets measured. These physical features of the materials may be a limiting factor to achieve relative standard deviations less than 10%.

Chapter 5 – Limiting Spectroscopic Interferences of ^{239}Pu and ^{237}Np in a $^{238}UO_2$ matrix

5.1 Abstract

Spectral overlap is a common event that occurs in ICP-MS detection. Whether it is peak tailing in neighboring channels of interest or hydride formation which interferes +1 amu quantification. Two saturation studies with a uranium source were completed to understand spectroscopic interferences using two LA-ICP-MS systems. The first study used an ELAN DRC II ICP-MS coupled with a CETAC LSX-500 laser ablation system. The laser power density was varied from 57.296 Wcm^{-2} to 157.563 Wcm^{-2} effectively saturating the m/z=238 channel while measuring the m/z=239 and m/z= 237 channels. It was found the m/z=239 channel remained at background regardless of the intensity of counts in the m/z=238 channel. The ratio of $^{239}Pu/^{238}U$ counts range from 6.88E-06 to 6.45E-05. The overlap of the uranium signal into the 237 channel is dependent on the laser power density applied to the material. The ratio of $^{237}Np/^{238}U$ counts ranges from 8.46E-05 to 1.47E-05. The second study used an iCAP-q-ICP-MS coupled with a NWR-213 laser ablation system. It was found using He as the carrier gas $^{239}Pu/^{238}U$ ranged from 8.53E-05 to 1.27E-04. The significantly higher $^{239}Pu/^{238}U$ ratio in this study is not peak tailing but a $^{238}UH^+$ formation confirmed by a mass scan survey with the hydrogen source coming from the He carrier gas. KED mode successfully lowered the $^{239}Pu/^{238}U$ ratio ranging from 2.77E-05 to

2.85E-05, also lowering the ^{238}U signal to 1.6E06. The mass scan survey also showed a second peak forming at the m/z 239.052 which suggests a hydride is still reaching the detector. Argon was used as the carrier gas where the $^{239}Pu/^{238}U$ ratio ranged from 6.46E-05 to 8.77E-05. These results are closer to the carry over observed in the first study with the $^{237}Np/^{238}U$ ratio.

Laser Ablation Inductively Couple Plasma Mass Spectrometry successfully measured plutonium in a uranium oxide matrix with a linear correlation factor of 0.9992 and the relative standard deviation for three runs varied from 3.7 to 9.6% for the calibration series. No signal overlap was observed from the bulk uranium in the 239 channel. The LA-ICP-MS parameters were successful in obtaining a linear correlation value of 0.995 and low percent relative standard deviations ranging from 3.9-8.9% for neptunium in a uranium oxide matrix. Although overlap in the 237 channel was observed, during analysis laser power density was kept below this feature to ensure no corrections needed. Each series was measured and analyzed within an hour which suggests a more rapid analytical technique than current methods in nuclear safeguards used to quantify plutonium and neptunium in a uranium matrix. The LA-ICP-MS also minimizes the handling of potentially hazardous material and reduces waste generation by directly ablating the solid.

5.2 Introduction

The limiting factor for using ICP-MS with liquid introductory system to analyze trace plutonium (m/z = 239) in a uranium matrix is the formation of uranium hydride (UH^+) which shows isobaric interference with ^{239}Pu. The UH^+ formation within the ICP-MS plasma has been extensively studied for liquid introductory systems (54, 55). Often corrections are needed for the hydride formation, separation of uranium from plutonium prior to analysis, or the use of a dynamic reaction cell to move one analyte to a higher m/z ratio (54). Directly ablating the material using LA-ICP-MS eliminates the main source of the hydrides within the system, nitric acid, offering a solution to the isobaric interference from the formation of hydrides.

Studies have been performed using LA-ICP-MS to determine radial distribution of plutonium isotopics in used nuclear fuel (56, 38). Leopold-Gunther et. al. found plutonium isotopics were in good agreement with the analysis by SIMS and EPMA but concluded that the lack of internal standard and reference material were the limiting factor for precise and accurate quantitative analysis. Ha et. al. measured the radial distribution of the isotopic ratios of ^{239}Pu, ^{237}Np, ^{243}Am in relation to ^{235}U, then compared the results to the ORIGEN2 code in order to determine burn-up of the fuel. These studies showed the ability to measure isotopic ratios of ^{239}Pu, but did not attempt to quantify the concentration of plutonium in the used fuel. To date none have successfully

quantified elemental concentrations within the samples, but quantified relative relationships of elements for spatial determination.

The purpose of this study is to demonstrate the ability of LA-ICP-MS to quantitatively determine plutonium and neptunium in a uranium oxide matrix with high precision and accuracy without an internal standard. The implications are that with a relatively inexpensive instrument and no sample preparation needed, LA-ICP-MS is a fast and reliable analytical tool for directly examining elemental and isotopic concentrations in a range of nuclear fuels without dissolution of material. Since standard reference materials are not readily available, the materials tested in this study were prepared and characterized for phase identification and density prior to LA-ICP-MS analysis. During the synthesis of the $(U,Pu)O_2$ pellets a kinetic study was performed to see how much ammonium hydroxide saturated in oxalate is needed to precipitate uranium and plutonium. A laser power study was performed on a 100% $^{238}UO_2$ pellet to show that the direct analysis of the solid in argon atmosphere eliminates hydride formation of ^{238}U. Following these results a stable reproducible signal of ^{239}Pu and ^{237}Np that is quantifiable was achieved for $(U,Pu)O_2$ and $(U,Np)O_2$ samples.

5.3 Experimental

The pellets were prepared as described in section 2.1. Prior to preparing the neptunium pellets, the neptunium dioxide source was converted to neptunium

nitrate using an autoclave synthesis route. Details and results of these syntheses are shown in section 5.4.1. Before precipitation of the $(U,Pu)O_2$ samples a kinetic study was performed to determine the amount of concentrated ammonium hydroxide saturated in oxalate in needed to precipitate uranium and plutonium nitrate from the de-ionized water. A 10 µL aliquot of the dissolved metal nitrates in water was prepared and counted using a Packard TriCarb 2700 TR liquid LSC. This sample was considered the baseline for the kinetic study. A 2 mL sample of concentrated ammonium hydroxide saturated with oxalate aliquot was then added to the bulk solution. The solution was then vortexed for 2 minutes and centrifuged for 5 minutes at 450 rpm. Another 10 µL aliquot of the supernatant was removed at 10 minutes of contact time and counted on the LSC. The solution and precipitate were placed on a shaker table overnight. After 24 hours of contact time, the material was then centrifuged for 5 minutes and another 10 µL aliquot was counted using LSC. Under these conditions uranium is precipitated as ammonium diuranate ($(NH_4)_2U_2O_7$). The vial was then centrifuged at 450 rpm for five minutes and then the supernatant was decanted from the precipitate. The precipitates were freeze-dried for 48 hours.

Table 8 shows the concentration of plutonium in used LWR fuel at different burn-ups. Using the g/kg reported, if it is assumed 0.5 g total material for each burn-up rate, the amount of plutonium and uranium used to produce 0.5g of each matrix is listed in Table 9.

Fuel Burnup (MWd/kg)	13	26	34	39
[Pu] (g/kg)	5.01	8	8.8	10.1

Table 8: Plutonium formation in 4% ^{235}U enriched LWR fuel as a function of burn-up (51).

Fuel Burn-up (MWd/kg)	**13**	**26**	**34**	**39**
[Pu] (g)	0.0025	0.004	0.0044	0.0051
[U] (g)	0.4975	0.496	0.4956	0.4949
wt% Pu	0.5	0.8	0.88	1.02

Table 9: Amount of material used to produce 0.5 g of each matrix

Table 10 shows the laser ablation and ICP-MS parameters used in the limit of detection analysis of ^{239}Pu in a uranium oxide matrix. Table 11 lists the LA-ICP-MS parameters used in the limit of detection analysis of ^{237}Np in a uranium oxide matrix. In both studies, the laser power density was varied from 57.296 Wcm^{-2} to 157.563 Wcm^{-2} in order to saturate the ^{238}U channel using a $^{238}UO_2$ pellet. The sampling area of the pellet was a 225 µm line that had a width of 100 µm. The ^{237}Np (m/z = 237.048), ^{239Pu} (m/z = 239.052) and ^{238}U (m/z = 238.05) signals were collected in the ICP-MS detector.

Laser Ablation	
Spot size	100 μm
Time per scan	45 sec
Scan rate	5 μm/sec
Gas blank	30 sec
Energy Level	varied
Pulse Rep Rate	5 Hz
ICP-MS	
RF Power	1100 W
Lens Voltage (V)	5.5V
Analog Stage Voltage (V)	-1700 V
Pulse Stage Voltage (V)	825 V
Sweeps	10
Readings	800
Dwell Time	8 ms
Nebulizer flow (Ar)	0.5 L/min

Table 10: LA-ICP-MS parameters for the ^{239}Pu signal in a $^{238}UO_2$ pellet using an Elan DRC II ICP-MS

Laser Ablation	
Spot size	100 μm
Time per scan	30 sec
Scan rate	5 μm/sec
Gas blank	30 sec
Energy Level	varied
Pulse Rep Rate	5 Hz
ICP-MS	
RF Power	1050 W
Lens Voltage (V)	5.5V
Analog Stage Voltage (V)	-1700
Pulse Stage Voltage (V)	825 V
Sweeps	10
Readings	800
Dwell Time	8 ms
Neb flow (Ar)	0.4 L/min

Table 11: LA-ICP-MS parameters for the ^{237}Np signal in a $^{238}UO_2$ pellet using an Elan DRC II ICP-MS

A second set of saturation studies were performed at Los Alamos National Laboratory using a NWR-213 New Wave Research laser ablation system coupled with a Thermo Scientific iCAP Q ICP-MS. These studies used the NIST 610 glass standard as the uranium source sample. Although the laser wavelength and sample are different than the first saturation studies since this is an observation of detector response, it does not conflict with the final results. The parameters of this study are listed in Table 12.

Laser Ablation	
Spot size	80 µm
Time per scan	45 sec
Scan rate	5 µmsec^{-1}
Gas blank	20 sec
Average Power Density	varied
Pulse Rep Rate	10 Hz
ICP-MS	
RF Power	1050 W
Lens Voltage (V)	6 V
Analog Stage Voltage (V)	-1700 V
Pulse Stage Voltage (V)	825 V
Sweeps	10
Readings	800
Dwell Time	10 ms
Nebulizer flow (Ar and He)	varied

Table 12: LA-ICP-MS parameters ^{237}Np and ^{239}Pu signals in a NIST 610 glass standard using an iCAP Q ICP-MS

Table 13 and Table 14 lists the optimal LA-ICP-MS parameters used to determine trace plutonium and neptunium in a uranium oxide matrix consecutively. Only the ^{237}Np and ^{239}Pu signals (m/z = 237.048 and 239.052

respectively) in each study are collected in the ICP-MS detector. The pellets were each ablated for 30 seconds and three times in different areas with a total signal collection time of 90 seconds. The signal was then integrated and normalized for time of integration. All of the data collected in this study used peak-hopping mode for the ICP-MS. The optimized average laser power density for the plutonium analysis was found to be 38.197 Wcm^{-2} and 31.821 Wcm^{-2} for the neptunium analysis.

Laser Ablation	
Spot size	150 µm
Time per scan	30 sec
Scan rate	5 $\mu msec^{-1}$
Gas blank	20 sec
Average Power Density	38.197 Wcm^{-2}
Pulse Rep Rate	5 Hz
ICP-MS	
RF Power	1100 W
Lens Voltage (V)	5.5V
Analog Stage Voltage (V)	-1700 V
Pulse Stage Voltage (V)	825 V
Sweeps	10
Readings	800
Dwell Time	10 ms
Nebulizer flow (Ar)	0.8 L/min

Table 13: LA-ICP-MS parameters for Pu analysis in $(U,Pu)O_2$ pellets

Laser Ablation	
Spot size	150 µm
Time per scan	30 sec
Scan rate	5 $\mu msec^{-1}$
Gas blank	20 sec
Avg Laser Power Density	31.821 Wcm^{-2}
Pulse Rep Rate	5 Hz
ICP-MS	
RF Power	1100 W
Lens Voltage (V)	5.5V
Analog Stage Voltage (V)	-1700
Pulse Stage Voltage (V)	825 V
Sweeps	10
Readings	800
Dwell Time	10 ms
Neb flow (Ar)	0.8 L/min

Table 14: LA-ICP-MS parameters for Np analysis in $(U,Np)O_2$ pellets

5.4 Results

5.4.1 Synthesis

In order to determine the amount of oxalate saturated concentrated ammonium hydroxide needed to sufficiently precipitate the plutonium from the water/nitrate solution a study was performed using the conditions listed for the 0.5 weight percent plutonium sample (Table 9). The results for the precipitation kinetic study are listed in Table 15.

Sample	Counts (cpm)	% Activity
Before	241648.2	100
10 minute contact	368.8	0.15
24 hours contact	143.2	0.06

Table 15: LSC results for precipitation kinetics

After 10 minutes of contact time with oxalate saturated concentrated ammonium hydroxide, 0.15% of total activity remained in the supernatant. Only 0.06% of the activity remained in solution after 24 hours. Using these results, 10 minute contact time was found to be sufficient for precipitating the remaining matrices. A 0.09% loss in overall activity is acceptable when taking into account of 24 hours are needed to recover a small amount of material.

A sample of ^{237}Np(VI) nitrate was prepared by first converting the neptunium mixed metal oxide to neptunium dioxide via flowing oxygen at 700 ºC for 12 hours. The solid changes to a red at 700 ºC indicating Np_2O_5 had formed. At 400 ºC a green solid is present Figure 18 (57). In an oxygen atmosphere at temperatures ranging from 700 K to 950 K, Np_2O_5 is unstable and decomposes to neptunium dioxide (58). The decomposition reaction is described in Equation 5.

$$Np_2O_5 \rightarrow 2NpO_2 + \frac{1}{2}O_2$$

Equation 5: Decomposition of Np_2O_5

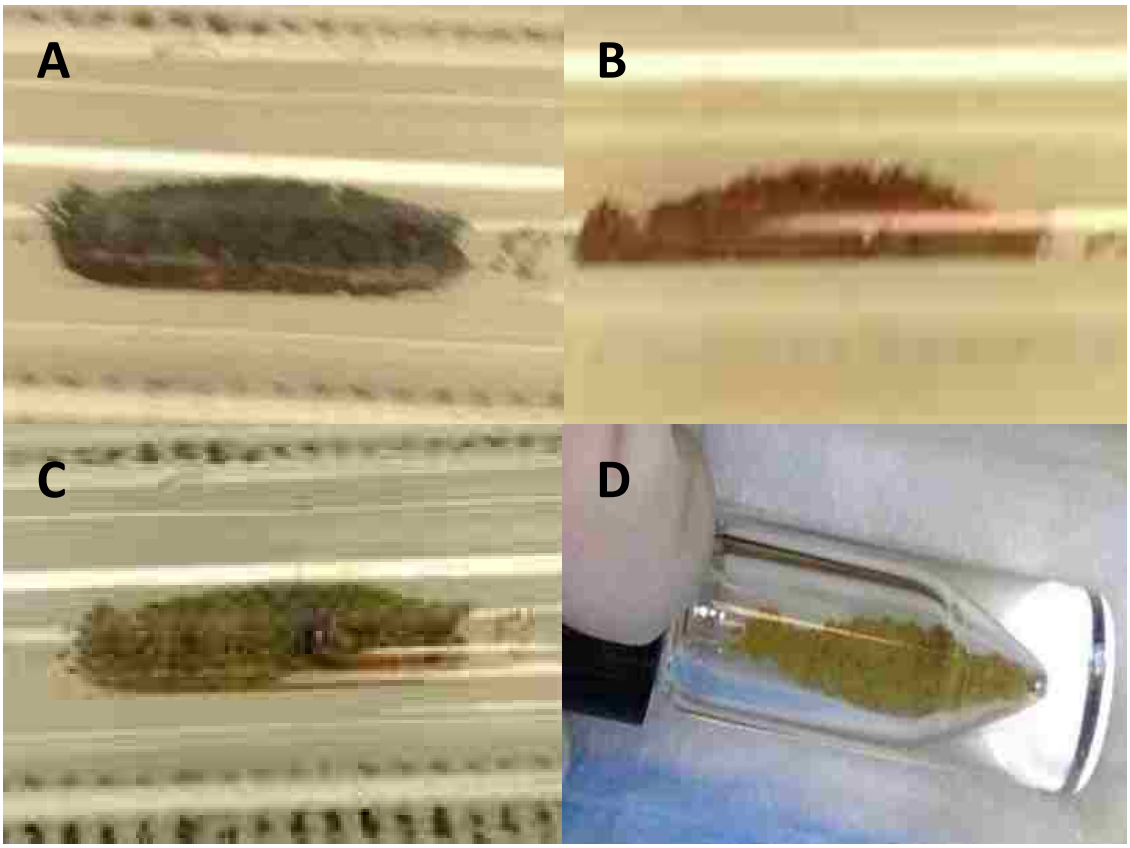

Figure 18: (A) A sample of NpOx (x = 0-2) load in quartz boat at room temperature. (B) Red solid at 700 ºC after 12hrs. (C) Green-solid after cooling to 400 ºC. (D) Green-brown solid NpO_2 at room temperature.

The powder XRD pattern of the green-brown product indicated full conversion to neptunium dioxide (Figure 19). The decomposition reaction was successful in preparing a crystalline face-centered cubic neptunium dioxide powder. This powder will then be the starting material for the conversion to Np(VI) nitrate.

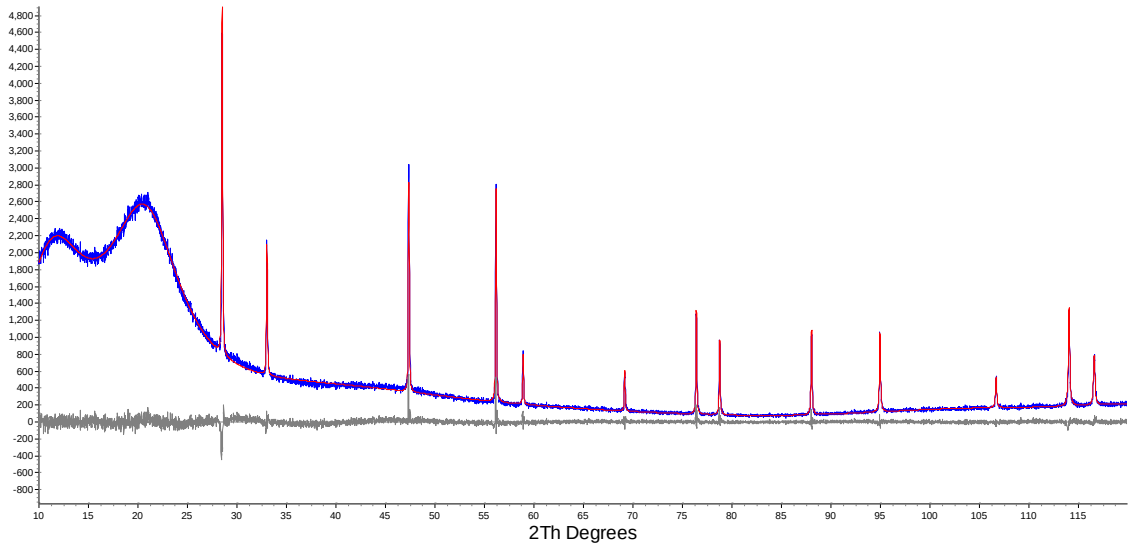

Figure 19: Powder XRD results of the NpO_2 powder

A 70 mg sample of the resulting neptunium dioxide solid was placed in 4 dram borosilicate glass vial of original dimensions 2.1 x 7.0 cm, inner diameter 1.8 cm, custom-cut to 3.5cm in height. A 5 mL aliquot of 8M HNO_3 was added to the vial and loaded in a 23 mL Teflon autoclave (Parr Instruments 4749, Figure 20) sealed and digested at 200 ºC for 72 hours.

A 100 µL of the dark green solution, seen in Figure 20, was diluted in 3 mL of 8M nitric acid and placed in a cuvette for UV-Vis spectroscopy analysis (Figure 21). The large band below 400 nm indicates a NpO_2^{2+}species identified as neptunium (VI) nitrate (59). Dukes and Shuler report sharp absorption bands at 715 nm for Np(IV) and at 617 nm for NpO_2^{+}. Neptunium (VI) nitrate also displays weak absorption bands 700 to 950 nm as seen in the spectrum measured for the dark green solution. The nitric acid concentration did not affect

the absorption spectrum for NpO_2^+ and NpO_2^{2+} but found slight shifts in the Np(IV) absorption bands.

Figure 20: Neptunium dioxide and 8M HNO_3 loaded in a 23 mL Teflon autoclave, Resulting dark green solution after 72 hours digestion at 200 °C.

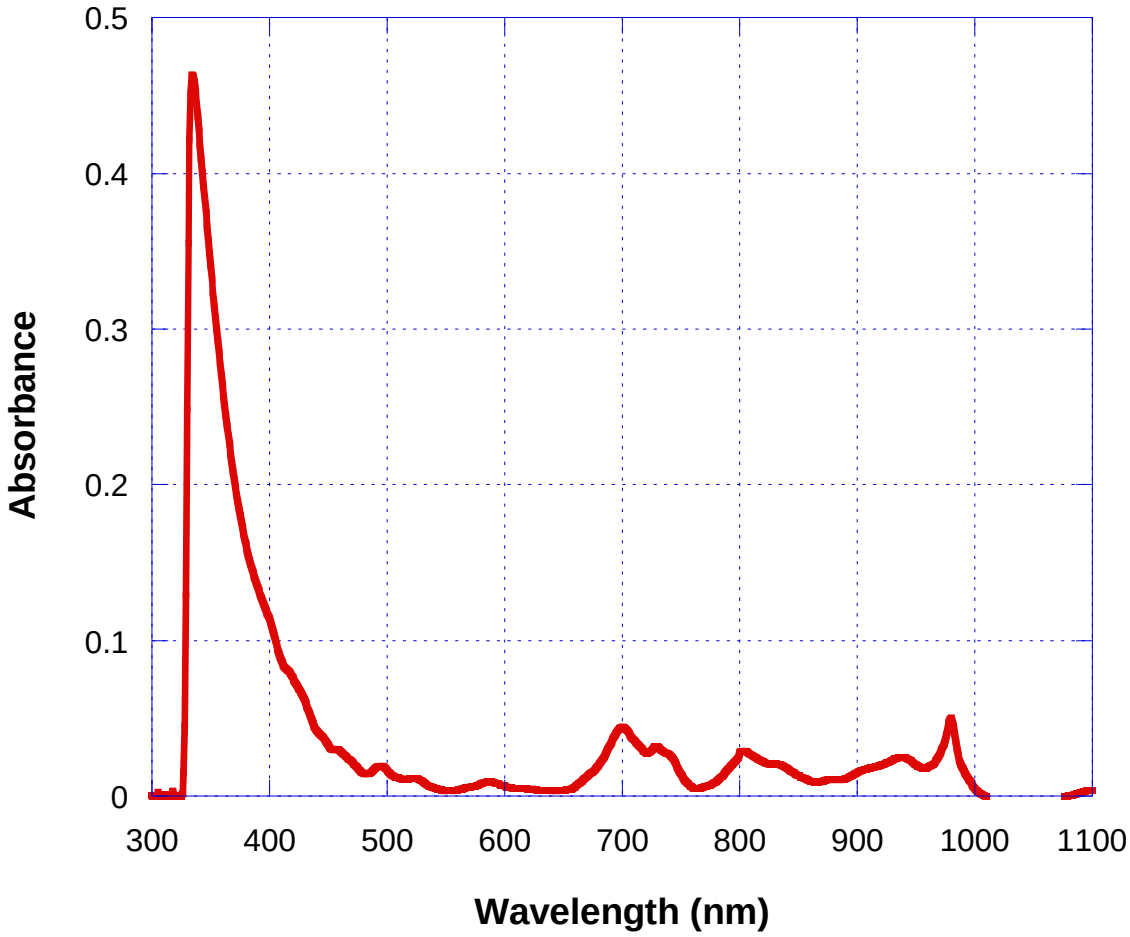

Figure 21: UV-Vis spectroscopy results of dark green solution from autoclave synthesis.

The Np(VI) nitrate solution concentration was then quantified by LSC shown in Table 16. Correcting for the in-growth of ^{233}Pa and its daughter ^{233}U, the final concentration of neptunium is 0.052 M ^{237}Np(VI) nitrate, where all of the neptunium was digested.

Original mg	Original V (mL)	Sample	cpm 10µL	M (mol/L)	^{237}Np (mg)
0	0	Blank	50.8		
70	5	Autoclave	480282	0.129	153.48

Table 16: LSC results from Np(VI) nitrate synthesis

5.4.2 Density Measurements

The $(U,Pu)O_2$ pellet densities range from 8.818 ± 0.153 to 10.254 ± 0.255 gcm^{-3} (Table 17). The lower densities of the 1.02 wt% plutonium pellet y and the 0.88 wt% plutonium pellet x can be explained by a lateral crack observed for these pellets. The remaining pellets have theoretical densities exceeding 85%, with the highest at 93.5%.

Pellet (Pu wt%)	Theoretical ρ [g cm^{-3}]	Measured ρ [g cm^{-3}]	%Theoretical ρ
0.5 PX	10.973	10.254 ± 0.255	93.5 ± 2.5
0.5 PY	10.973	10.130 ± 0.241	92.3 ± 2.4
0.8 PX	10.974	9.588 ± 0.253	87.4 ± 2.6
0.8 PY	10.974	9.534 ± 0.228	86.9 ± 2.4
0.88 PX	10.975	9.049 ± 0.210	82.5 ± 2.3
0.88 PY	10.975	9.606 ± 0.196	87.5 ± 2.0
1.02 PX	10.975	9.861 ± 0.269	89.9 ± 2.7
1.02 PY	10.975	8.818 ± 0.153	80.4 ± 1.7

Table 17: Percent theoretical densities measured for $(U,Pu)O_2$ pellets

Fresh, sintered, commercial light water reactor nuclear fuel is normally around 95-97 % of theoretical density (50). After irradiation and in-growth of fission products the theoretical density decreases between 1 % and 6 %, depending on length of irradiation and achieved burn-up (51). While the pellets synthesized are not within the fresh nuclear fuel densities, they fall within the range of higher burn-up used nuclear fuel with the exception of the defected pellets.

The neptunium pellet densities are listed in Table 18. The percent theoretical densities range from 84.96 ± 2.73 to 91.44 ± 2.71. No physical defects were observed for these pellets and were pressed under the same conditions as the plutonium pellets. The pellets percent theoretical densities below 90 have larger diameters suggesting not as much shrinking and compacting in the sintering phase as the pellets' above 90. The average theoretical density is 88.33 ± 2.16%. The synthesis was successful in producing desirable densities with only one pellet below 85%.

mol % Np	Measured ρ [g cm^{-3}]	Theoretical ρ [g cm^{-3}]	% Theoretical ρ
0.25 PX	9.658 ± 0.230	10.970	88.04 ± 2.38
0.25 PY	9.450 ± 0.285	10.970	86.14 ± 3.02
0.5 PX	9.967 ± 0.260	10.971	90.85 ± 2.60
0.5 PY	9.320 ± 0.254	10.971	84.96 ± 2.73
0.75 PX	9.603 ± 0.238	10.971	87.53 ± 2.48
0.75 PY	9.589 ± 0.256	10.971	87.40 ± 2.67
1.0 PX	9.589 ± 0.229	10.971	87.40 ± 2.39
1.0 PY	9.716 ± 0.279	10.971	88.55 ± 2.87
1.25 PX	9.985 ± 0.275	10.972	91.01 ± 2.75
1.25 PY	10.033 ± 0.272	10.972	91.44 ± 2.71

Table 18: Percent theoretical densities measured for (U,Np)O_2 pellets

5.4.3 Powder XRD Results

To determine homogeneity and crystallinity powder XRD was performed using a Bruker D8 Advance. The pellets were mounted using clay for direct measurement as described in section 2.2.1. Figure 22 and Figure 23 display the powder XRD patterns for the 0.88 and 1.02 wt % plutonium in (U,Pu)O_2 pellets, respectively. It was found that all matrices were a single phase, face centered cubic, and had no impurities. Plutonium undergoes isomorphic substitution within the uranium dioxide matrices (60). The narrow peaks with large relative intensities in the XRD pattern indicate high crystallinity and uniform equiaxed

grains within the pellets (61).The sintering time and temperature profile use in the synthesis was successful in ensuring homogeneity within the pellets.

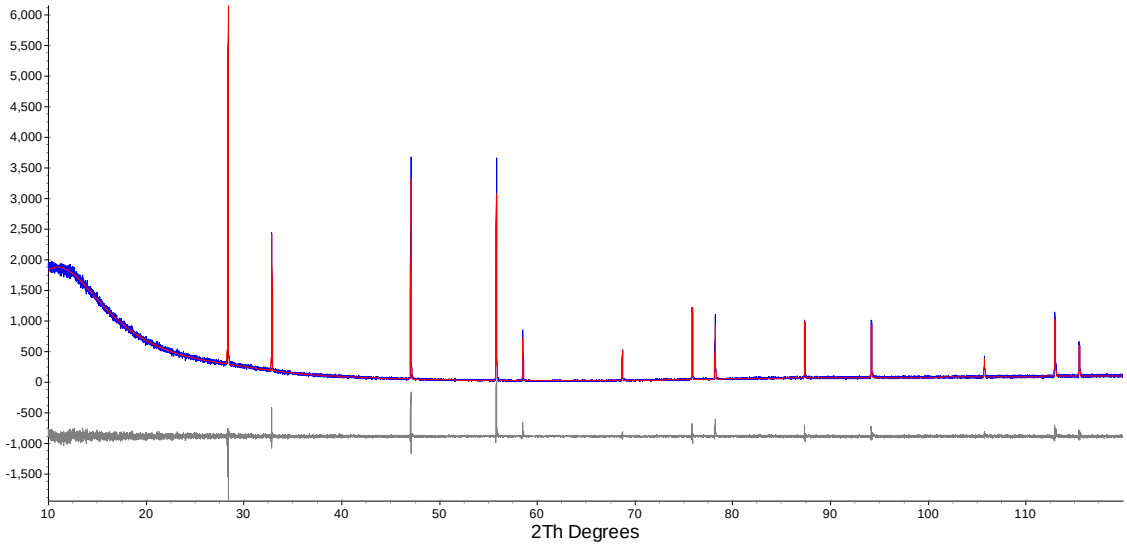

Figure 22 : Powder XRD pattern for 0.88 wt% Pu (U,Pu)O_2

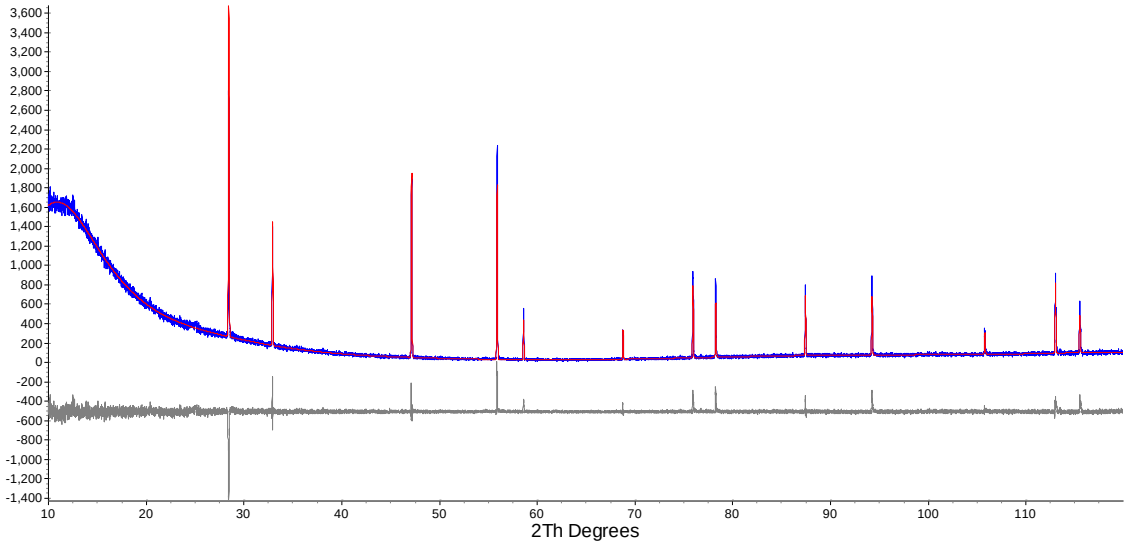

Figure 23: Powder XRD pattern for 1.02 wt % Pu (U,Pu)O_2

Examples of the $(U,Np)O_2$ powder XRD pattern are shown in Figure 24 and Figure 25 with the two phases highlighted. The main UO_2 is highlighted in blue in Figure 24 and the $(U,Np)O_2$ solid solution phase is highlighted in black in Figure 25. The solid solution phase appears as a shoulder on the main UO_2 phase with more definition at higher two theta. This shift signifies a lower d-spacing within the crystal lattice of the solid solution phase compared to the UO_2 phase.

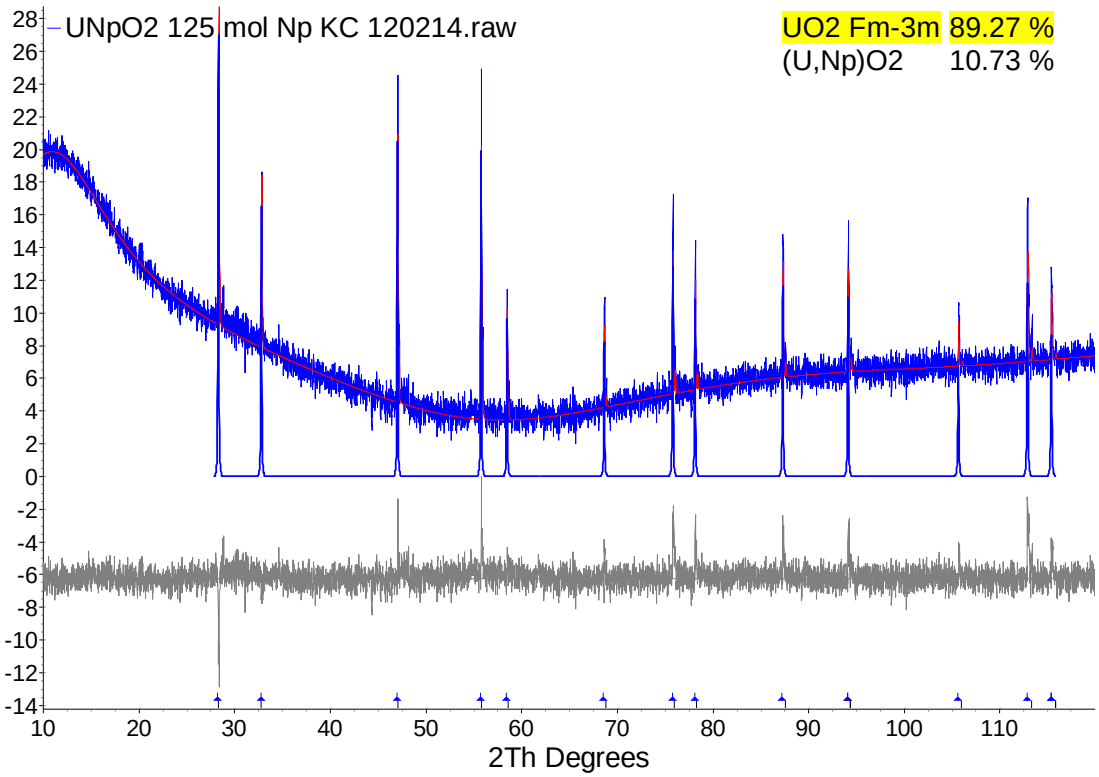

Figure 24: Powder XRD pattern for $(U,Np)O_2$ 1.25 mol% pellet with UO_2 phase highlighted

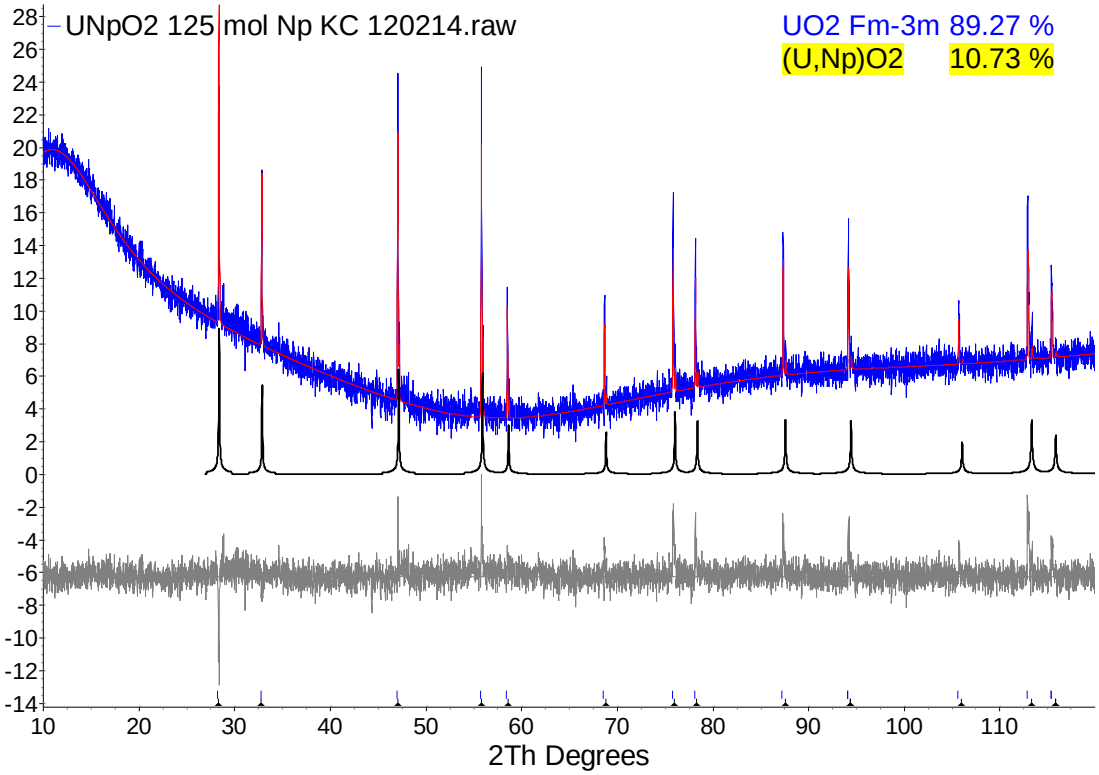

Figure 25: Powder XRD pattern for $(U,Np)O_2$ 1.25 mol% pellet with $(U,Np)O_2$ phase highlighted

The relative phase concentrations for the $(U,Np)O_2$ series are provided below (Table 19). All pellets contained two fcc phases, a pure UO_2 phase and a $(U,Np)O_2$ solid solution. Normally the desired R_{wp} is less than 10, but for most of these patterns small differences in intensities were observed between the experimental and measured peaks due to slight peak deformities of the measured peaks from a Gaussian shape. A single solid solution may be obtained by increasing the sintering time at 1700 °C and annealing at a lower temperature.

Pellet (mol % Np)	UO_2 phase %	$(U,Np)O_2$ phase %	R_{wp}
0.25	92.97	7.03	10.24
0.5	94.07	5.93	10.46
0.75	87.49	12.51	12.83
1.0	92.67	7.33	8.64
1.25	89.27	10.73	15.27

Table 19: Phase analysis of pellets in the UO_2-NpO_2 system by Rietveld structure refinement

5.4.4 Saturation Study

Signal overlap due to peak tailing from saturating the detector is commonly observed in ICP-MS measurements. In order to quantify any signal overlap of ^{238}U (M/z=238.05) into ^{239}Pu (m/z=239.052) channel a laser power study was performed with a 100% $^{238}UO_2$ pellet (Figure 26) using instrument parameters listed in Table 10. The laser power density was varied from 57.296 Wcm^{-2} to 157.563 Wcm^{-2}, effectively saturating the m/z=238 channel at 130 Wcm^{-2} while measuring the m/z=239 channel. It was found the m/z=239 channel remained at background regardless of the intensity of counts in the m/z=238 channel.

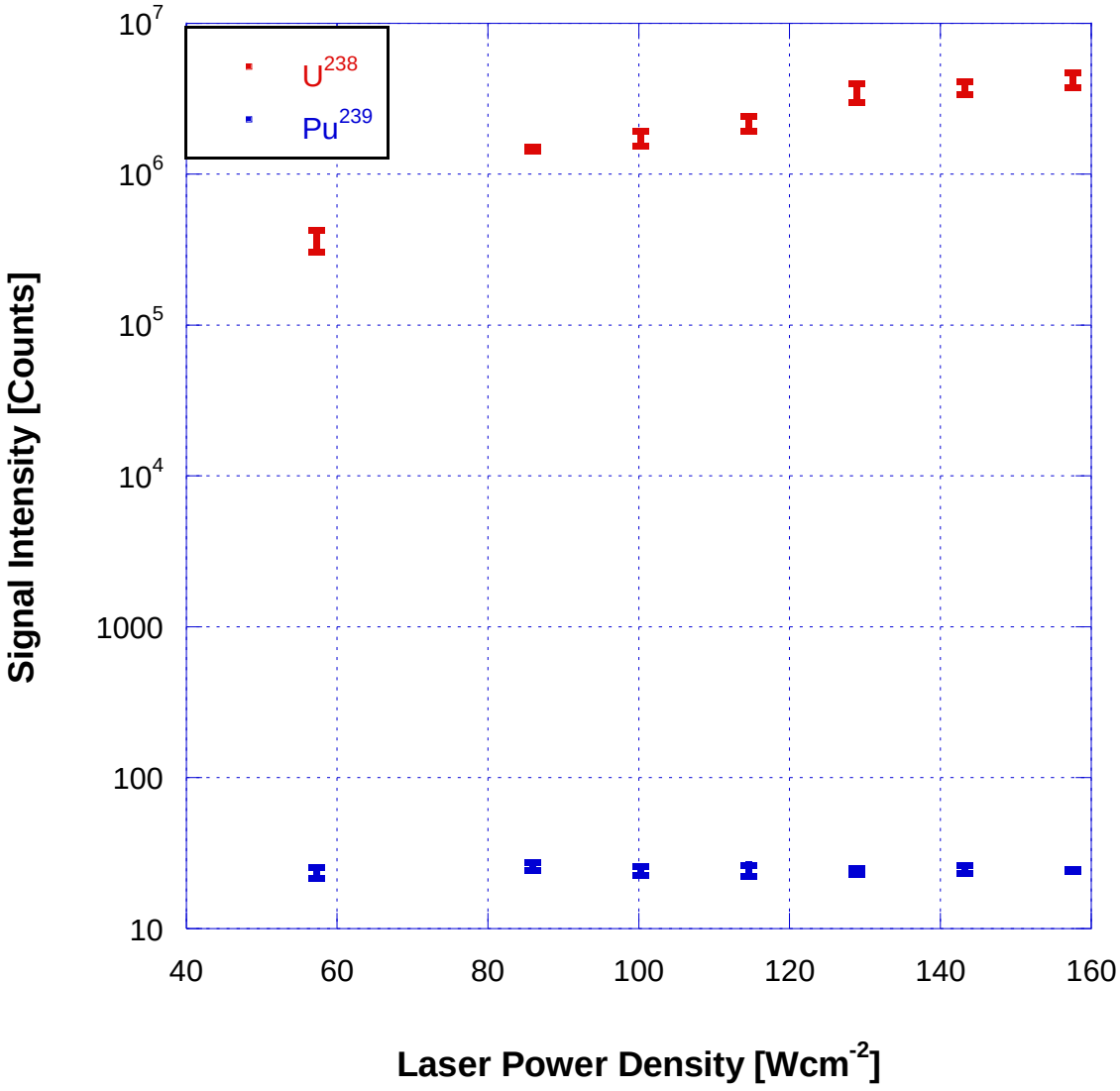

Figure 26: Laser Power Study of ^{239}Pu using 100% $^{238}UO_2$ Pellet

In order to clearly see the ^{239}Pu signal trends, the ^{239}Pu signal is graphed separate from the ^{238}U signal in Figure 27. Small fluctuations in the average signal intensity are apparent ranging from 23.456 counts to 26.04 counts with relative standard deviation 1.28 to 8.97 % indicating low background in the 239

channel with no observable overlap of the uranium signal. The ratio of $^{239}Pu/^{238}U$ counts range from 6.88E-06 to 6.45E-05. This ratio is significantly less than previous reported values of 9.1E-04 (4).

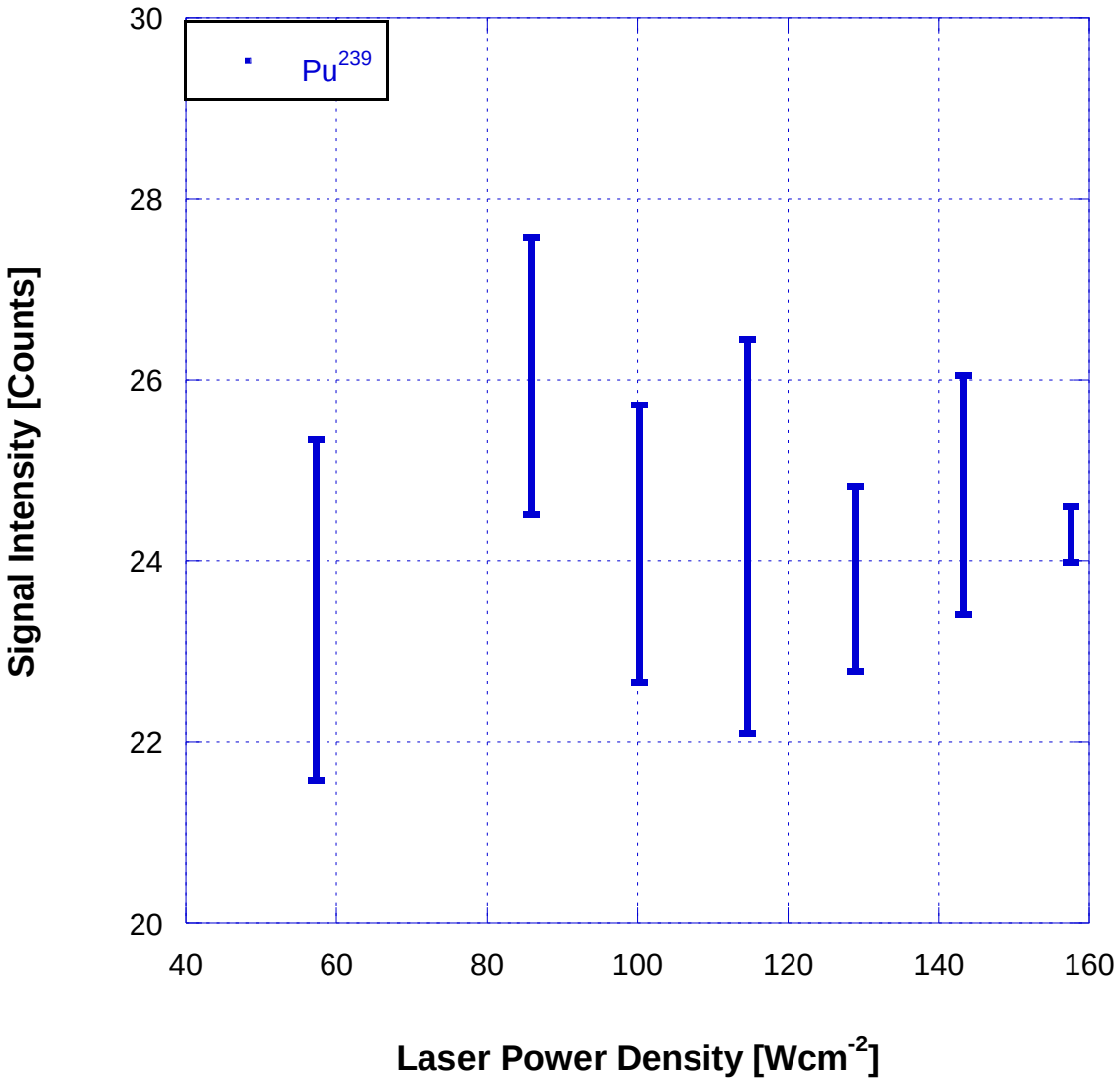

Figure 27: ^{239}Pu signal in Laser Power Study using 100% $^{238}UO_2$ Pellet

The same saturation study was performed with a 100% $^{238}UO_2$ pellet in order to quantify any signal overlap of ^{238}U (M/z=238.05) into the ^{237}Np (m/z=237.048) channel (Figure 28) with instrument parameters listed in Table 11. The laser power density was varied from 57.296 Wcm^{-2} to 157.563 Wcm^{-2} effectively saturating the m/z=238 channel while measuring the m/z=237 channel. It was found the m/z=237 channel increases significantly as the laser power density increases by a factor of 2.

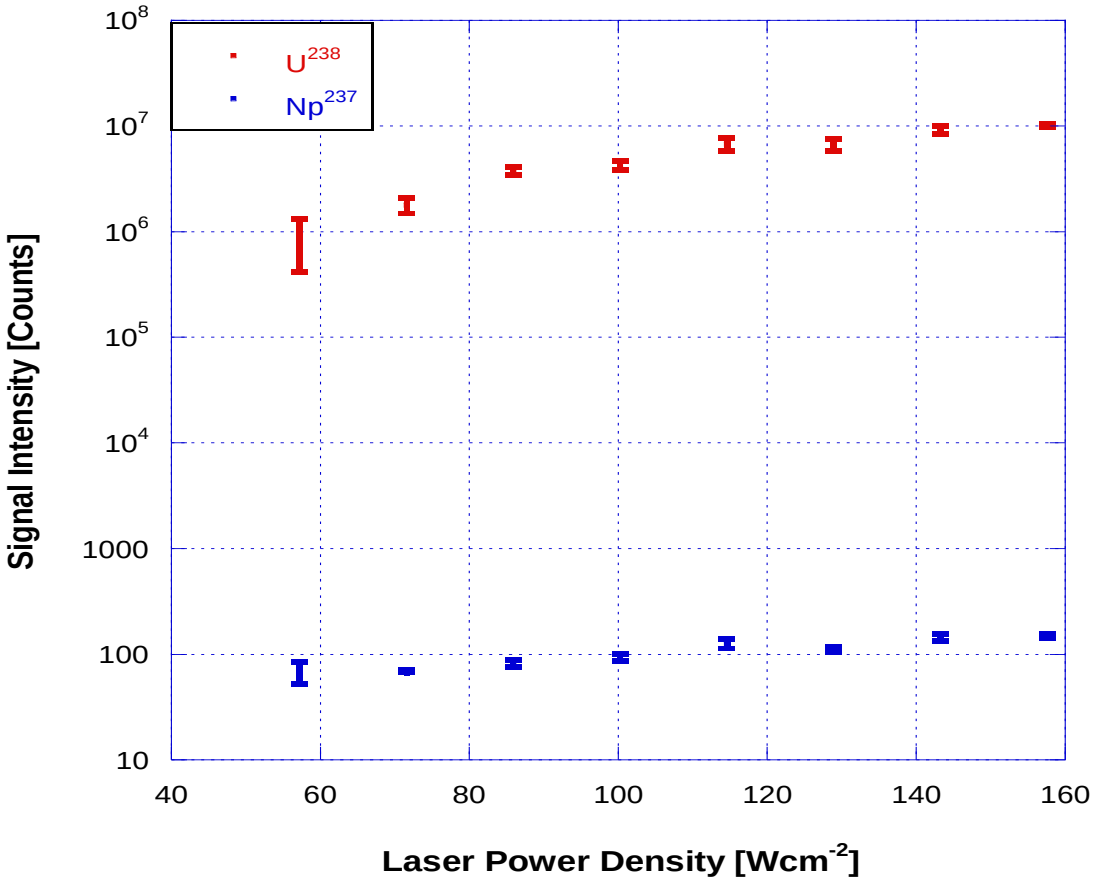

Figure 28: Laser Power Study of ^{237}Np using 100% $^{238}UO_2$ Pellet

The ^{237}Np signal from Figure 28 is graphed separately in Figure 29 to show the features clearly. It was found the counts in the 237 channel increased from 73.49 ± 7.81 to 149.17 ± 6.34. The overlap of the uranium signal into the 237 channel is dependent on the laser power density applied to the material. The ratio of $^{237}Np/^{238}U$ counts ranges from 8.46E-05 to 1.47E-05.

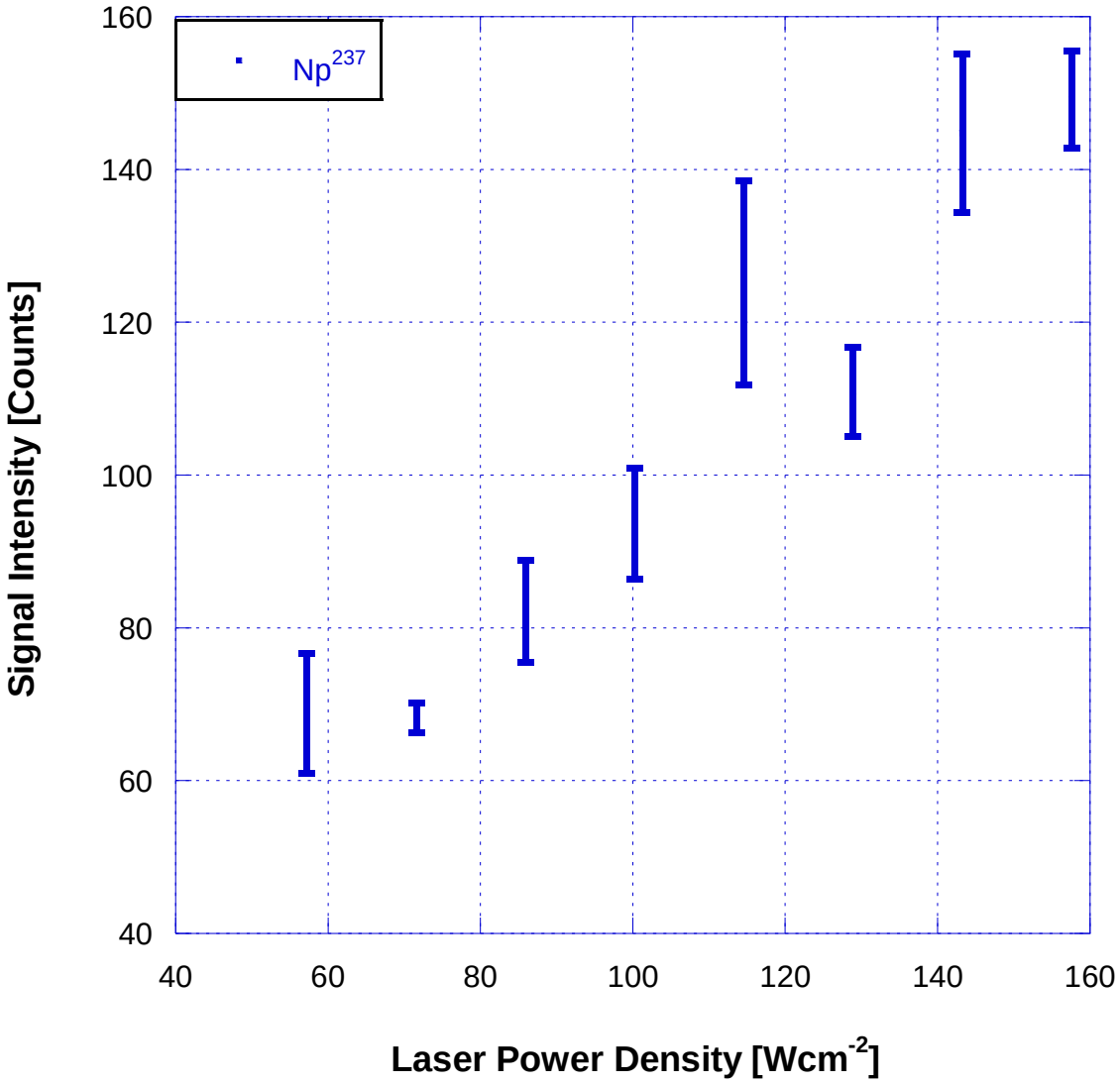

Figure 29: ^{237}Np signal in Laser Power Study using 100% $^{238}UO_2$ Pellet

A second laser power study was performed using a NIST 610 glass standard as the ^{238}U source and an iCAP-Q ICP-MS with a New Wave NWR-213 laser ablation system. This system has the capability of simultaneously measuring in peak hopping mode and mass scan survey. The results for the ^{239}Pu and ^{237}Np are shown in Figure 30 using helium as the carrier gas. Although the average power densities in this study are higher than previous studies in this work (Figure 27 and Figure 28), the resulting $^{239}Pu/^{238}U$ ranged from 8.53E-05 to 1.27E-04. The uranium counts in this study were 2.2E07 which are in the same order of magnitude as the uranium oxide pellet measured with ELAN DRC II ICP-MS. The significantly higher $^{239}Pu/^{238}U$ ratio in this study can be explained in Figure 31. The signal at m/z 239.052 is not peak tailing but a $^{238}UH^{+}$ formation.

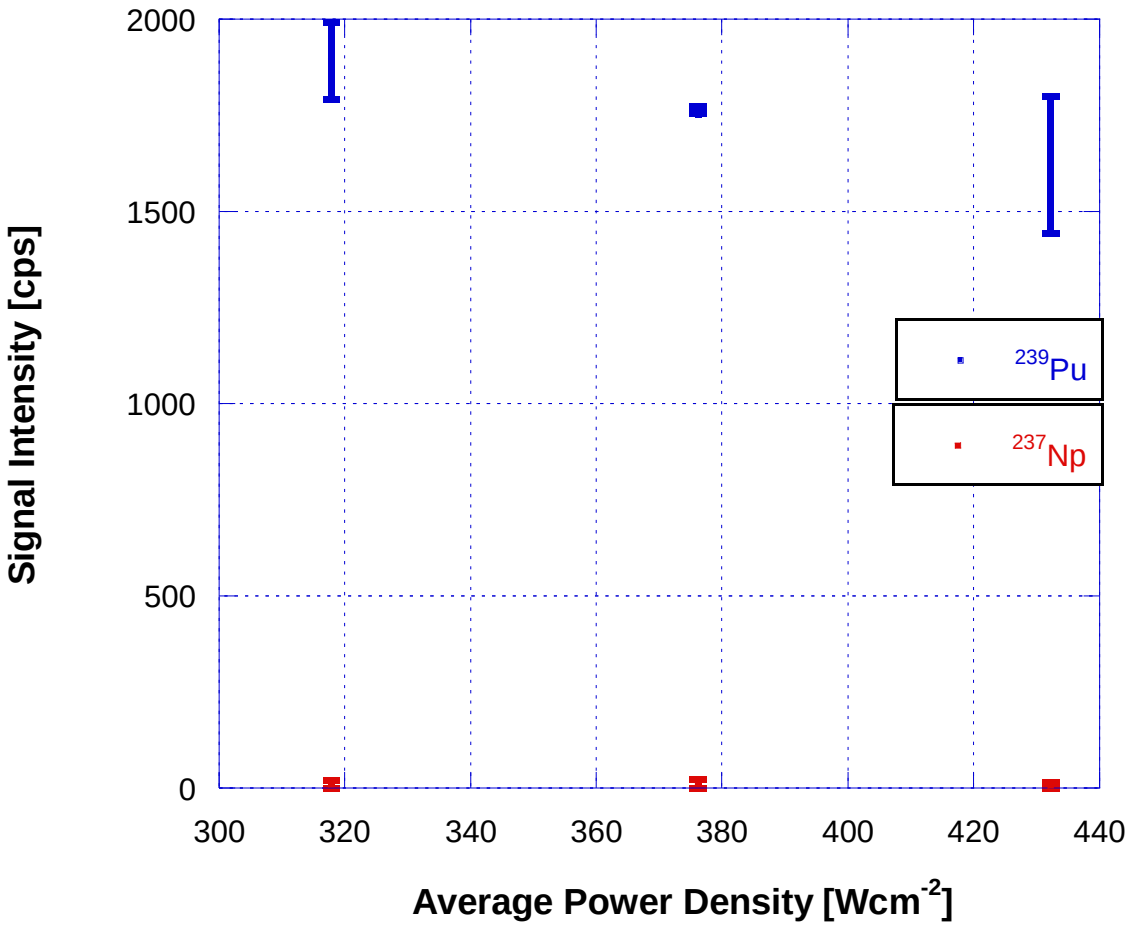

Figure 30: ^{239}Pu and ^{237}Np signals using NIST 610 glass standard iCAP-Q ICP-MS with He as carrier gas

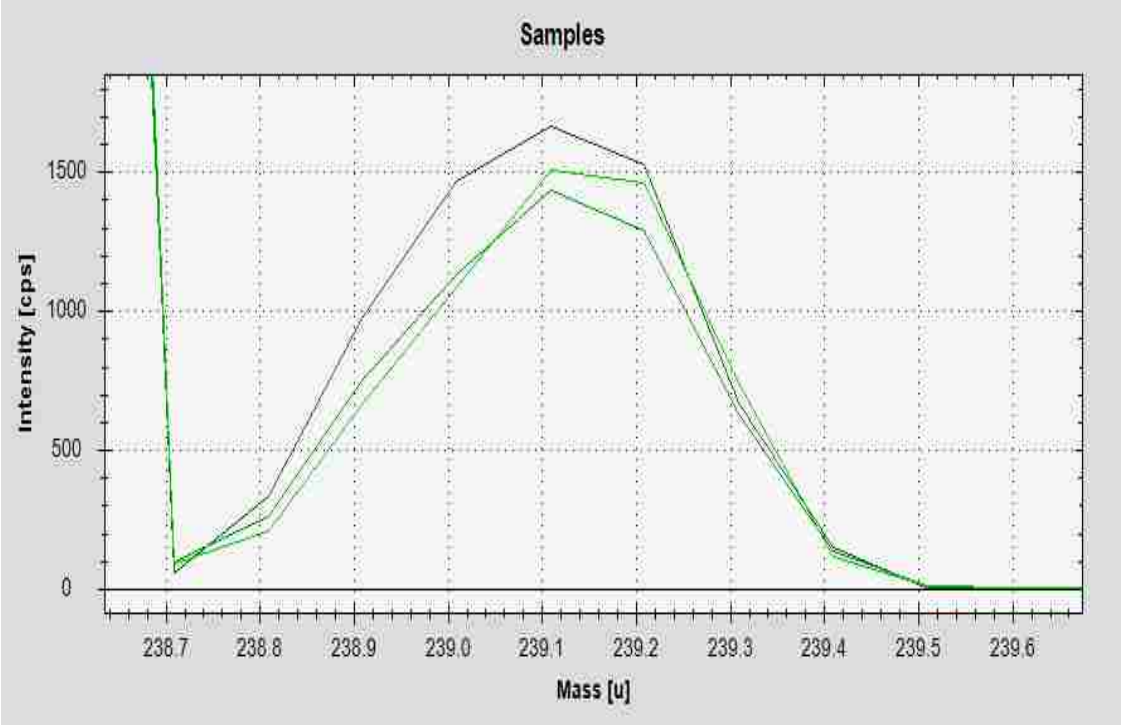

Figure 31: Mass scan survey in second laser power density study using He as carrier gas

The iCAP-Q-ICP-MS also has the ability to analyze in KED mode. The KED mode is a kinetic energy discrimination collision cell using helium as a pressurized gas. This cell breaks molecular bonds formed in the plasma. Figure 32 shows the resulting ^{239}Pu and ^{237}Np signals using helium carrier gas and activated KED mode.

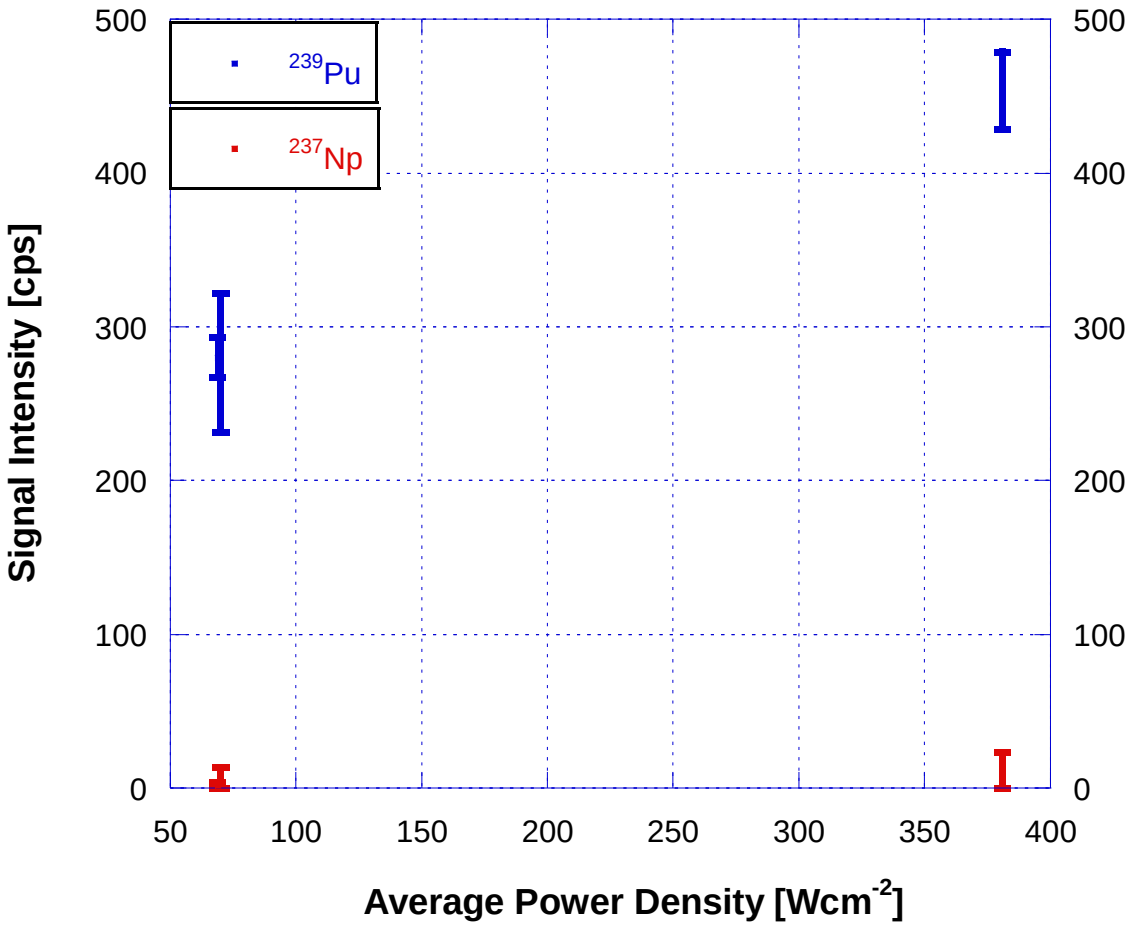

Figure 32: ^{239}Pu and ^{237}Np signals in second Laser Power Study using He as carrier gas and KED mode

The KED mode successfully lowered the ^{239}Pu/^{238}U ratio ranging from 2.77E-05 to 2.85E-05 from the helium mode on the same instrument (Table 20). The KED collision cell also lowered the ^{238}U signal to 1.6E06 from 2.2E07. The mass scan survey also showed a second peak forming at the m/z 239.052 which suggests a hydride is still reaching the detector.

Instrument	Carrier gas	$^{237}Np/^{238}U$	$^{239}Pu/^{238}U$
Elan DRC II	Ar	8.46E-05 - 1.47E-05	6.88E-06 - 6.45E-05
iCAP Q	He	8.42E-07 - 2.98E-07	8.53E-05 - 1.27E-04
iCAP Q	He KED mode	7.36E-07 - 1.65E-07	2.77E-05 - 2.85E-05
iCAP Q	Ar	ND - 2.2E-06	6.46E-05 - 8.77E-05

Table 20: Comparison of the $^{237}Np/^{238}U$ and $^{239}Pu/^{238}U$ ratios with ICP-MS instruments and carrier gases

To limit the hydride formation assuming the hydrogen source is from the He carrier gas, argon was used as the carrier gas (Figure 33). The $^{239}Pu/^{238}U$ ratio ranged from 6.46E-05 to 8.77E-05. These results are closer to the carry over observed in the ELAN DRC II measurements with the $^{237}Np/^{238}U$ ratio using argon as the carrier gas (Table 20).

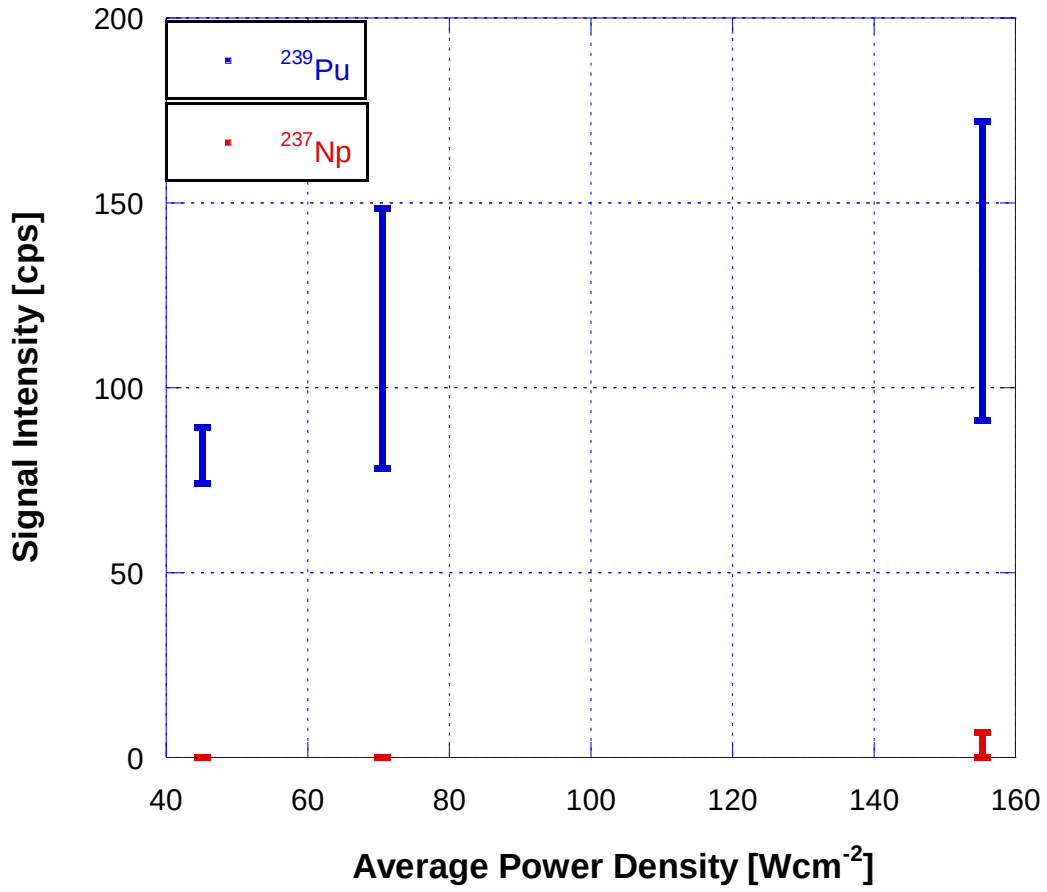

Figure 33: ^{239}Pu and ^{237}Np signals in second Laser Power Study using Ar as carrier gas

The difference in carry-over of the tails can be explained in the graphical representation of signal intensity for different AMU (Figure 34) showing the different point of analysis of each ICP-MS tested along with the theoretical point of analysis. As shown in Figure 34, the top left would be the ideal point of analysis for the quadrupole detector where the point is at the peak maximum and the tails end at ± 1 amu. The top right is what is observed for the iCAP-Q-ICP-MS where the right tail would overlap into the m/z 239.052 resulting in higher background counts regardless of hydride formation. The bottom left is

what is observed for the Perkin Elmer ELAN DRC II used for analysis. With the analysis shifted to the right the left tail would then overlap into the m/z 237.048. While machines have been mass calibrated prior to analysis, it appears small tailing is inevitable with quadrupole detectors. The relationship increases with increasing laser power density due to the relationship with power density and signal intensity. As signal intensity increases the broadening increases.

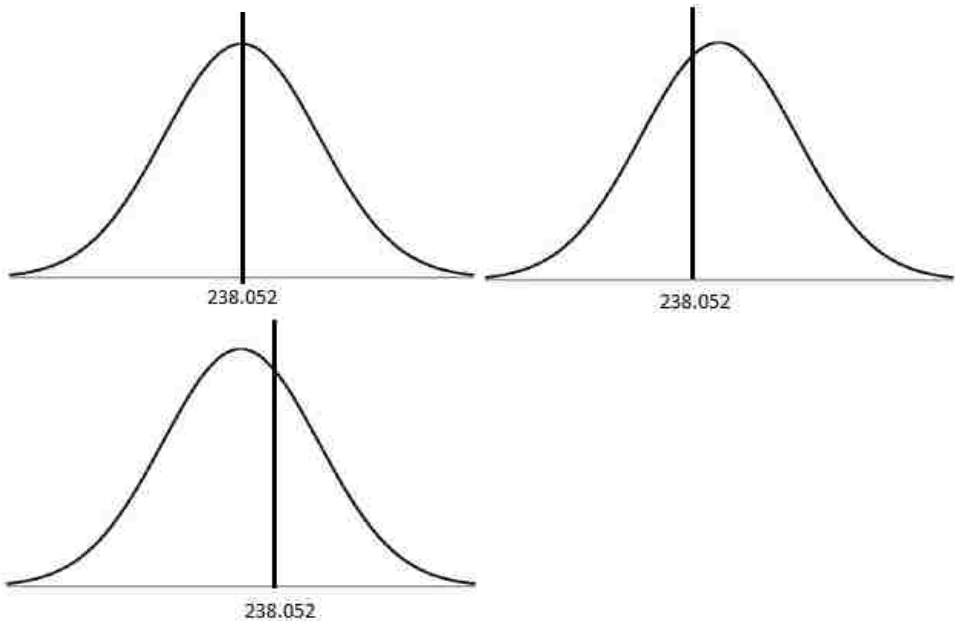

Figure 34: Graphical representation of a ^{238}U ICP-MS signal. Top left is the theoretical point of analysis, Top right is the analysis point for the iCAP-Q-ICP-MS and the bottom left is the analysis point for the Perkin Elmer ELAN DRC II ICP-MS

5.4.5 Quantification of ^{237}Np and ^{239}Pu in UO_2 matrix

Figure 35 shows the quantitative results of ^{239}Pu concentrations ranging from 0.5 to 1.02 wt% in a uranium oxide matrix with instrument parameters listed in Table 13. Linearity was achieved with a correlation factor of 0.9992 and the relative standard deviation for three runs varied from 3.7 to 9.6%. The concentration of plutonium in these samples directly correlates with burn-up rates between 13 and 39 $MWdkg^{-1}$ which are of interest to nuclear safeguards. The average power density used in this study was lower than the laser power study (Figure 26) of 38.197 Wcm^{-2}, indicating no overlap from the uranium signal and no correction needed. The overall area sampled per run was 0.0225 mm^2, which suggests that the method is minimally destructive for determining plutonium concentration within the samples.

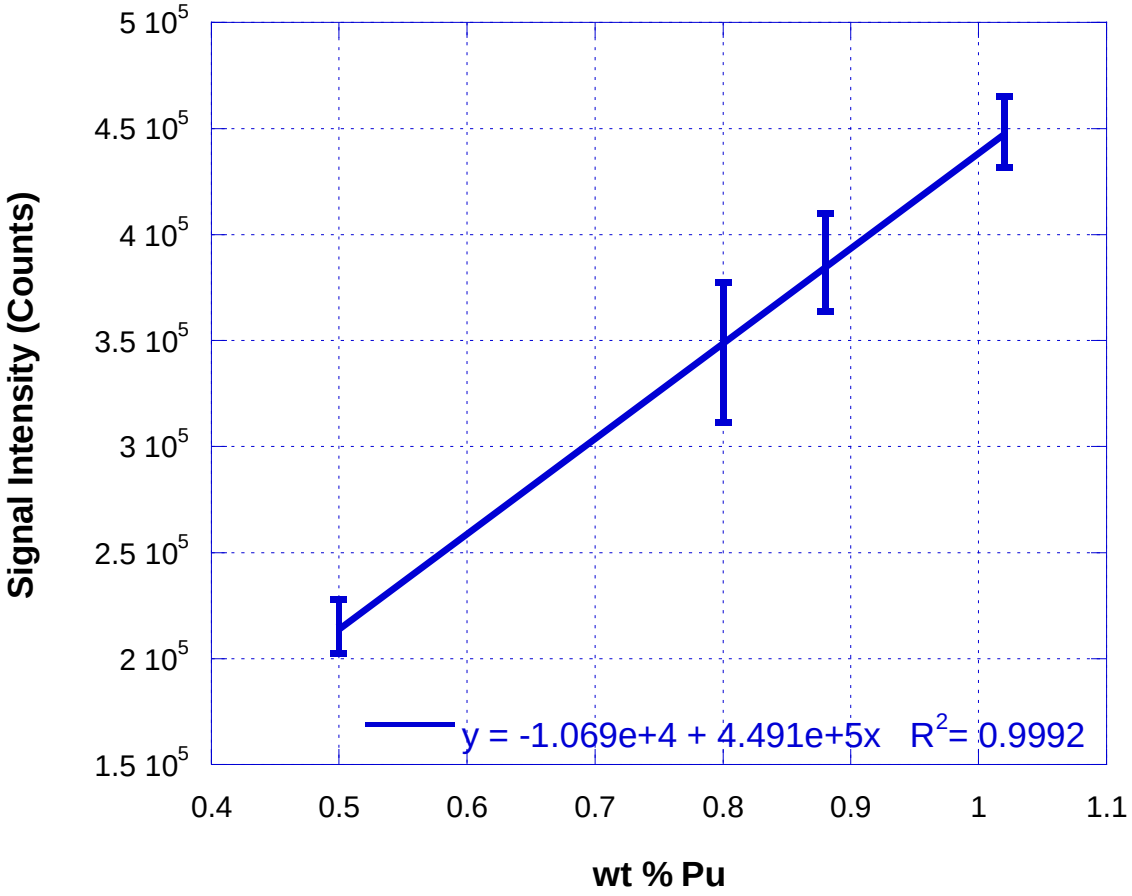

Figure 35: LA-ICP-MS Results for Analysis of ^{239}Pu in (U,Pu)O_2 pellets

Figure 36 shows the calibration curve obtained for the (U,Np)O_2 series with LA-ICP-MS conditions listed in Table 14. The linear correlation value obtained was 0.995. The pellets were measured in 4 replicates with relative standard deviation ranging from 3.9-8.9%. The 0.75 wt % neptunium has the highest %RSD. The laser power density used in this study was 31.821 Wcm^{-2} ensuring conditions with no tail overlap; therefore no correction factor is needed.

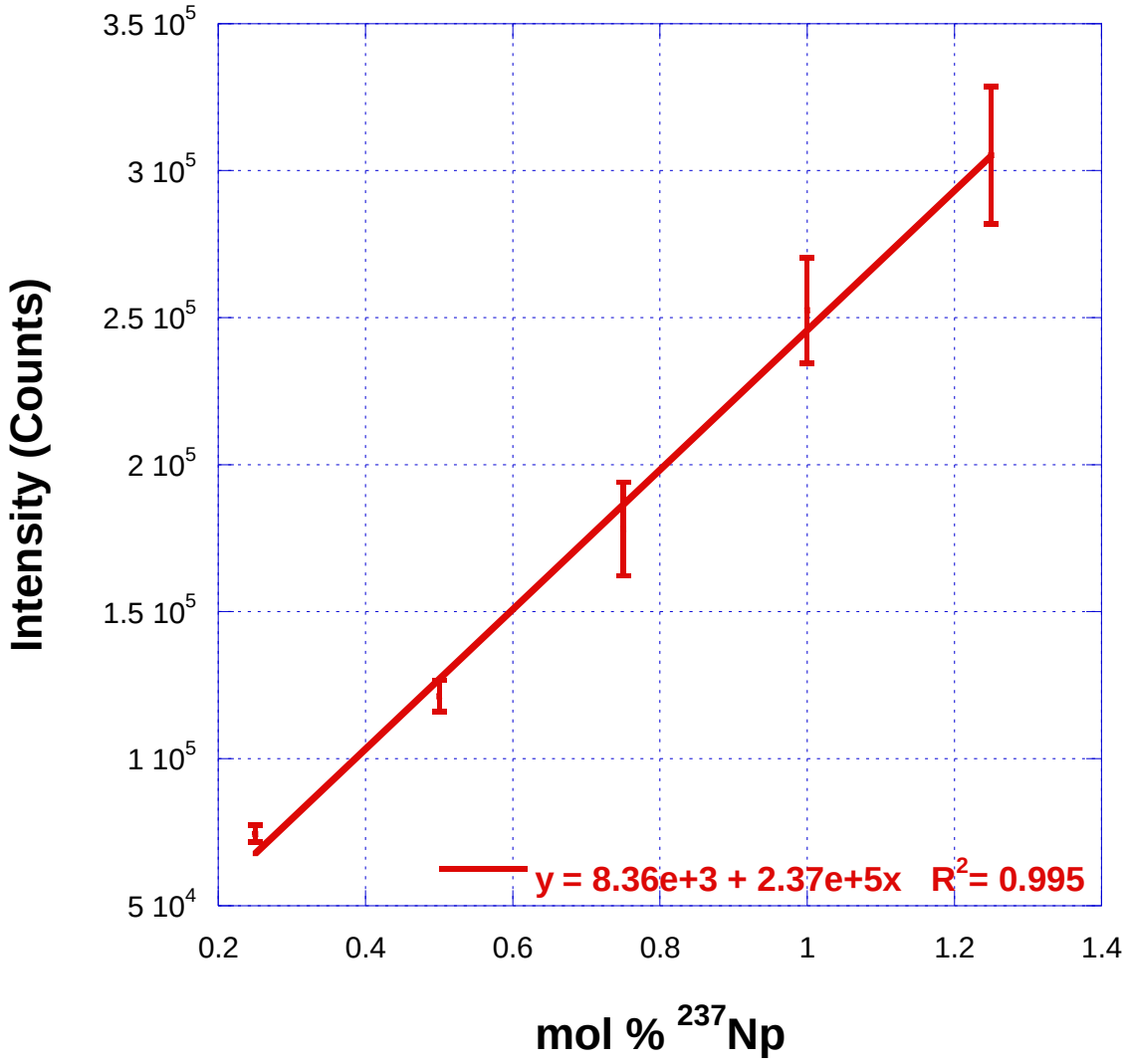

Figure 36: LA-ICP-MS Results for Analysis of ^{237}Np in $(U,Np)O_2$ pellets

5.5 Conclusion

The co-precipitation of uranium and plutonium using 2 mL of ammonium hydroxide saturated with oxalate precipitated 99.4% of the metal ions in solution with contact time of 10 minutes. The pellets prepared were highly crystalline,

single face centered cubic phase of $(U,Pu)O_2$, verifying the sintering profile of 5 hours at 1700°C was sufficient. The theoretical densities of the $(U,Pu)O_2$ pellets exceed 85% with the highest measured at 93.5%. Two pellets had lateral cracks most likely from the pressing stage of preparation.

The autoclave synthesis of neptunium dioxide in 8M nitric acid effectively converted all the material to Np(VI) confirmed by UV-Vis spectroscopy and LSC. The pellet preparation produced high theoretical densities. The average theoretical density was found to be 88.33 ± 2.16%. All the pellets contained two face centered cubic phases. In order to obtain a single solid solution the sintering parameters would need to be optimized by increasing the sintering time in order for the neptunium to diffuse throughout the pellet.

Two saturation studies with a uranium source were completed to understand spectroscopic interferences. It was found using helium as the carrier gas the $^{239}Pu/^{238}U$ count ratio ranged from 8.53E-05 to 1.27E-04. The significantly higher $^{239}Pu/^{238}U$ ratio in this study is not peak tailing but a $^{238}UH^+$ formation confirmed by a mass scan survey. The KED mode successfully lowered the $^{239}Pu/^{238}U$ ratio ranging from 2.77E-05 to 2.85E-05, also lowering the ^{238}U signal to 1.6E06. The mass scan survey also showed a second peak forming at the m/z 239.052 which suggests a hydride is still reaching the detector. To limit the hydride formation, assuming the hydrogen source is from the helium carrier gas. With argon as the carrier gas the $^{239}Pu/^{238}U$ ratio ranged from 6.46E-05 to 8.77E-05. These results are closer to the carry over observed with the ELAN DRC

II ICP-MS with the $^{237}Np/^{238}U$ ratio. The difference in carry over can be explained by the location the quadrupole in assigning the channel for measurement. If the channel is to the left of the peak maximum the carry over counts will be +1 amu. If the channel is to the right of the peak maximum, the carry over counts will be -1 amu. The relationship increases with increasing laser power density due to the relationship with power density and signal intensity. As signal intensity increases the broadening increases.

Laser Ablation-Inductively Coupled Plasma-Mass Spectrometry successfully measured plutonium in a uranium oxide matrix with a linear correlation factor of 0.9992 and the relative standard deviation for three runs varied from 3.7 to 9.6%. No signal overlap was observed from the bulk uranium. The LA-ICP-MS parameters were successful in obtaining a linear correlation value of 0.995 and low percent relative standard deviations ranging from 3.9-8.9% for neptunium in a uranium oxide matrix. Although overlap in the 237 channel was observed, during analysis laser power density was kept below this feature to ensure no corrections needed. Each series was measured and analyzed within an hour, which suggests a more rapid analytical technique than current methods used to quantify plutonium and neptunium in a uranium matrix. Laser Ablation-Inductively Couple Plasma-Mass Spectrometry also minimizes the handling of potentially hazardous material and reduces waste generation by directly ablating the solid. This technique could be applied to fresh or used fuel to quantify plutonium and neptunium for safeguards or forensic purposes.

Chapter 6 – Synthesis, characterization and measurement of $(U,Zr)O_2$ and $(U,Zr,Ce)O_2$

6.1 Abstract

Dissolution procedures for uranium and zirconium oxides are often tedious and require lengthy periods of time for complete dissolution. This can be problematic when determining the zirconium concentration in a sample. This study developed a quantitative technique for measuring zirconium in a uranium dioxide matrix without the need to dissolve the material. The linear correlation value for zirconium in a uranium dioxide matrix was found to be 0.9963 with relative standard deviation ranges from 8.0 to 14.0 %. The concentration range of zirconium from 2.4 to 23.6 mole percent is the widest tested that resulted in an acceptable linear correlation value. A second set of materials with cerium oxide is also analyzed to determine limitations on accuracy and precision of LA-ICP-MS while simultaneously measuring two analytes. The $(U,Zr,Ce)O_2$ pellets model the main oxide phase of used nuclear fuel. The zirconium results for the simultaneous analysis of zirconium and cerium in $(U,Zr,Ce)O_2$ pellets were found to be linear correlation of 0.9795 with relative standard deviation ranging from 6.8 % to 20.9 %. The cerium linear correlation is 0.985 with relative standard deviation ranging from 5.2 % to 22.9 %. The zirconium concentration in the $(U,Zr,Ce)O_2$ varied from 2.82 to 12.84 mole %. The cerium concentration ranged

from 2.4 to 11.2 mole %. When optimizing laser conditions for two different elements, loss of accuracy in the linear correlation value is observed.

6.2 Introduction

There has been extensive amount of research on the $(U,Zr)O_2$ matrices (62, 63, 64, 65, 66, 67, 68). Zirconium is one of the major fission products as well as a main component in zircaloy cladding. Zirconium dioxide is also studied as a component for a mixed oxide fuel inert matrix. Based on these considerations relevant concentrations of zirconium in $(U,Zr)O_2$ range from 0.1 to 95 weight percent.

Fuel-cladding interaction is important in determining reactor and fuel performance evaluations. Fission products depositing on the surface of the cladding causing stress corrosion cracking is suspected as one of the mechanism for cladding failure (51). The majority of nuclear fuel used today consists of a uranium dioxide pellets contained in a sealed tube of zirconium alloy to make a fuel rod with variations on how the rods are assembled in the reactor. The two common zirconium alloys are Zircaloy, which is a zirconium-tin alloy with about 1.5% tin (62), and E110 and E635 which are alloys of zirconium with about 1% niobium (63). Studies of fuel-cladding interaction are often diffusion experiments (64, 65). The concentration of zirconium diffusing into the uranium dioxide

matrices in these studies around 10 weight percent and is highly dependent on oxygen concentration.

Previous studies examined the addition of an inert zirconium oxide to enhance the chemical stability and radiation resistance of nuclear fuel (66).The addition of zirconia into mixed oxide and thorium-uranium fuels has been shown to increase the durability of the fuel and the bonding between the phases (67). These fuels tend to have uranium concentrations from 5 to 20 weight percent (68) with the remaining material as zirconia with other additives.

The purpose of this study is to develop a quantitative technique for measuring zirconium in a uranium dioxide matrix without the need to dissolve the material. Nuclear fuels must be assayed, whether destructive or non-destructive, for safeguard purposes to ensure accountability and correct compound composition. This is an issue in regards to zirconium dioxide which necessitates the use of potentially hazardous reagents such as hydrofluoric acid for dissolution in destructive assay (69). A second set of materials including cerium oxide is also analyzed to determine limitations on accuracy and precision of LA-ICP-MS while simultaneously measuring two analytes. The $(U,Zr,Ce)O_2$ pellets model the main oxide phase of used nuclear fuel (51).

6.3 Experimental

The $(U,Zr)O_2$ and $(U,Zr,Ce)O_2$ were prepared as described in section 2.1. The concentration of cerium, zirconium and uranium for these matrices are listed in Table 21. The concentration of the zirconium in $(U,Zr)O_2$ are in the range of used nuclear fuel as well as fuel-cladding interaction experiments. The concentration of zirconium and cerium in the ternary oxide pellets are consistent with what is found in used nuclear fuel with burn up rates up to 65 MWd/kg (51).

mol% U	mol% Zr
97.60	2.40
95.20	4.80
88.70	11.30
93.80	6.20
76.40	23.60

mol% U	mol% Ce	mol% Zr
94.8	2.4	2.8
89.4	5.0	5.7
83.1	7.9	9.0
76.0	11.2	12.8

Table 21: Concentration of $(U,Zr)O_2$ pellets (left), Concentration of $(U,Zr,Ce)O_2$ pellets (right)

Prior to laser ablation analysis the pellets densities and phase composition were characterized. The densities were measured using a digital balance and calipers and compared to the theoretical densities. The phase composition was

determined using powder XRD with the preparation and parameters described in section 2.2.1.

Table 22 lists the optimal LA-ICP-MS parameters used to determine zirconium in a uranium oxide matrix. Only the ^{90}Zr (m/z = 89.9043) is collected in the ICP-MS detector. The pellets were each ablated for 40 seconds with replicates of four in different areas on the pellet surface. Each ablation including blank collection is a total collection time of 90 seconds. The signal was then integrated and normalized for time of integration. All of the data collected in this study used peak-hopping mode for the ICP-MS. The optimized average laser power density for the zirconium analysis was found to be 114.592 Wcm^{-2} which is the highest of all power densities tested.

Laser Ablation	
Spot size	100 µm
Time per scan	40 sec
Scan rate	5 $\mu msec^{-1}$
Gas blank	30 sec
Avg Power Density	114.592 Wcm^{-2}
Pulse Rep Rate	5 Hz
ICP-MS	
RF Power	1050 W
Lens Voltage	5.5 V
Analog Stage Voltage	-1700 V
Pulse Stage Voltage	825 V
Sweeps	10
Readings	600
Dwell Time	8 ms
Neb flow (Ar)	0.8 $Lmin^{-1}$

Table 22: LA-ICP-MS parameters for (U,Zr)O2 measurements

Table 23 shows the relevant parameters used to measure the $(U,Zr,Ce)O_2$ pellets. The optimized average laser power density was 100.268 Wcm^{-2}. This laser power density falls between those used for the optimized analysis of each element separately. The cerium analysis is listed in Table 5 with power density 85.944 Wcm^{-2} and the zirconium analysis listed in Table 22 with 114.592 Wcm^{-2}. The m/z measured in this study was 89.9043 for zirconium and 139.905 for cerium leaving the uranium to be filtered within the ion beam. The pellets were each ablated for 40 seconds and three times in different areas with the signal collection time of 90 seconds. The signal was then integrated and normalized for time of integration.

Laser Ablation	
Spot size	100 µm
Time per scan	40 sec
Scan rate	5 $\mu msec^{-1}$
Gas blank	20 sec
Avg Power Density	100.268 Wcm^{-2}
Pulse Rep Rate	5 Hz
ICP-MS	
RF Power	1100 W
Lens Voltage	5.5 V
Analog Stage Voltage	-1700 V
Pulse Stage Voltage	825 V
Sweeps	10
Readings	600
Dwell Time	8 ms
Neb flow (Ar)	0.95 $Lmin^{-1}$

Table 23: LA-ICP-MS parameters for $(U,Zr,Ce)O_2$ measurements

6.4 Results

6.4.1 Density Measurements

The density measurements for the $(U,Zr)O_2$ pellets are listed in Table 24. The theoretical densities range from 71.27 ± 1.99% to 88.60 ± 2.72% with an average of 82.67 ± 6.69%. The 4.8 mol% zirconium is an outlier with the lowest theoretical density.

mol% Zr	Measured ρ [g cm^{-3}]	Theoretical ρ [g cm^{-3}]	%Theoretical ρ
2.4	9.247 ± 0.237	10.843	85.28 ± 2.56
4.8	7.638 ± 0.152	10.716	71.27 ± 1.99
6.2	9.429 ± 0.256	10.642	88.60 ± 2.72
11.3	8.853 ± 0.219	10.372	85.36 ± 2.47
23.6	8.052 ± 0.193	9.722	82.83 ± 2.40

Table 24: Density measurements for $(U,Zr)O_2$ pellets

After sintering the 4.8 mol % $(U,Zr)O_2$ pellet expanded and cracked on one side shown in Figure 37. These cracks do not cross the entire pellet, leaving the pellet intact but deformed, resulting in a low theoretical density. These physical defects would seem to be a manufacturing malfunction instead of a chemical reaction within the pellet. When excess pressure is applied to the green

pellet during ejection from the pressing die lateral weakness in the structure is expected (70).

Figure 37: Image of side cracks 4.8 mol% Zr (U,Zr)O_2 pellet using Leica DM 2500P Microscope

The density measurements for the (U,Zr,Ce)O_2 pellets are listed in Table 25. The theoretical densities range from 73.20 ± 3.56% to 81.69 ± 3.12% with an average of 76.84 ± 3.55%. This is by far the lowest average theoretical density for an entire series. These pellets are more porous than other matrices with an average pore size of 66.2 ± 21.3 μm.

mol% U	Measured ρ [g cm^{-3}]	Theoretical ρ [g cm^{-3}]	%Theoretical ρ
94.8	8.157 ± 0.196	10.843	75.93 ± 2.40
89.3	7.688 ± 0.274	10.716	73.20 ± 3.56
83.1	7.829 ± 0.228	10.642	76.52 ± 2.91
76.0	8.105 ± 0.253	10.372	81.69 ± 3.12

Table 25: Density measurements for (U,Zr,Ce)O_2 pellets

6.4.2 Powder XRD Results

The chemical homogeneity and phase composition of the synthesized pellets are characterized using powder XRD. This determination is important to understand if the pellets are homogenous within the sampling area of the laser ablation. The goal is to have a single phase solid solution to ensure the micron sampling area is representative of the bulk of the sample.

An example of the (U,Zr)O_2 powder XRD pattern is shown in Figure 38. The blue line is the measured pattern, the red is the calculated pattern and the grey is the difference between measured and calculated. There are two face centered cubic phases observed for these matrices. The uranium rich (U,Zr)O_2 phase is the main peak in the pattern. The zirconium rich (U,Zr)O_2 phase appears as a shoulder on the main peak at low 2 theta °, below 60 ° and is separated and more defined from the main peak at 2 theta ° above 75 °. This is due to the difference in ionic radius of uranium and zirconium. Since zirconium

has a smaller ionic radius, the d-spacing of the zirconium rich phase is smaller resulting in a smaller lattice parameter.

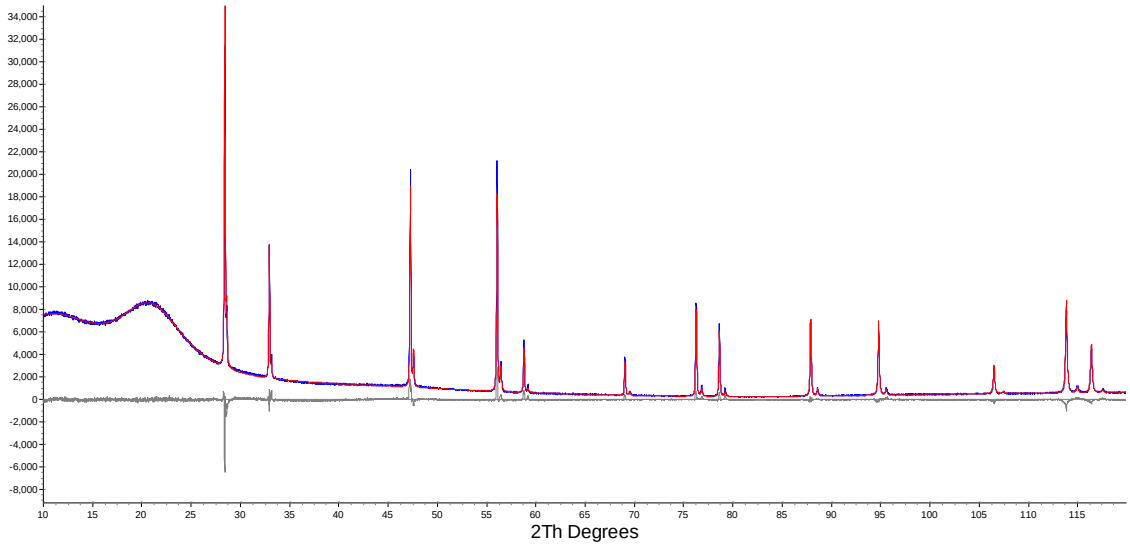

Figure 38: Powder XRD pattern for 11.3 mol% Zr $(U,Zr)O_2$ pellet

The breakdown of the phase composition for the uranium rich and zirconium rich solid solutions are listed in Table 26. All of the pellets have two phases except for the 6.2 mol% zirconium which is a single solid solution. The synthesis procedure, sintering time, and temperature were the same throughout the series. It is unclear why the 6.2 mol% zirconium is the only matrix that is a single solid solution. Schleifer et. al. found that annealing period of 200 hours at 1670 K with a reducing atmosphere is needed to obtain a pure $(U,Zr)O_2$ solid

solution in a zirconia rich sample (11). This annealing period is excessive and not needed for laser ablation sampling since the zirconium is distributed throughout the pellet.

mol% Zr	$(U,Zr)O_2$ U Rich (phase %)	$(U,Zr)O_2$ Zr Rich (phase %)	R_{wp}
2.4	77.3	22.7	4.81
4.8	74.56	25.44	5.24
6.2	100	0	5.59
11.3	64.29	35.71	5.43
23.6	23.02	76.98	7.44

Table 26: Phase analysis of pellets in the $(U,Zr)O_2$ system by Rietveld structure refinement

An example of the ternary oxide powder XRD pattern is shown in Figure 39 with the phases of the two face centered cubic phases identified listed in Table 27. The major $(U,Zr,Ce)O_2$ phase contains more uranium than zirconium and cerium. The minor $(U,Zr,Ce)O_2$ phase contains more zirconium and cerium than the major phase. The pellets are more than 90% the major phase with the exception of the 83.1 mol% uranium pellet. The minor phase appears as a shoulder in the XRD pattern and is in small quantities throughout the series. A longer sintering time should diffuse the remaining minor phase resulting in a single solid solution.

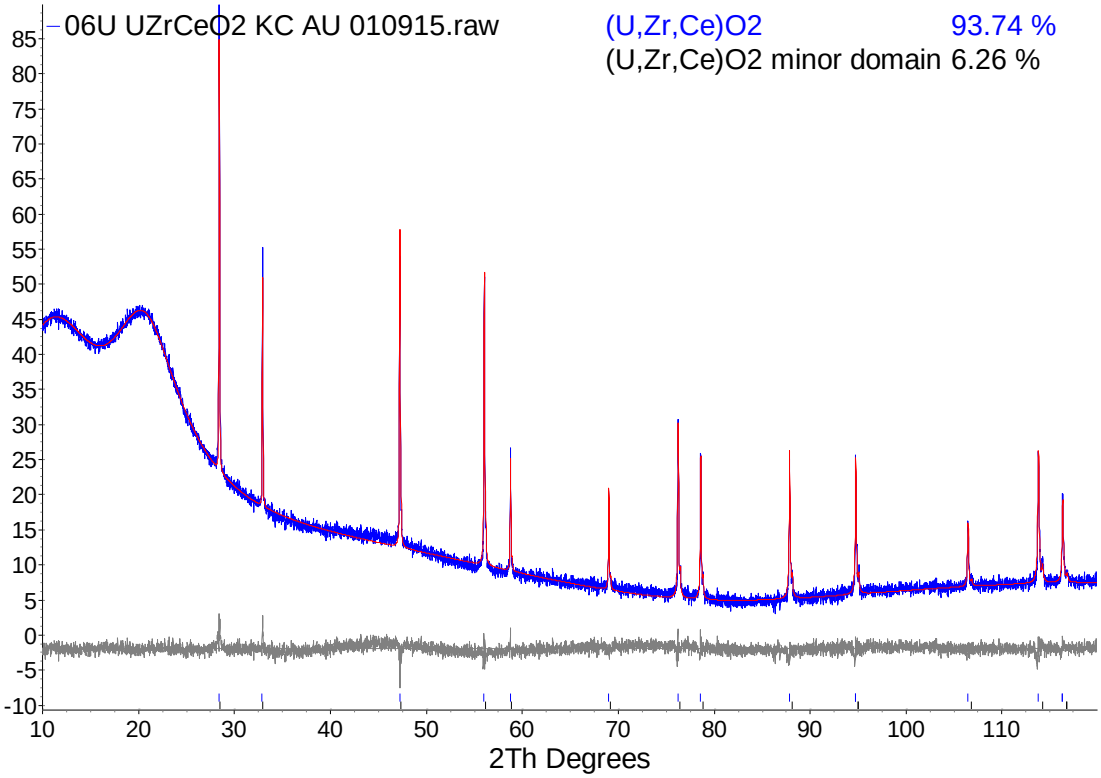

Figure 39: Powder XRD pattern for 76.0 mol% U (U,Zr,Ce)O_2 pellet

mol% U	Major (U,Zr,Ce)O_2 phase %	Minor (U,Zr,Ce)O_2 phase %
94.8	93.74	6.26
89.3	95.15	4.85
83.1	84.85	15.15
76.0	95.75	4.25

Table 27: Phase analysis of pellets in the (U,Zr,Ce)O_2 system by Rietveld structure refinement

6.4.3 LA-ICP-MS Analysis

The calibration curve for zirconium in $(U,Zr)O_2$ matrix is displayed in Figure 40. The linear correlation value was found to be 0.9963 with relative standard deviation ranges from 8.0 to 14.0 %. The average relative standard deviation is 11.9 ± 2.5%. The concentration range of zirconium from 2.4 to 23.6 mole percent is the widest range tested that resulted in an acceptable linear correlation value above 0.99.

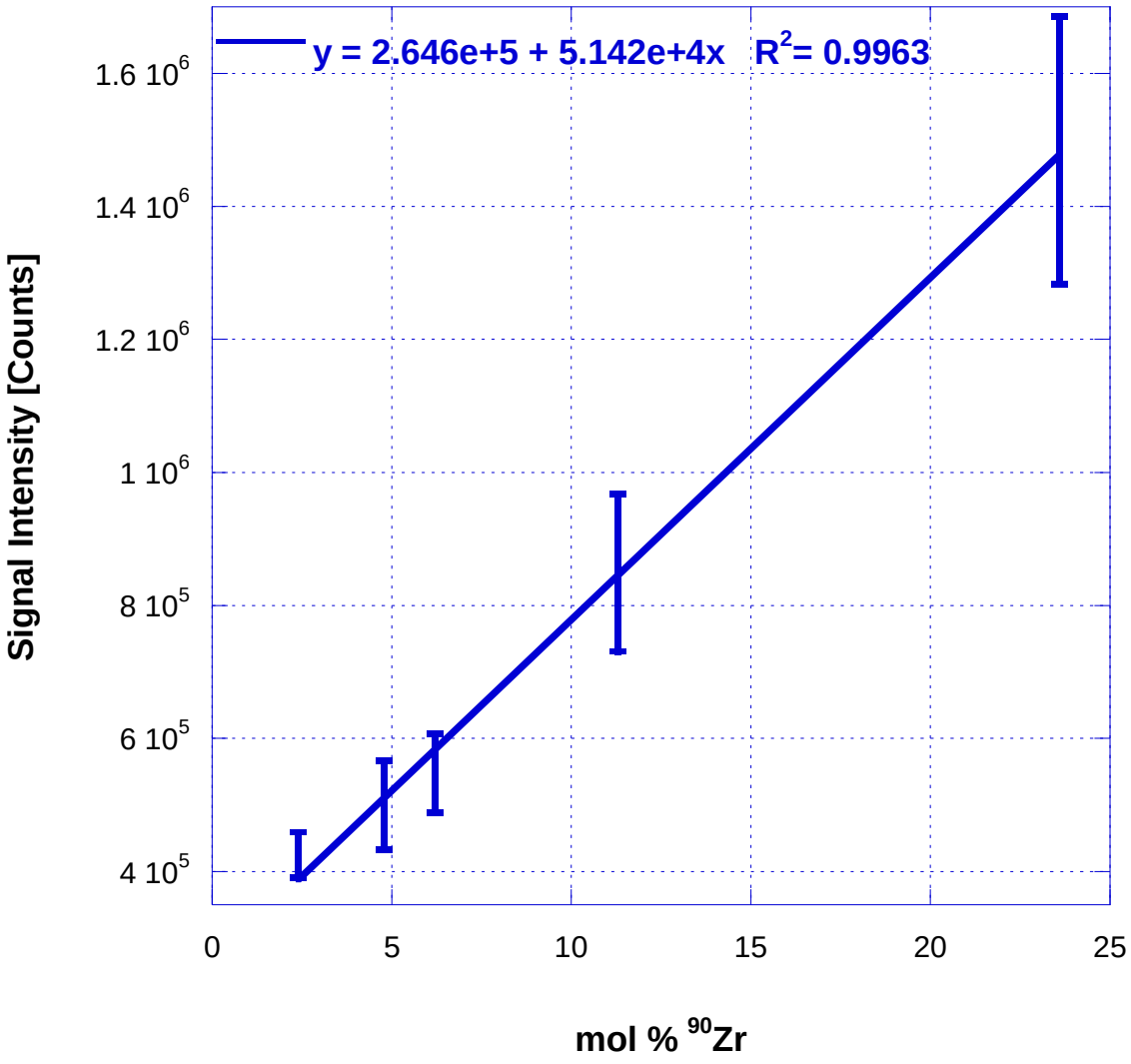

Figure 40: LA-ICP-MS results for $(U,Zr)O_2$ series

The zirconium results for the simultaneous analysis of zirconium and cerium in $(U,Zr,Ce)O_2$ pellets are shown in Figure 41. The linear correlation is 0.9795 with relative standard deviation ranging from 6.8 % to 20.9 %. The zirconium concentration varied from 2.82 to 12.84 mole %. The average laser

power density in this study of 100.268 Wcm^{-2} is lower than optimization of zirconium at 114.592 Wcm^{-2}.

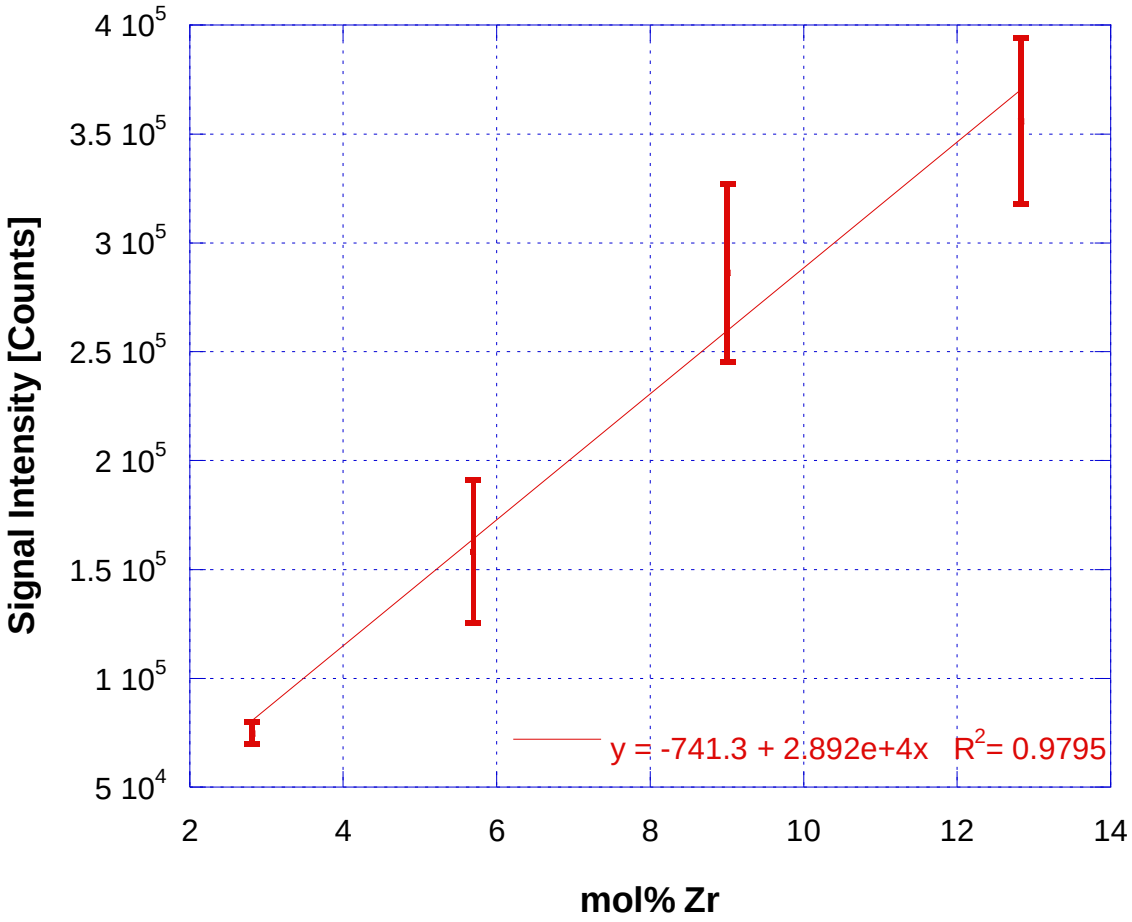

Figure 41: LA-ICP-MS results for trace Zr in $(U,Zr,Ce)O_2$ pellets

The cerium results for the simultaneous analysis of zirconium and cerium in $(U,Zr,Ce)O_2$ pellets are shown in Figure 42. The linear correlation was found to be 0.985 with relative standard deviation ranging from 5.2 % to 22.9 %. The linear correlation value is higher for cerium than zirconium. The cerium

concentration ranged from 2.4 to 11.2 mole %. The average laser power density of 100.268 Wcm^{-2} in this study is significantly higher than the average laser power density for cerium at 85.944 Wcm^{-2}.

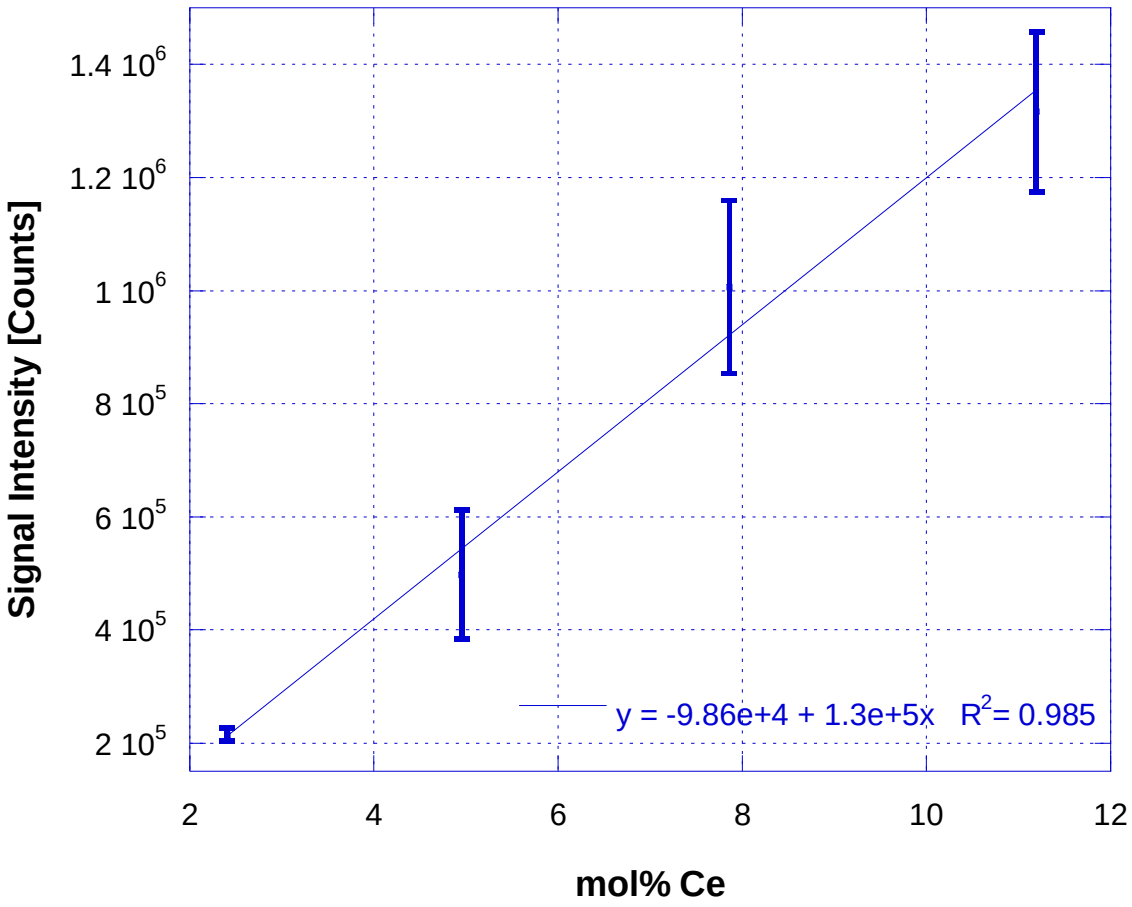

Figure 42: LA-ICP-MS results for trace Ce in $(U,Zr,Ce)O_2$ pellets

6.5 Conclusion

The co-precipitation method for synthesizing $(U,Zr)O_2$ and $(U,Zr,Ce)O_2$ was successful in producing solid solutions of each matrices. Longer sintering times would produce a single solid solution for each matrices than the two solid solutions measured for both $(U,Zr)O_2$ and $(U,Zr,Ce)O_2$ pellets. The theoretical densities of the $(U,Zr)O_2$ pellets ranged from 71.27 ± 1.99% to 88.60 ± 2.72% with an average of 82.67 ± 6.69%. The theoretical densities of the $(U,Zr,Ce)O_2$ ranged from 73.20 ± 3.56% to 81.69 ± 3.12% with an average of 76.84 ± 3.55%. This is by far the lowest average percent theoretical density made for an entire series. The low theoretical densities result in larger pits and voids in the pellets correlating with large relative standard deviations. The pellets with zirconium doped are more porous and had physical defects in the materials such as lateral cracks observed.

The linear correlation value for zirconium in a uranium oxide matrix was found to be 0.9963 with relative standard deviation ranges from 8.0 to 14.0 %. The concentration range of zirconium from 2.4 to 23.6 mole % is the widest range tested that resulted in an acceptable linear correlation value. The average power density needed to ablate zirconium is higher than the other elements in this work, suggesting zirconium oxide needs more energy to vaporize than cerium, uranium, neptunium or plutonium

The zirconium results for the simultaneous analysis of zirconium and cerium in $(U,Zr,Ce)O_2$ pellets were found to be linear correlation of 0.9795 with relative standard deviation ranging from 6.8 % to 20.9 %. The cerium linear correlation is 0.985 with relative standard deviation ranging from 5.2 % to 22.9 %. The zirconium concentration varied from 2.82 to 12.84 mole percent. The cerium concentration ranged from 2.4 to 11.2 mole percent. The porosity of the material affects the precision of the laser ablation measurements resulting in high relative standard deviation for this series.

The average laser power density in the $(U,Zr,Ce)O_2$ pellets of 100.268 Wcm^{-2} is lower than just the optimization of zirconium in previous work of 114.592 Wcm^{-2} and higher than the average laser power density of just optimizing for cerium in previous studies of 85.944 Wcm^{-2}. The average laser power density for the analysis of both elements fell between the optimization values for either element, but skewed to the higher value in order to ablate zirconium successfully. When optimizing laser conditions for two different elements, loss of accuracy in the linear correlation value is observed.

Chapter 7 – Effects of Laser Ablation on Uranium Oxides

7.1 Abstract

The ablation zone is examined for any chemical or physical changes in the material to determine the effects of LA-ICP-MS. This study will classify the technique as destructive or non-destructive and determine where it could be best implemented as an analysis method. Destructive assay utilize techniques that result in destruction of the sample, often dissolving, separating and then analysis. Non-destructive techniques do not produce any chemical or physical changes to the sample. Two studies analyzed chemical changes in the ablation zone using powder XRD. These studies were inadequate since the penetration of the laser ablation was found to be only a few microns and is too small for powder XRD analysis. Ablation zone evaluation using SEM determined changes in the surface morphology including intergranular fractures within the grain boundaries of the ablated region. The volume of ablated material was estimated to be 4.5E-05 ± 2.25E-05 mm^3. Lastly chemical and thermodynamic properties of the materials were investigated to establish trends in laser power density needed to ablate elements of interest. This included measuring the heat capacity of $(U,Zr)O_2$, $(U,Ce)O_2$, $(U,Pu)O_2$, and $(U,Np)O_2$ prepared.

7.2 Introduction

The physical processes during the absorbance of laser light by a solid target are complex and not entirely understood (28). These processes are dependent on the laser properties as well as those of the solid. The sample is heated, melted, and evaporated at extremely high temperatures and pressures (3). The mass is then removed from the target in a mixture of molecules, atoms, vapor or large particulates. Incomplete vaporization of large particles results in elemental fractionation where the more refractory element is not completely vaporized in the plasma and is filtered in the mass spectrometer. For this reason it is crucial to determine the quantity of ablated mass and size distribution of particles in optimizing laser parameters for samples of interest.

Many mechanisms are used to describe mass removal of solids using laser ablation. Depending on the irradiance of the laser desorption, thermal vaporization, phase explosion and other mechanisms are proposed. If the irradiance is below 3×10^8 W/cm^2, desorption and thermal vaporization is the dominant processes (3). Laser desorption involves the absorbing of laser light with the upper layer of the material is vaporized and ionized. For the uranium oxides with plutonium, neptunium, cerium and zirconium materials examined in this work the laser power density varied from 31.821 to 114.592 Wcm^{-2}. This range suggests laser desorption mechanism. The removal of mass is dependent

on the melting point, boiling point, ionization potential, heat capacity, thermal conductivity, volatility, and reflectivity of the material (3, 21, 23, 28).

The purpose of this study is to classify LA-ICP-MS as either destructive or non-destructive and determine where it could be best implemented as an analysis method. Destructive assay result in dissolving the sample for quantitative analysis and are used at fuel fabrication plants as well as spent fuel recycling plants prior to separations (2). Non-destructive assay techniques do not produce any significant physical or chemical changes in the sample. These include gamma spectrometry and neutron counting as discussed in section 1.2 and are employed throughout the fuel cycle from enrichment plants to recycling plants (2). If the technique is non-destructive, then it could be used to determine the plutonium concentration in MOX fuel before irradiation at fuel fabrication plants. On the other hand, if it is destructive, then the technique would be better applied to safeguards to assist in determining used fuel burn-up rates, which can be indicative of weapons production.

Lastly chemical and thermodynamic properties of the materials were investigated to establish trends in laser power density needed to ablate elements of interest. This included measuring the heat capacity of the materials prepared. This will be a useful tool in determining laser power densities of the materials of interest.

7.3 Experimental

An important portion of this work is to quantify whether the method of analysis is destructive to the material. Physical changes in the material have been measured in previous work (23, 25, 28) but no chemical changes are reported. To address this variety of methods were examined to analyze any chemical changes in the material. Two methods with the same ablation conditions were examined to quantify chemical changes using 100% $^{238}UO_2$ and analyzed with powder XRD. The first method pressed a pellet with thickness less than 2 mm and sintered at 1700 °C under reducing atmosphere. The entire surface was then ablated at a rate of 100 μm sec^{-1} and pulse energy of 20 Hz. The average grain size was measured before and after ablation.

The second method ablated the surface of a green pellet. The top and bottom of the pellet was ablated then analyzed by powder XRD. The pellet was then ground and pressed again and ablated under the same conditions. This procedure was repeated for a total of three times.

The $(U,Zr)O_2$ pellets were used to measure the physical effects of the ablation process. After laser ablation sampling the pellets were carbon coated and analyzed on the SEM/EDS as described in section 2.2.3. This study examined the ablated area for physical defects in the material. Also an attempt to quantify the amount of material ablated during a line scan analysis was performed.

A quantum design model 6000 Physical Property Measurement System (PPMS) was used to determine the heat capacity of the materials. The data analysis is discussed in section 2.2.4. The sample mass required for analysis ranges from 20 to 50 mg. For each matrices tested the pellet was broken into small pieces with a mortar and pestle. The piece chosen for analysis needed to fall within the mass range as well as have a flat side to ensure proper contact between the sample and micro-calorimeter platform. If the sample coupling between the sample surface and micro-calorimeter platform fell below 90% the data was rejected and another set collected.

7.4 Results

7.4.1 Chemical changes due to ablation

The first method to determine chemical changes of the material using a thin sintered pellet ablated at a rate of 100 μm sec^{-1} and pulse energy of 20 Hz showed a reduction of grain size of material listed in Table 28, along with cylindrical formation on the surface (Figure 43). The powder XRD results showed no change in phases of the material due to ablation. However the x-rays penetrate farther into the sample than the ablated area and are not indicative of lack of surface chemical change.

Ablation	Average Grain Size (µm)
Before	10.34 ± 0.84
After	3.74 ± 0.21

Table 28: Average grain size of 100% UO_2 pellet before and after ablation measured using Leica DM 2500P Microscope

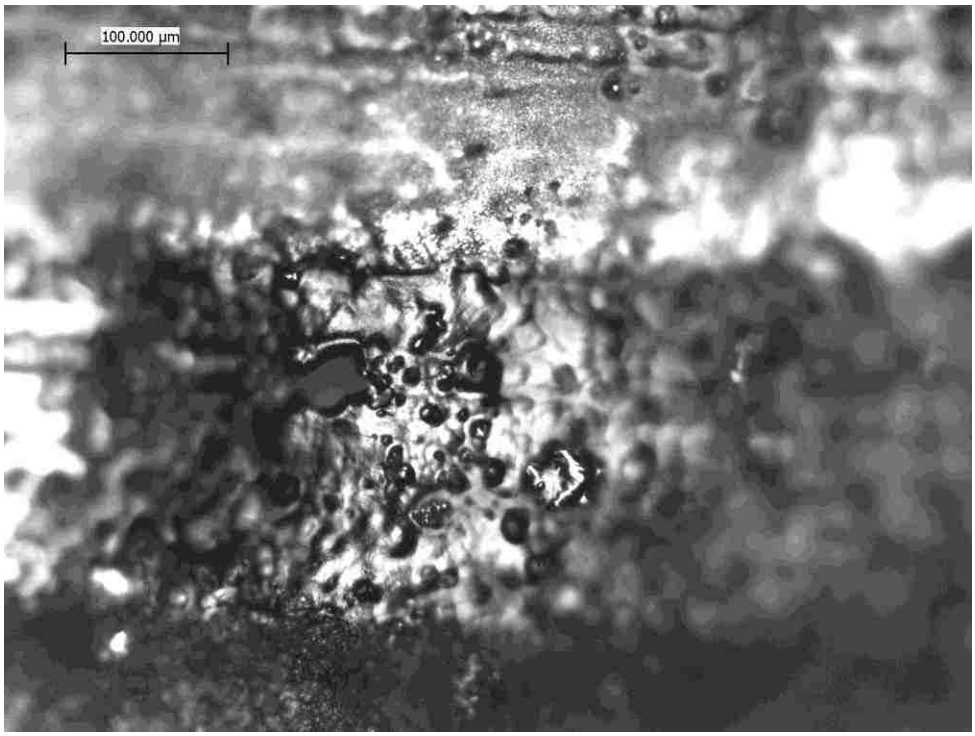

Figure 43: Effects of Laser on 100% UO_2 sintered pellet method 1

The second method ablated the surface of a green pellet. The top and bottom of the pellet was ablated then analyzed by powder XRD. The pellet was then ground and pressed again and ablated under the same conditions. This procedure was repeated for a total of three times resulting in some measurable differences in phases shown in Figure 44 and Figure 45. The measurable differences in phases cannot be deciphered as chemical changes at this time.

Since the geometry of the surface of the pellet and distance in mounting on clay changes between XRD analysis, this cannot be distinguished from chemical shifts in the pattern. The material is composed of two phases, Uraninite and $UO_{(2+x)}$. The reduction of the lattice parameter value indicates oxidation of the phase where the pattern shifts to the right. An increase of the lattice parameter value indicates a reduction of the phase and the pattern shifts to the left. These values are reported in Figure 45.

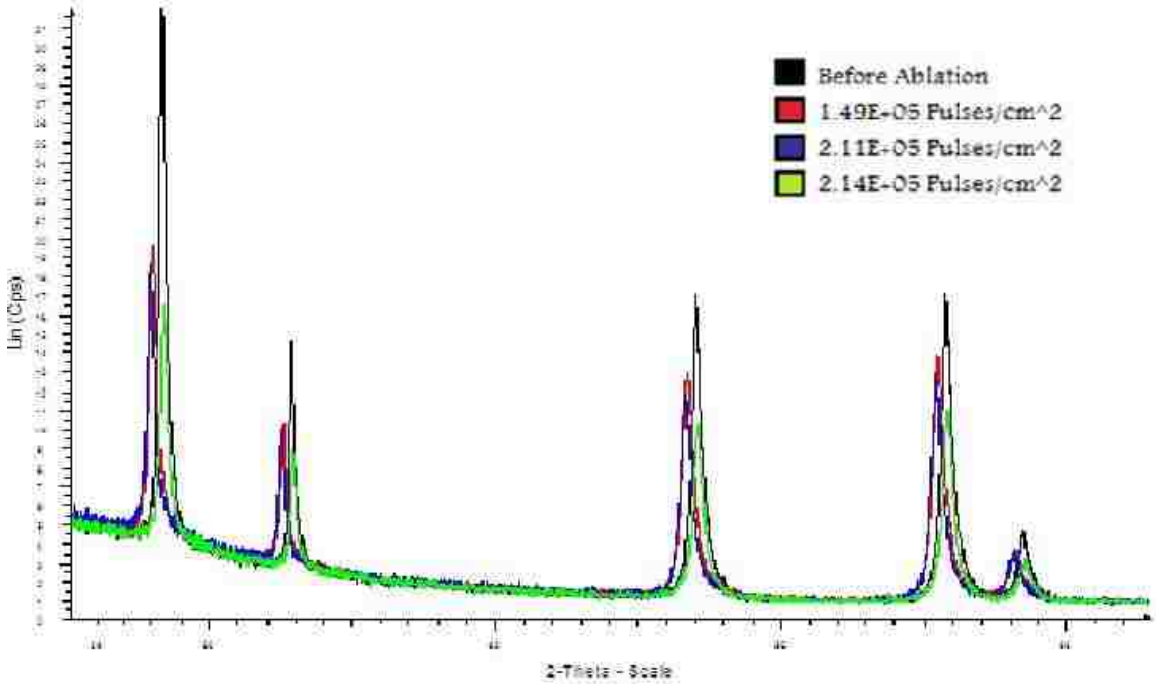

Figure 44: Comparison of XRD results of green pellet ablation study

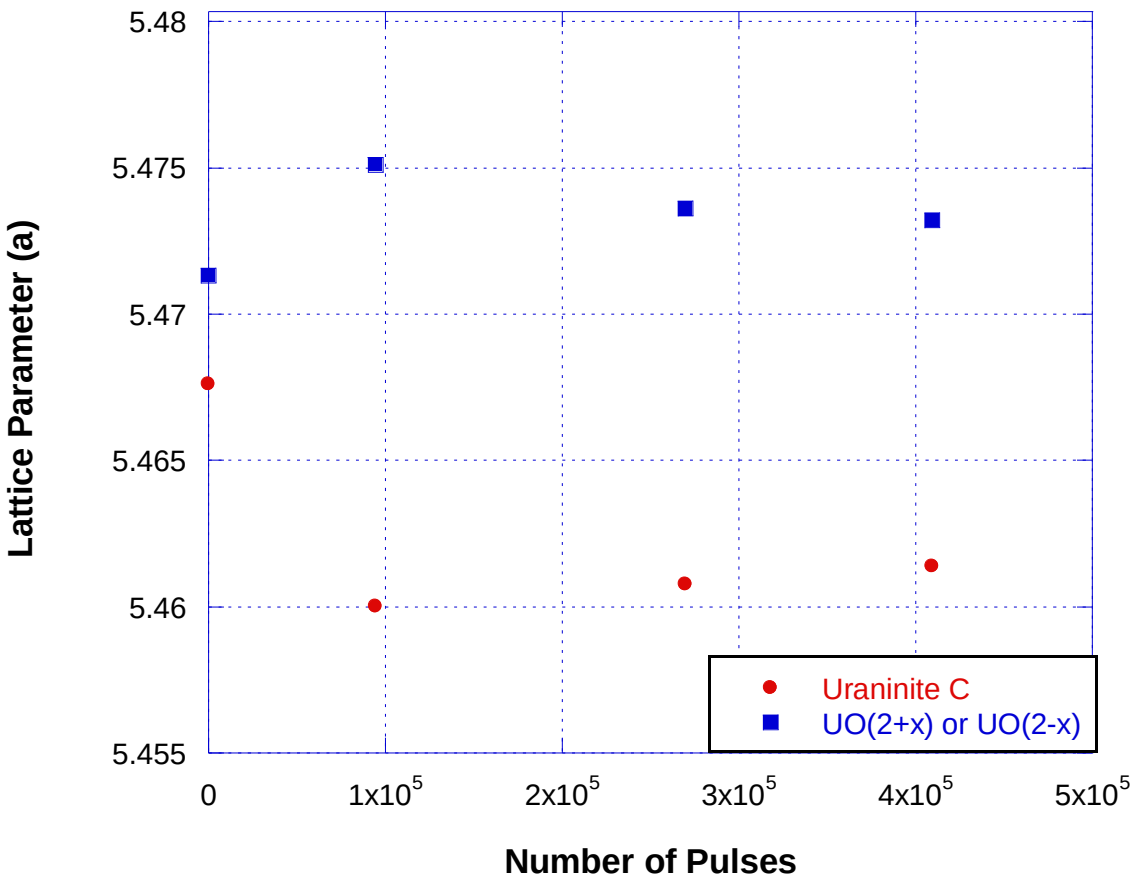

Figure 45: Lattice parameter changes with number of laser pulses with green pellet

The shifts shown in Figure 44 can be explained by geometry effects of the pellet and the detector. The geometry of the initial material was different than the ablated samples and is not a fair value to compare the ablated results to in Figure 45. There is a small shift at the lower 2 Theta that is not consistent throughout the scan (Figure 44). This is due to a change in geometry of the sample. The data suggests no change in material. We find the material is a mixture of UO_{2+x} and Uraninite where the x may be slightly changing. This would need to be verified using small angle grazing powder XRD.

7.4.2 Physical Changes

Analyzing the surface of the material after ablation lends insight into the amount of material ablated, surface morphology after ablation and efficiency of the vaporization process. Figure 46 is a back scatter image of the line scan sampling on a $(U,Ce)O_2$ pellet. The grain boundaries within the ablated area (highlighted by the red circle) are cracked and separated compared to the non-ablated area (highlighted by the yellow circle). This is evidence of intergranular fracture in the ablated area. Intergranular fractures could affect fuel performance if ablation is performed on fresh fuel, although the area affected is only 0.0225 mm^2 which would suggest minimum effect of fuel performance.

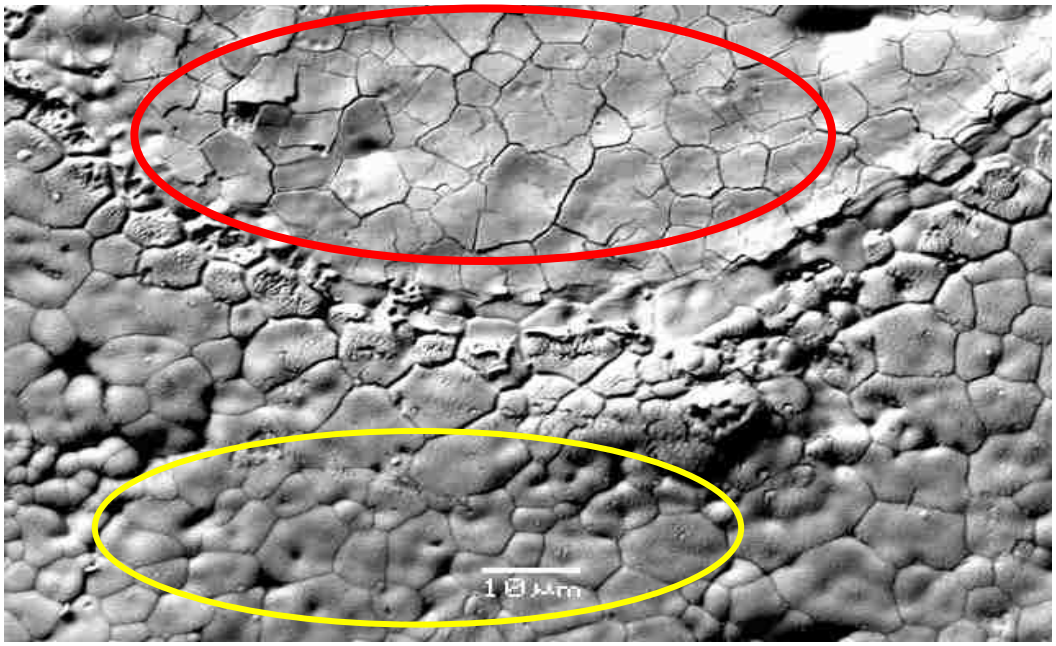

Figure 46: 1200x magnification back scatter image of the line scan

Figure 47 is the same image as Figure 46 in secondary electron mode on the SEM. This image clearly shows the depth of material ablated from the surface. It is estimated to be only a few microns. Using a depth estimate of 2 ± 1 μm, the overall volume of sample ablated is 4.5E-05 ± 2.25E-05 mm^3. These results show laser desorption as the mechanism for the ablation process since only a few micron layer of the material is vaporized and ionized (3).

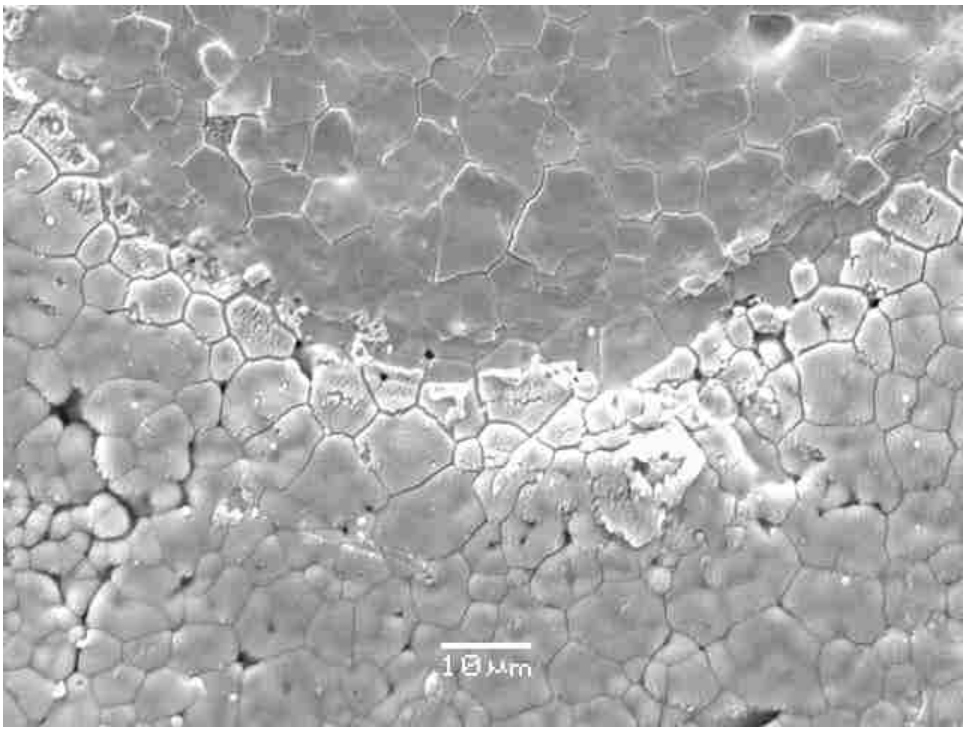

Figure 47: 1200x magnification secondary electron image of the line scan

Figure 48 is a back scatter image of the ablation zone of a $(U,Ce)O_2$ pellet. The ablation zone is highlighted with a blue square and is attributed to the shock wave of the laser as it interacts with the solid (28). The fracturing in this zone may be related to recrystallization of thin molten layers or stress during cooling (28). Outside of the ablation zone small spherical fragments of the ablated material have re-deposited onto the sample surface. This is indicative of the particles cooling before transport to the ICP-MS. These larger particles are clearly visible in the secondary electron image and highlighted with green circles (Figure 49).

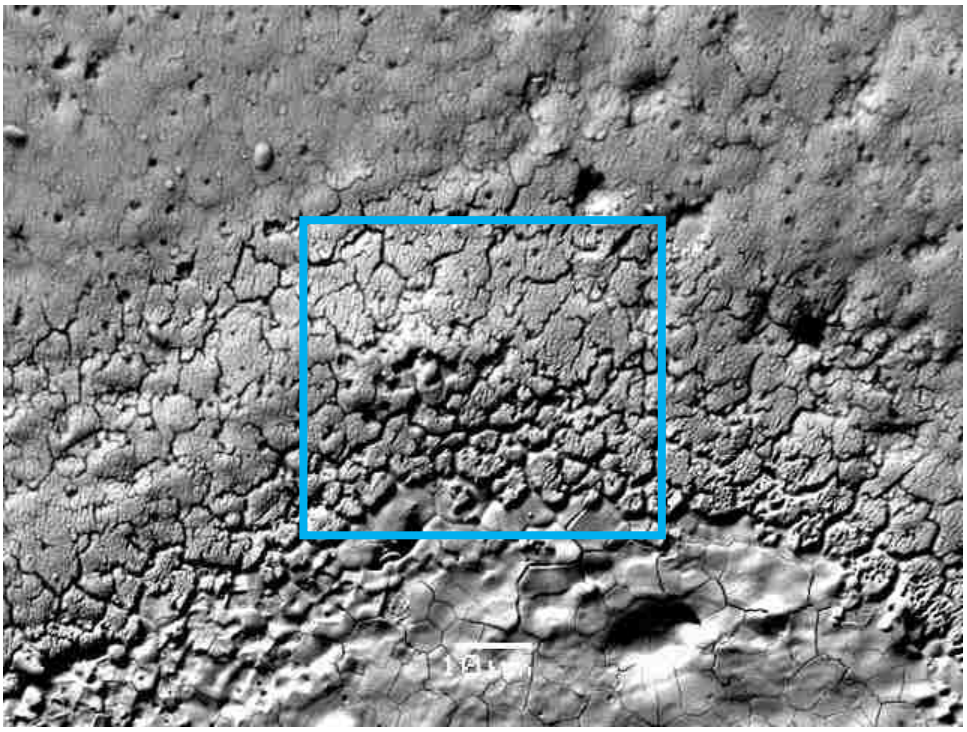

Figure 48: 1000x magnification back scatter image of the ablation zone

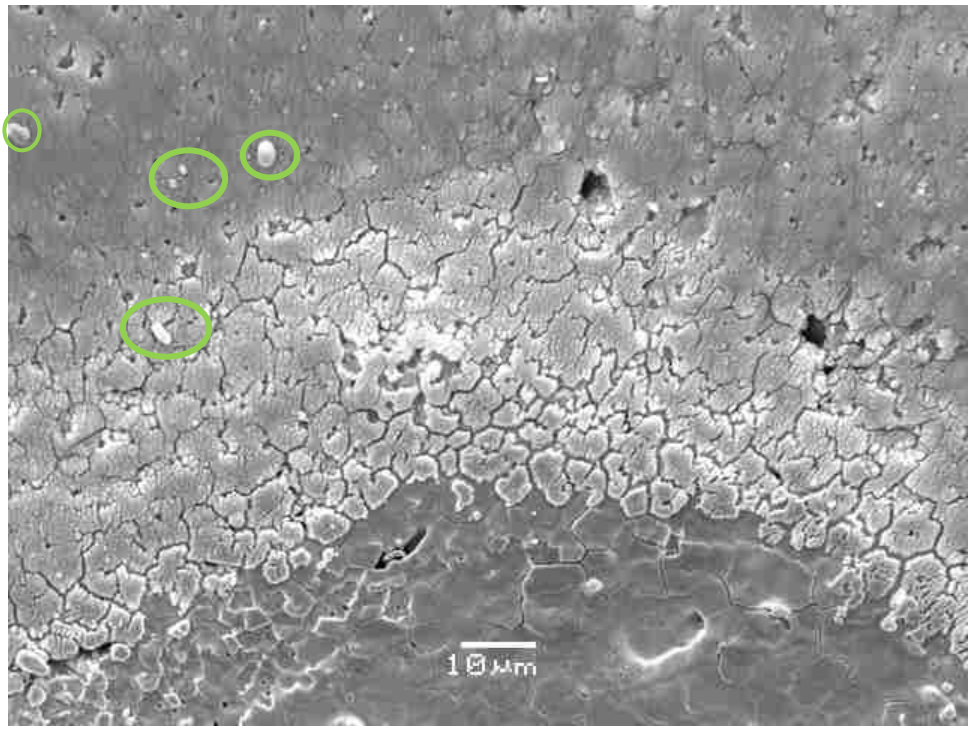

Figure 49: 1000x magnification secondary electron image of the ablation zone

7.4.3 Heat capacity measurements

Each matrix measured for heat capacity are compared to uranium dioxide measurements. The uranium dioxide values are in agreement with literature values reported at the temperatures evaluated (72, 74). Figure 50 shows the heat capacity results for 1, 5 and 10 mole % cerium in $(U,Ce)O_2$ matrices compared to uranium dioxide. The heat capacity value increases with decreasing cerium content. From 250-325 K 10 mole % cerium has heat capacity values below uranium dioxide and converges with uranium dioxide at 350 K. After 350 K the 10 mole % cerium heat capacity is slightly above uranium dioxide. The 1

mole % cerium has an average difference of 3.75 ± 0.44 $Jmol^{-1}K^{-1}$ above uranium dioxide across the temperatures measured. The 5 mole % cerium has an average difference of 2.77 ± 0.88 $Jmol^{-1}K^{-1}$ above uranium dioxide. This decrease in heat capacity with increasing cerium content was also observed by Krishnan et. al. (71). This is due to the fact that the heat capacity of uranium dioxide is higher than that of cerium dioxide.

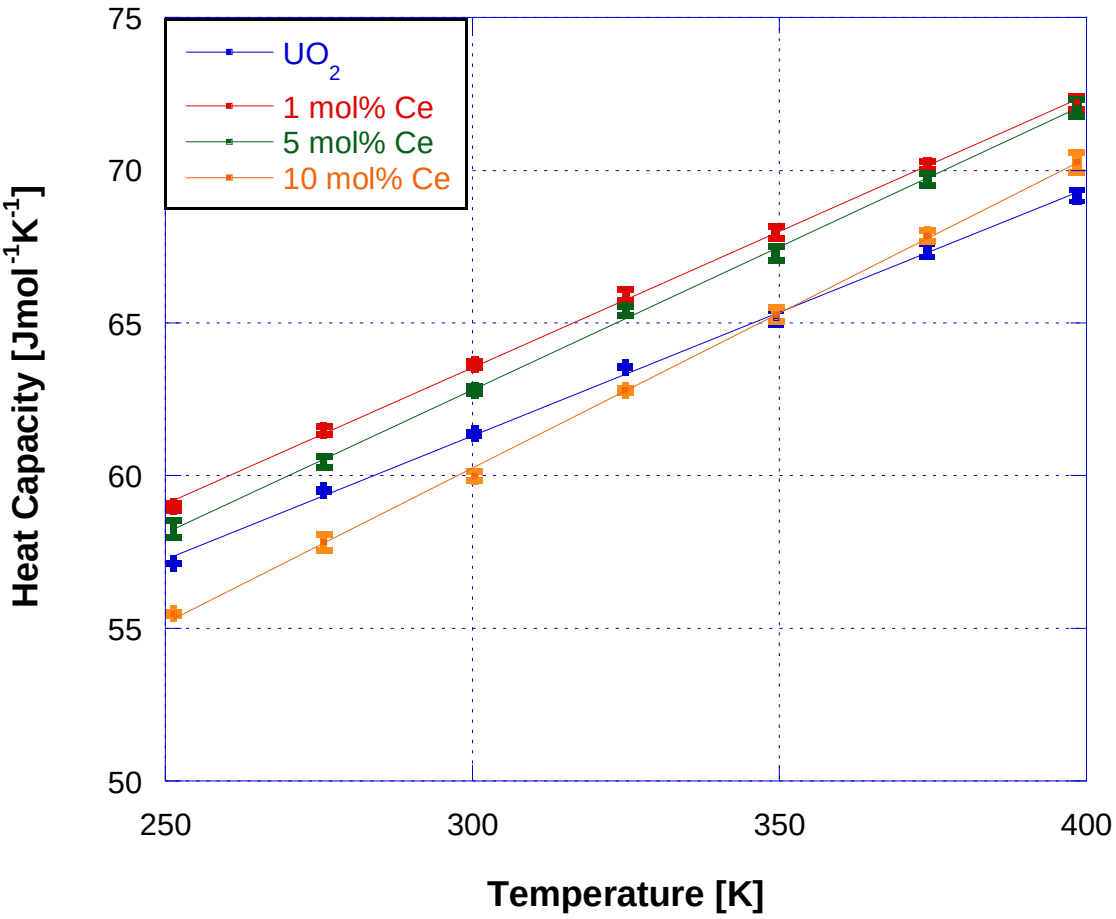

Figure 50: Heat capacity results for the $(U,Ce)O_2$ series compared to 100% UO_2

The 2.4 and 23.6 mole % zirconium heat capacity measurements compared to uranium dioxide are displayed in Figure 51. The difference between 2.4 mole % zirconium and uranium dioxide is 2.19 ± 0.41 $Jmol^{-1}K^{-1}$. The difference between 23.6 mole % zirconium and uranium dioxide is 4.89 ± 0.26 $Jmol^{-1}K^{-1}$. As the amount of zirconium in the sample increases the heat capacity value increases. Zirconium dioxide has the opposite effect of cerium dioxide in a uranium oxide matrix. Pure zirconium oxide heat capacity value at 298.15 K is found to be 56.5 $Jmol^{-1}K^{-1}$ which is less than the $(U,Zr)O_2$ matrices measured as well as the UO_2 sample (72).

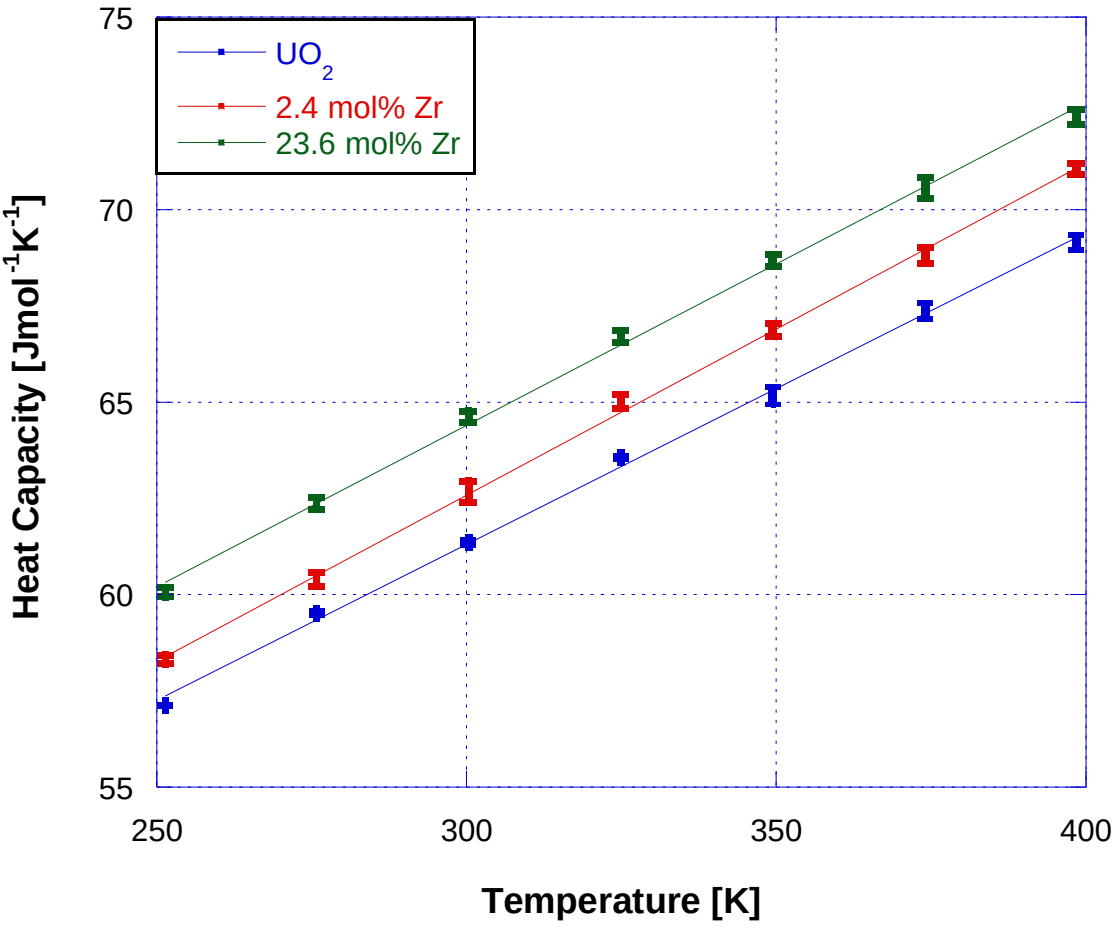

Figure 51: Heat capacity results for the $(U,Zr)O_2$ series compared to 100 % UO_2

Heat capacity results for the 0.5 and 1 mole % plutonium in $(U,Pu)O_2$ are shown in Figure 52. The 0.5 mole % plutonium heat capacity values are consistently below those of uranium dioxide with an average difference of -3.48 ± 0.20 $Jmol^{-1}K^{-1}$. The 1 mole % plutonium heat capacity values are continually above the uranium dioxide values with an average difference of 4.52 ± 0.53 $Jmol^{-1}K^{-1}$. Increasing the concentration of plutonium in $(U,Pu)O_2$ from 0.5 to 1.0 mole percent the heat capacity increases by an average 5.12 ± 0.77 $Jmol^{-1}K^{-1}$.

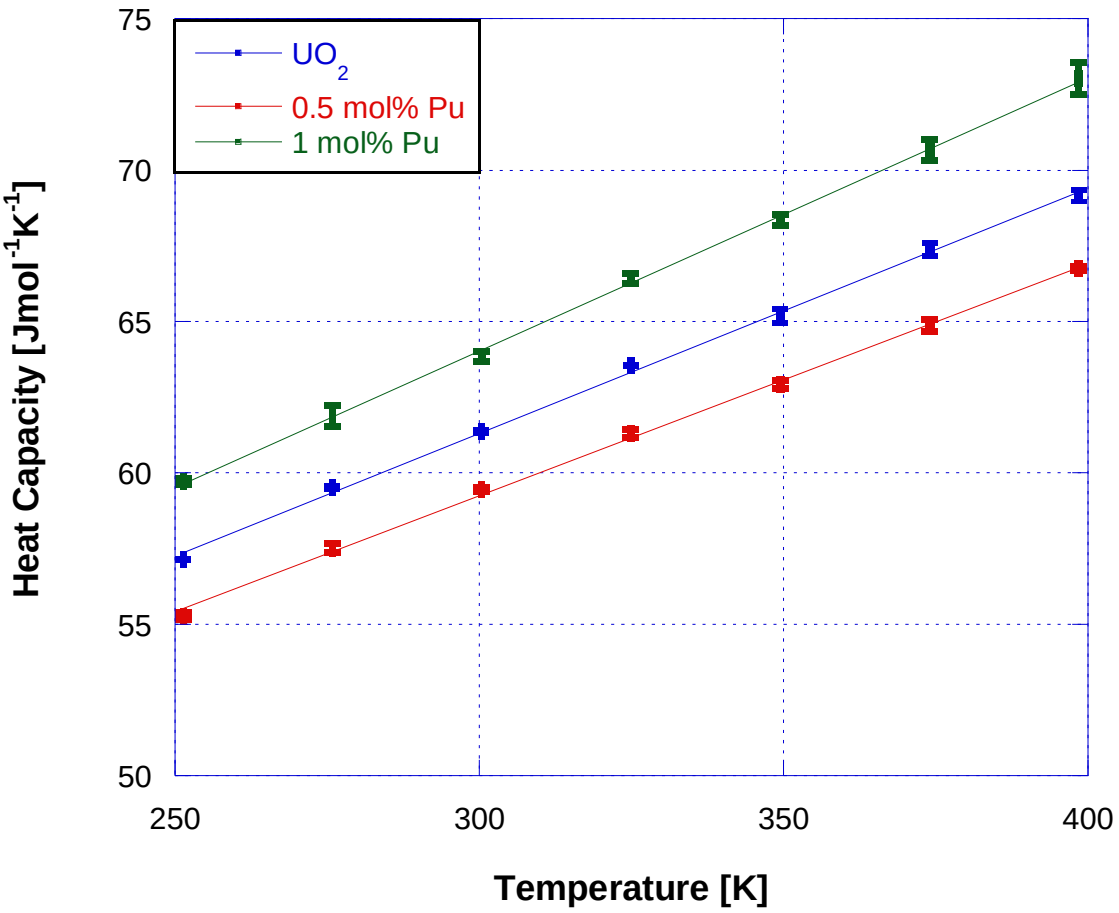

Figure 52: Heat capacity results for the $(U,Pu)O_2$ series compared to 100 % UO_2

The heat capacity for 0.25 and 1.25 mole % neptunium in a $(U,Np)O_2$ matrices compared to uranium dioxide are shown in Figure 53. The 0.25 mole % neptunium heat capacity values are within the error of the uranium dioxide values. This amount of neptunium has no effect on the heat capacity value. The 1.25 mole % neptunium heat capacity values increase compared to the uranium dioxide values with an average difference of 2.79 ± 0.23 $Jmol^{-1}K^{-1}$.

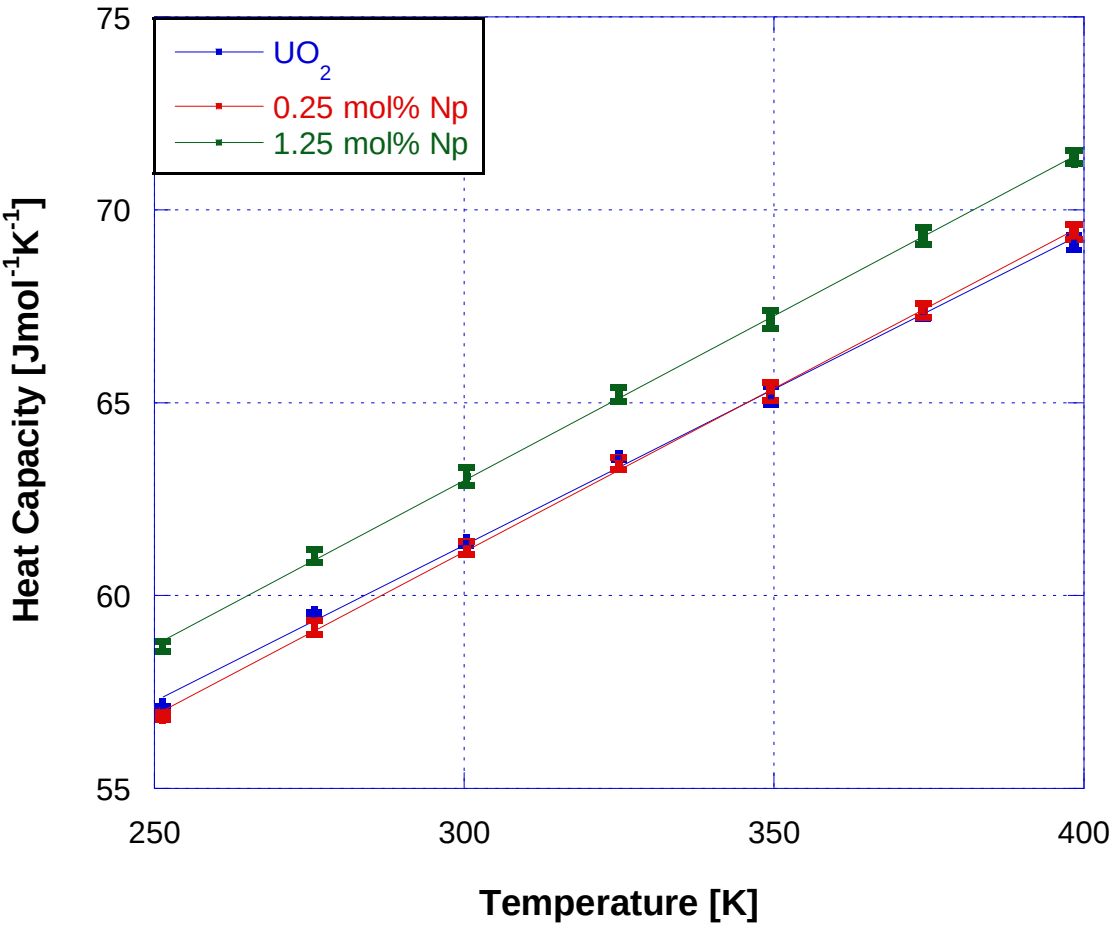

Figure 53: Heat capacity results for the $(U,Np)O_2$ series compared to 100 % UO_2

The laser temperature was calculated using the Stefan Boltzmann Law (Equation 6), which describes the power radiated from a black body in terms of temperature. Temperature (T) is raised to the 4^{th} power, the power (P) is the average power density applied to the surface in watts, the area ablated (A) is in cm^2. The emissivity (Ɛ) describes a body that does not absorb all incident radiation and emits less total energy than a black body. For simplicity the

emissivity value is equal to 1 for this calculation. The Stefan-Boltzmann constant (σ) or the constant of proportionality equals 5.67E-12 $Wcm^{-2}K^{-4}$.

$$T^4 = \frac{P}{A\mathcal{E}\sigma}$$

Equation 6: Stefan Boltzmann Law

The results of the Stefan Boltzmann law using the average power densities used for analysis are listed in Table 29. The temperature of the laser at the sample surface ranges from 1538 K to 2120 K. Unfortunately the PPMS cannot measure heat capacity above 400 K and extrapolation does not effectively predict actual heat capacity values. Heat capacity is dependent on phase relationships and lattice structures where a phase change is possible between 400 K and 2120 K for these materials. Figure 54 shows the heat capacity values for pure UO_2 from 250 K to 2900 K. Changes in the slope of the values indicate phase changes of the materials. Some groups have tried fitting with polynomial functions with success (71,72,74) but often need data points close to the phase transitions to account for steep slopes in heat capacity values. A study performed by Lucuta et. al. found that hyperstoichiometric UO_2 heat capacity values vary with oxygen potentials. As the oxygen potential increases the heat capacity values increase (73).

Matrices	Avg. Power Density [Wcm^{-2}]	Temperature [K]
$(U,Np)O_2$	31.821	1538
$(U,Pu)O_2$	38.197	1610
$(U,Ce)O_2$	85.944	1973
$(U,Zr)O_2$	114.592	2120

Table 29: Calculated temperatures of the laser at sample surface using Stefan Boltzmann Law

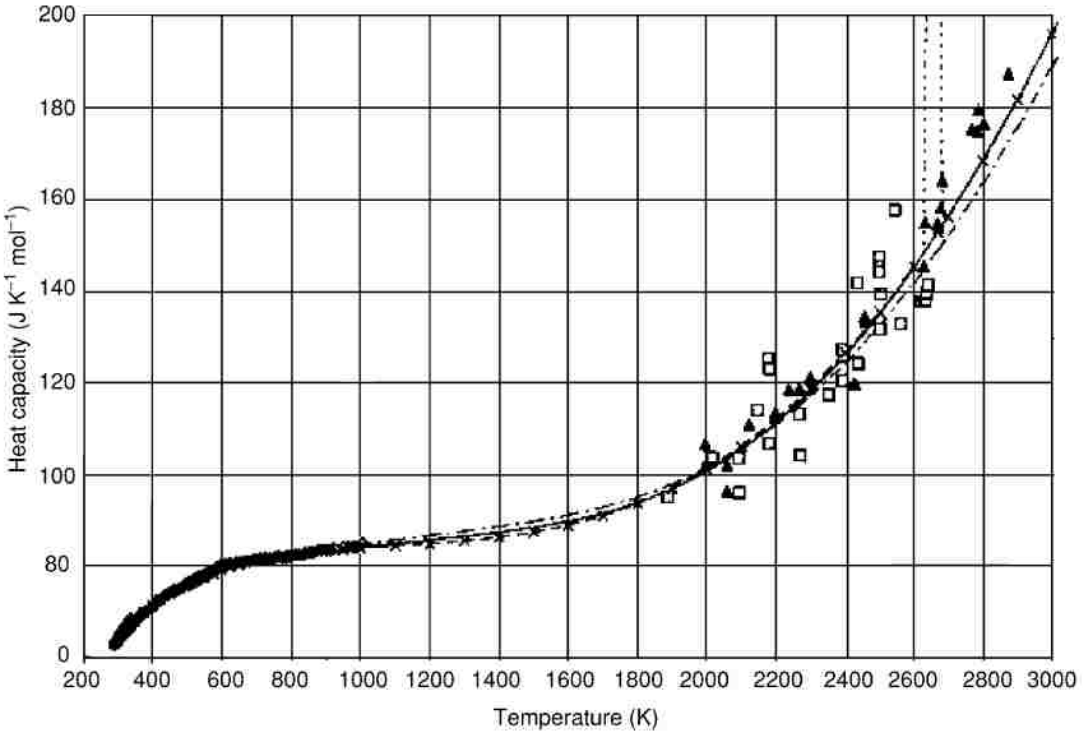

Figure 54: Heat capacity values for UO_2 from 250 K to 2900 K (74)

7.4.4 Thermodynamic model

The removal of mass during the laser ablation process is dependent on the melting point, boiling point, ionization potential, heat capacity, thermal conductivity, heat of vaporization, volativity, and reflectivity of the material (3, 21, 23, 28). Durant developed an equation to determine the time required for a sample to be raised to its vaporization temperature:

$$t_v = \pi K \rho C (T_v - T_0)^2 / 4P^2$$

Equation 7: Time required for vaporization (75)

Where K is the thermal conductivity, ρ is the sample mass density, C is the heat capacity, T_0 the initial temperature, T_v the sample vaporization temperature and P is the laser power density. Using this equation Durant concluded that different elements will vaporize at different rates. This has been visual verified in Figure 55. Cerium vaporizes and reaches the ICP-MS detector faster than zirconium in the (U,Zr,Ce)O_2 analysis seen in the difference in response time. The response times of three ablations per analyte are averaged in Table 30. The visual verification of zirconium and cerium differences in response, as well as the other analytes tested is confirmed. Although the rate of vaporization varies, the variation is not significant enough to pose a problem in the oxide matrices tested

as long as the integration is performed separately for each analyte and the counts are normalized by time of integration. The time corrections are applied to the quantitative analysis in this work, as described in section 2.2.2.

Element	**^{90}Zr**	**^{238}U**	**^{237}Np**	**^{239}Pu**	**^{140}Ce**
Response Time (s)	11.264 ± 0.064	12.914 ± 0.127	10.861 ± 0.277	11.187 ± 0.131	11.091 ± 0.119

Table 30: Response time of elements tested

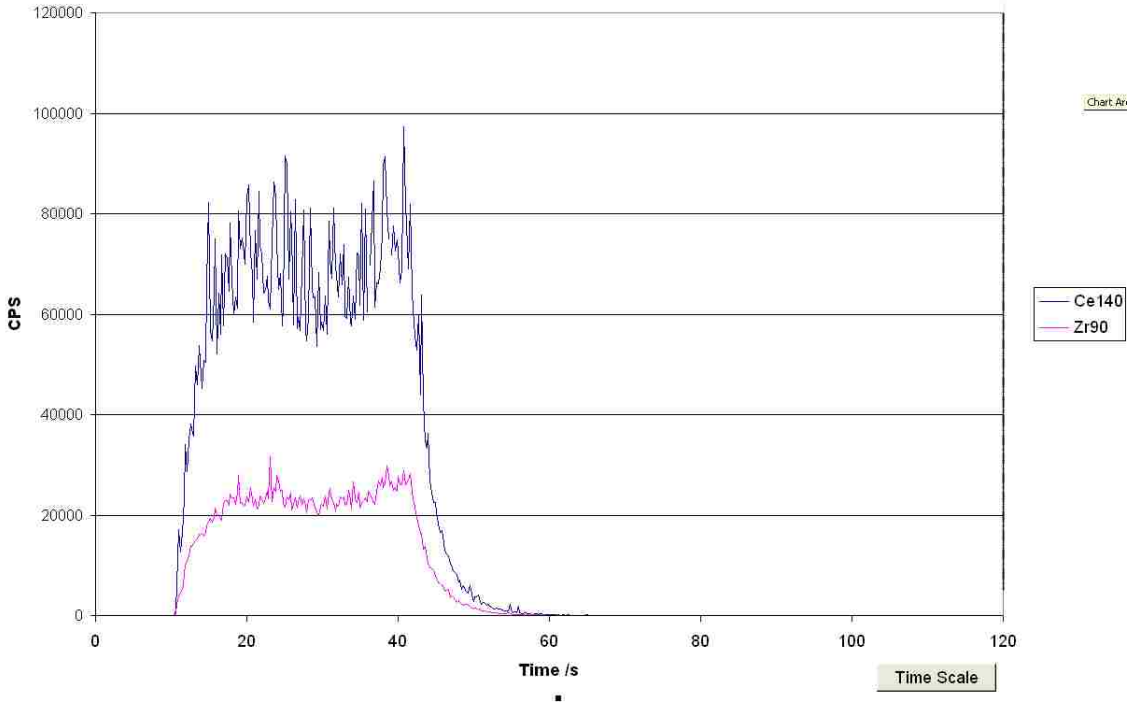

Figure 55: Response time of ^{140}Ce and ^{90}Zr laser ablation signals

Heat capacity and thermal conductivity are functions of temperature. In order to use these terms to determine a thermodynamic model, computer modeling would need to be used to ensure the laser temperature, heat capacity and thermal conductivity values converge and are optimized. To avoid this circular logic to determine a thermodynamic model, this section will look at trends within the known values of chemical or thermodynamic properties of cerium dioxide, zirconium dioxide, neptunium dioxide and plutonium dioxide shown in Table 31.

Matrices	1st Ionization Potential [eV]	Melting Point [K]	Boiling Point [K]
NpO_2	6.33 ± 0.18	2873	unknown
PuO_2	7.03 ± 0.12	2673	3073
CeO_2	9.7 ± 0.5	2873	3773
ZrO_2	9.4 ± 0.2	2125	4650

Table 31: Chemical and thermodynamic properties of materials (60, 76, 77, 78, 79, 80, 81)

The melting points of the examined oxides value from 2125-2873 K, no trends could be observed between the melting point and ablation laser temperature. All of the boiling points for the oxides are known except for neptunium. The remaining three boiling points are correlated with Stefan Boltzmann equation with a linear correlation value of 0.9101 (Figure 56). Cerium dioxide falls below the trend with a laser temperature of 1973 K and boiling point temperature of 3773 K. In order for a complete trend to be established, further

studies are needed with known boiling point values and optimization of LA-ICP-MS of the element of interest.

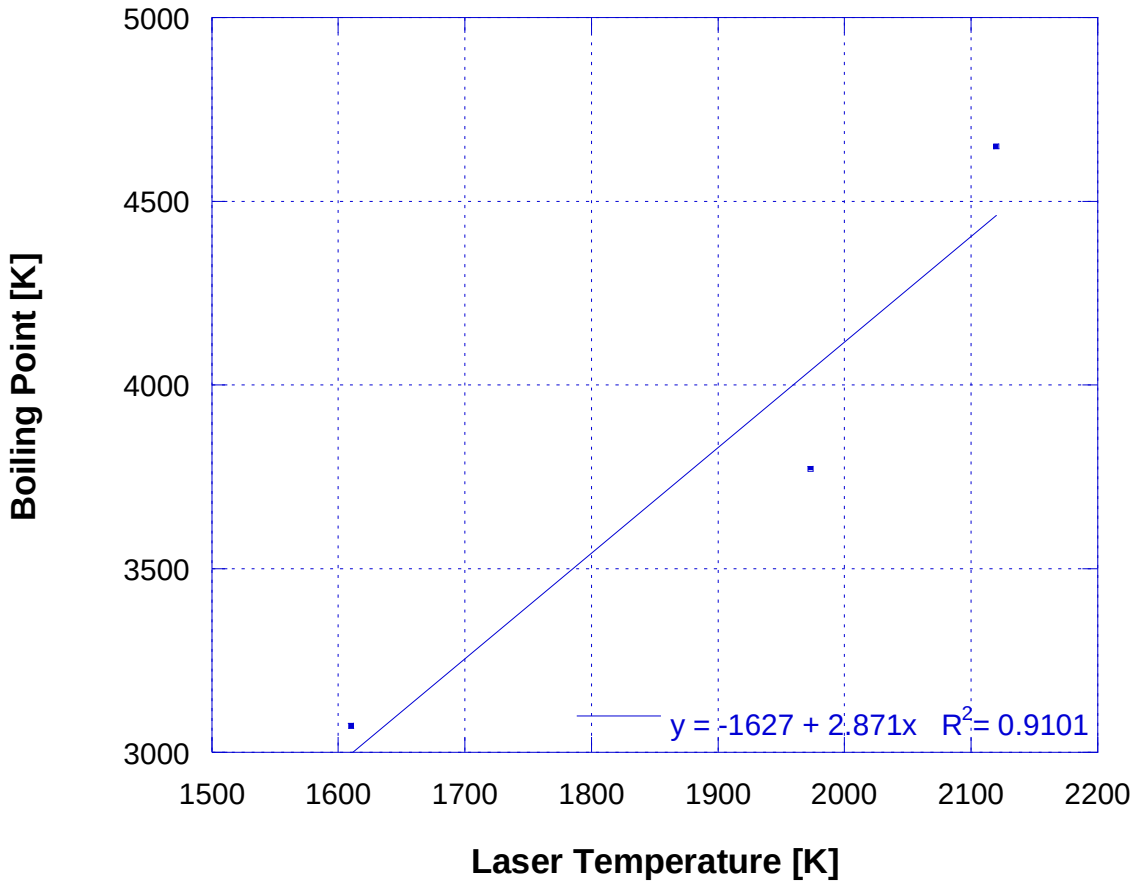

Figure 56: Boiling point of oxides versus laser temperature

The first ionization potentials for the examined oxides have been measured in the literature and are plotted against laser temperature using the Stefan Boltzmann equation (Figure 57). The linear correlation value for this relationship is 0.9155. The cerium oxide ionization potential is high compared

and the zirconium oxide ionization potential is low compared to the optimized laser temperature. Although the trend is not entirely linear, this could be used as a starting reference point for future oxides of interest. For instance, if the 1st ionization potential for the oxide of interest is 8 eV, the user would use a laser temperature of 1800 K as a starting point with further optimization.

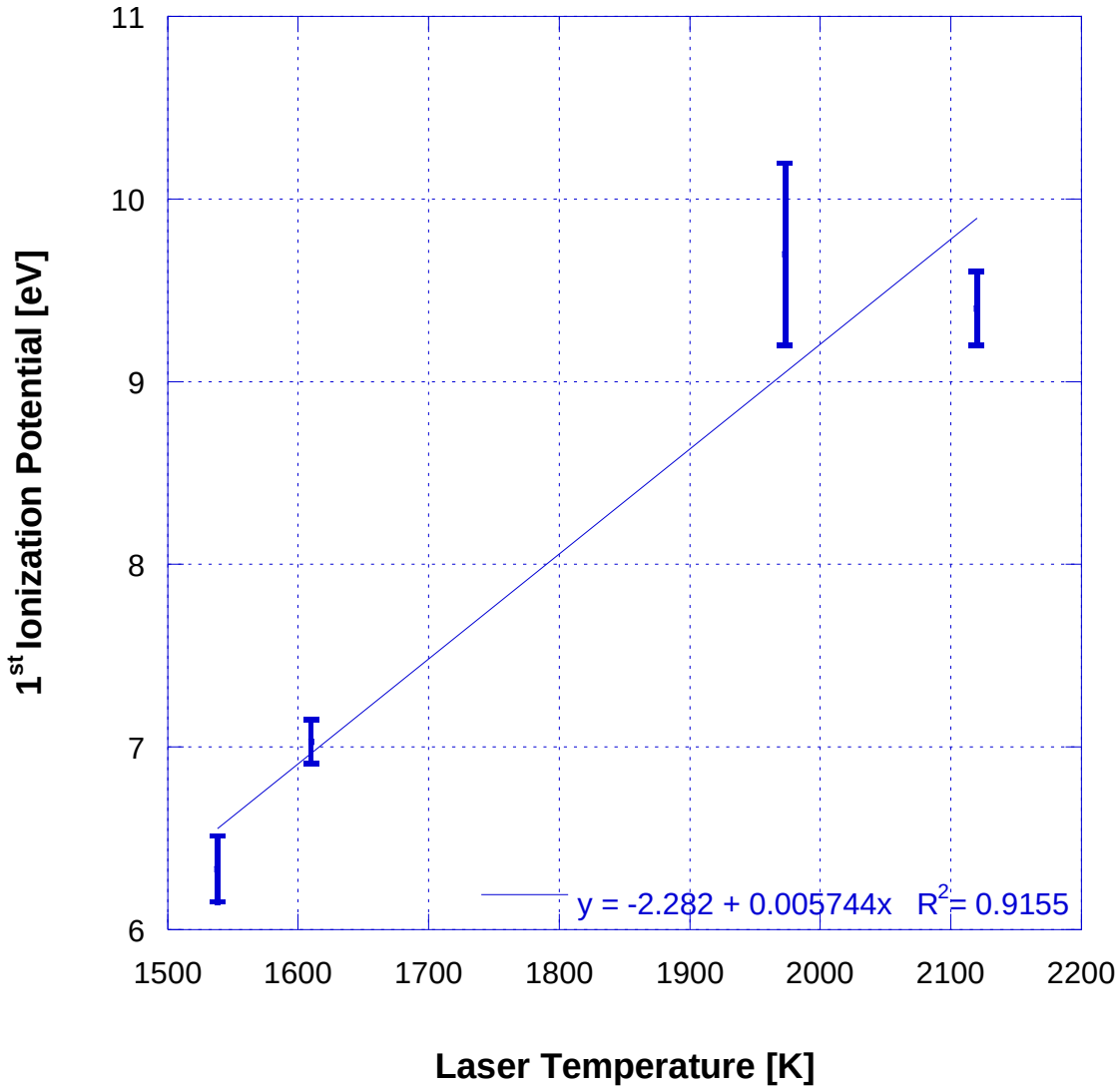

Figure 57: 1st ionization potential of oxides versus laser temperature

7.5 Conclusion

The first method to determine chemical changes of the material using a thin sintered pellet ablated at a rate of 100 μm sec^{-1} and pulse energy of 20 Hz showed a reduction of grain size of material, along with cylindrical formation on the surface. The powder XRD results showed no change in phases of the material due to ablation. However this is x-rays penetrating farther into the sample than the ablated area and not indicative of lack of chemical change due to sampling. The second method ablated the surface of a green pellet. The top and bottom of the pellet was ablated then analyzed by powder XRD. The pellet was then ground and pressed again and ablated under the same conditions. This procedure was repeated for a total of three times resulting in some measurable differences in phases. The measurable differences in phases cannot be deciphered as chemical changes at this time. Since the geometry of the surface of the pellet and distance in mounting on clay changes between XRD analysis, this cannot be distinguished from chemical shifts in the pattern.

The powder XRD results showed no change in phases of the material due to ablation. However this method has x-rays penetrating farther into the sample than the ablated area and the results are not indicative of lack of chemical change due to sampling. Further studies are needed to quantify the change in x for the UO_{2+x} species. A suitable method would be small angle grazing to emphasize surface changes.

Analyzing the surface of the material after ablation lends insight into the amount of material ablated, surface morphology after ablation and efficiency of the vaporization process. The grain boundaries within the ablated area are cracked and separated compared to the non-ablated area. This is evidence of intergranular fracture in the ablated area. Intergranular fractures could affect fuel performance if ablation is performed on fresh fuel, although the area affected is only 0.0225 mm^2. The depth of material ablated from the surface is estimated to be only a few microns. Using a depth estimate of 2 ± 1 μm, the overall volume of sample ablated is 4.5E-05 ± 2.25E-05 mm^3. Since the area ablated is insignificant compared to the bulk material, this technique could be used at a fuel fabrication facility to measure plutonium concentrations in MOX fuel.

The fracturing in the ablated zone may be related to recrystallization of thin molten layers or stress during cooling. Outside of the ablation zone small spherical fragments of the ablated material have re-deposited onto the sample surface. This is indicative of the larger particles cooling before transport to the ICP-MS. The size and shape of the fragments indicate soft ablation that is ideal for quantitative analysis.

Heat capacity measurements were successfully measured using a PPMS Quantum Design model 6000. The temperature measured ranged from 250 K to 400 K. The heat capacity value for $(U,Ce)O_2$ decreased with increasing cerium content from 1 to 10 mole % cerium. The heat capacity value for $(U,Zr)O_2$

increases as the amount of zirconium in the sample increases. The difference between 23.6 mole % zirconium and UO_2 is 4.89 ± 0.26 $Jmol^{-1}K^{-1}$. For the $(U,Pu)O_2$ series, the 0.5 mole % plutonium heat capacity values are consistently below the uranium dioxide values with an average difference of -3.48 ± 0.20 $Jmol^{-1}K^{-1}$. The 1 mole % plutonium heat capacity values are continually above the uranium dioxide values with an average difference of 4.52 ± 0.53 $Jmol^{-1}K^{-1}$. By increasing the concentration of plutonium in $(U,Pu)O_2$ from 0.5 to 1.0 mole % the heat capacity values increases by an average 5.12 ± 0.77 $Jmol^{-1}K^{-1}$. The 0.25 mole % neptunium heat capacity values are within the error of the uranium dioxide measurements. The 1.25 mole % neptunium heat capacity values increase compared to the uranium dioxide values with an average difference of 2.79 ± 0.23 $Jmol^{-1}K^{-1}$. Using the Stefan Boltzmann Law and solving for the temperature of the laser at the sample surface ranges from 1538 K to 2120 K. Unfortunately the PPMS cannot measure heat capacity above 400 K and extrapolation does not effectively predict actual heat capacity values. Heat capacity is dependent on phase relationships and lattice structures where a phase change is possible between 400 K and 2120 K for these materials.

Trends were established between laser temperature and boiling point and first ionization potentials of the evaluated materials. These trends cannot be translated to generalized matrices since LA-ICP-MS is a matrix dependent technique. The trends could be used as starting point for optimization of laser

parameters in a uranium oxide matrix. Further studies of oxides would be needed to establish linearity greater than 0.91 correlations.

Chapter 8 – Conclusions and Recommendations

The goal of this project was to develop and optimize LA-ICP-MS techniques for the analysis of fuel, used fuel, and waste forms. Actinide oxide materials and standards were prepared and characterized. The characterization included physical, thermodynamic, and chemical properties. The methods developed for the LA-ICP-MS analysis were evaluated for limit of detection, accuracy, and precision. The ablation zone was examined for chemical or physical changes in the material. Lastly, trends correlating the ablation behavior of the elements evaluated with physical and thermodynamic properties of the materials were assessed.

8.1 Preparation of materials

The first task was to prepare actinide oxide materials as standards for LA-ICP-MS. These materials were binary oxides consisting of bulk uranium with zirconium, cerium, neptunium and plutonium to best model used nuclear fuel. More complex materials such as a ternary oxide matrix of bulk uranium with zirconium and cerium were also prepared. The physical properties of the materials characterized include theoretical density and average grain sizes. Lastly, the phase composition of the materials was characterized.

The autoclave synthesis of NpO_2 in 8 M nitric acid effectively converted all the material to Np(VI) as confirmed by UV-Vis spectroscopy and LSC. The co-precipitation of uranium and plutonium using 2 mL of ammonium hydroxide saturated with oxalate precipitated 99.4 % of the metals in solution with contact time of 10 minutes. The co-precipitation method for synthesizing the binary and ternary oxides was successful in producing solid solutions of each matrix. The $(U,Pu)O_2$ pellets prepared were highly crystalline, single face centered cubic phase verifying the sintering profile of 5 hours at 1700 °C was sufficient. Longer sintering times or an added annealing step after sintering would produce a single solid solution for each matrices than the two solid solutions measured for both $(U,Zr)O_2$ and $(U,Zr,Ce)O_2$ pellets. The $(U,Np)O_2$ and $(U,Ce)O_2$ contained a solid solution phase and a uraninite phase, these matrices would also need longer sintering times or annealing in order for the cerium and neptunium to diffuse throughout the material producing one solid solution phase.

The average theoretical densities for the materials are listed in Table 32. The highest theoretical densities were the $(U,Np)O_2$ and $(U,Pu)O_2$. These matrices were freeze dried after precipitation rather than oven dried at 100 °C and ball milled. The freeze drying method produced particle sizes that were ideal for sintering. The lowest theoretical densities contained zirconium and were the $(U,Zr)O_2$ and $(U,Zr,Ce)O_2$. This could be due the small ionic radius of zirconium (72 pm) compare to the other elements in the matrices (83). The pellets with zirconium are more porous and had physical defects in the materials such as

lateral cracks observed. The lateral cracks most likely occurred during the pellet pressing stage.

Matrices	Avg % Theoretical ρ
$(U,Ce)O_2$	87.30 ± 9.67
$(U,Zr)O_2$	82.67 ± 6.69
$(U,Zr,Ce)O_2$	76.84 ± 3.55
$(U,Np)O_2$	88.33 ± 2.16
$(U,Pu)O_2$	87.55 ± 4.48

Table 32: Average % Theoretical Densities for all matrices

8.2 LA-ICP-MS methods

The second task was to determine the LOD, accuracy, and precision for the LA-ICP-MS methods developed as well as any limitations of this technique. The system was optimized using loops in the transport tube to limit elemental fractionation. Having loops in the transport tube successfully filtered the larger ablated particles from the untreated $(U,Ce)O_2$ surface. The smaller ablated particles reached the plasma of the ICP-MS for detection. By increasing the amount of loops in the transport tube the accuracy of the measurements considerably improved from a linear correlation value of 0.9756 to 0.9997.

All of the studies optimizing one element produced linear correlation values above 0.99 (Table 33) when using two loops in the transport tube. The

concentration range of zirconium from 2.4 to 23.6 mole percent is the widest tested that resulted in an acceptable linear correlation value. The average power density needed to ablate zirconium is higher than the other elements in this work, suggesting zirconium oxide needs more energy to vaporize than cerium, uranium, neptunium or plutonium oxides. When optimizing laser conditions for two different elements, loss of accuracy in the linear correlation value is observed. This is due to the laser power density difference needed to ablate cerium and zirconium. The average laser power density for the analysis of both elements fell between the optimization values for either element, but skewed to the higher value in order to ablate zirconium successfully.

Matrices	**Linear Correlation**	**%RSD**
$(U,Ce)O_2$	0.9997	12.4-20.8
$(U,Zr)O_2$	0.9963	8.0-14.0
$(U,Np)O_2$	0.995	3.9-8.9
$(U,Pu)O_2$	0.9992	3.7-9.6
$(U,Zr,Ce)O_2$ Zr	0.9795	6.8-20.9
$(U,Zr,Ce)O_2$ Ce	0.985	5.2-22.9

Table 33: Linear correlation values and %RSD for all the matrices

The change in precision within the measurements using the loops as a filtration system was not as noticeable with only a few percent gained with the average relative standard deviations within the series. The porosity of the material affects the precision of the laser ablation measurements resulting in

high relative standard deviation for this series. These physical features of the materials may be a limiting factor to achieve relative standard deviations less than 10%.

Two saturation studies with a uranium source were completed to understand spectroscopic interferences. It was found using helium as the carrier gas the $^{239}Pu/^{238}U$ ratio ranged from 8.53E-05 to 1.27E-04. The significantly higher $^{239}Pu/^{238}U$ ratio using helium as the carrier gas is not peak tailing but $^{238}UH^{+}$ formations confirmed by a mass scan survey. The KED mode successfully lowered the $^{239}Pu/^{238}U$ ratio to the range of 2.77E-05 to 2.85E-05, also lowering the ^{238}U signal to 1.6E06. The mass scan survey showed a second peak forming at the m/z 239.052 which suggests a hydride is still reaching the detector. To limit the hydride formation assuming the hydrogen source is from the He carrier gas, argon was used where the $^{239}Pu/^{238}U$ ratio ranged from 6.46E-05 to 8.77E-05. These results are closer to the carry over observed with the $^{237}Np/^{238}U$ ratio on the ELAN DRC II system.

The difference in carry over can be explained by where the quadrupole in assigning the channel for measurement. If the channel is to the left of the peak maximum the carry over counts will be +1 amu. If the channel is to the right of the peak maximum, the carry over counts will be -1 amu. The relationship increases with increasing laser power density due to the relationship with power density and signal intensity. As signal intensity increases the broadening increases.

Each series was measured and analyzed under an hour, which suggests a rapid analytical technique compared to current methods used to quantify plutonium and neptunium in a uranium matrix. Laser Ablation-Inductively Couple Plasma-Mass Spectrometry also minimizes the handling of potentially hazardous material and reduces waste generation by directly ablating the solid. This technique could be applied to fresh or used fuel to quantify plutonium and neptunium for safeguards or forensic purposes.

8.3 Ablation Zone

The third task was to examine the ablation zone for any chemical or physical changes. Overall the methods failed to show significant chemical changes in the material. The thin sintered pellet ablated indicated small changes in the lattice parameters due to a change in geometry of the sample. The data suggests no change in material. It is found the material is a mixture of UO_{2+x} and Uraninite. Further studies are needed to quantify the change in x for UO_{2+x}. Small angle XRD would be ideal for studies on the material. This type of analysis is needed as the effects of the laser ablation only appear to be on the surface of the material.

Analyzing the surface of the material after ablation lends insight into the amount of material ablated, changes in surface morphology and efficiency of the vaporization process. The grain boundaries within the ablated area are cracked

and separated compared to the non-ablated area. This is evidence of intergranular fracture in the ablated area. Intergranular fractures could affect fuel performance if ablation is performed on fresh fuel, although the area affected is only 0.0225 mm^2. Since the area ablated is insignificant compared to the bulk material, this technique could be used at a fuel fabrication facility to measure plutonium concentrations in MOX fuel.

The depth of material ablated from the surface is estimated to be only a few microns. Using a depth estimate of 2 ± 1 μm, the overall volume of sample ablated is 4.5E-05 ± 2.25E-05 mm^3. The fracturing in the ablated zone may be related to recrystallization of thin molten layers or stress during cooling. Outside of the ablation zone small spherical fragments of the ablated material have re-deposited onto the sample surface. This is indicative of the larger particles cooling before transport to the ICP-MS. The size and shape of the fragments indicate soft ablation that is ideal for quantitative analysis.

Since the damage to the surface is minimal the technique could be classified as semi destructive. Further studies are needed to determine if the intergranular fractures disrupt fuel performance. Irradiation of the ablated material would verify if the technique could be used to determine the plutonium concentration in MOX fuel before irradiation. This technique could also be applied to safeguards to assist in determining used fuel burn-up rates, which can be indicative of weapons production.

8.4 Thermodynamic model

The final task was to develop a model to correlate the ablation behavior of the elements tested with physical and thermodynamic properties of the materials. Trends were established between laser temperature and boiling point of the oxides as well as first ionization potential of the oxide of interest in a uranium dioxide matrix. These trends cannot be translated to any matrices other than uranium dioxide since LA-ICP-MS is a matrix dependent technique. The trends could be used as starting point for optimization of laser parameters in a uranium oxide matrix. Further studies of oxides would be needed to establish linearity greater than 0.91 correlations.

The next element of interest is neodymium in a uranium dioxide matrix. Neodymium has a +3 oxidation state in uranium dioxide and is a burn up indicator as described in section 1.3. Comparing the direct solid state analysis of neodymium using LA-ICP-MS with the Nd-148 method is of great interest. The challenge would be that the 148 m/z channel has interferences with $^{132}Ba^{16}O$ and ^{148}Sm. This can be overcome by comparing the ^{148}Nd with the ^{145}Nd m/z channel which has no mass interferences (82).

References

[1] IAEA 2002. IAEA Safeguards Glossary 2001 Edition. International Nuclear Verification Series No. 3. IAEA Printing Office in Vienna.

[2] IAEA 2011. Safeguards Techniques and Equipment: 2011 Edition. IAEA Printing Office in Vienna.

[3] Mokgalaka NS, Torresdey JL. 2006. Laser Ablation Inductively Coupled Plasma Mass Spectrometry: Principles and Applications. Applied Spectroscopy Reviews. 41:131-150.

[4] Gastel M, Becker JS, Kuppers G, Dietze H-J. 1997. Determination of long-lived radionuclides in concrete matrix by laser ablation inductively coupled plasma mass spectrometry. Spectrochimica Acta Part B. 52(14):2051-2059.

[5] DeVol TA, Ringberg AH, Dewberry RA. 2002. Isotopic analysis of plutonium using a combination of alpha and internal conversion electron spectroscopy. J. Radioanal Nucl Chem. 254(1):71-79.

[6] Loveland WD, Morrissey DJ, Seaborg GT. 2005. Modern Nuclear Chemistry. USA: John Wiley & Sons.

[7] Burkes DE, Fielding RS, Porter DL, Meyer MK, Makenas BJ. 2009. A US perspective on fast reactor fuel fabrication technology and experience. Part II: Ceramic fuels. J. Nuclear Materials. 393:1-11.

[8] Nakamura A, Fujino T. 1987. Thermodynamic study of UO_{2+x} by solid state emf technique. J. Nuclear Materials. 149:80-100.

[9] Schleifer F, Naoumidis A, Nickel H. 1983. Thermodynamics on uranium dioxide-zirconium oxide-lanthanide oxide (LnO2-x) solid solutions. J. Nuclear Materials 1983 115(2-3):143-158.

[10] Kleykamp H. 1985. The chemical state of the fission products in oxide fuels. J. Nuclear Materials. 131(2-3): 221-246.

[11] Schleifer F, Naoumidis A, Nickel H. 1981. Solid solutions and phase equilibriums in (uranium, zirconium, lanthanide) oxides in the temperature range 1270-1670 K. J. Nuclear Materials. 101(1-2):150-161.

[12] Kinoshita H, Uno M, Yamanaka S. 2004. Stability evaluation of fluorite structure phases in ZrO_2-MO_2 (M = Th, U, Pu, Ce) systems by thermodynamic modeling. J. Alloys and Compounds. 370:25-30.

[13] Kleykamp H, Paschoal JO, Pejsa R, Thommler F. 1985. Composition and structure of fission product precipitates in irradiated oxide fuels: correlation with phase studies in the molybdenum-ruthenium-rhodium-palladium and barium oxide-uranium dioxide-zirconium dioxide-molybdenum dioxide systems. J. Nuclear Materials. 130:426-433.

[14] ASTM E321-96. 2012. Standard Test Method for Atom Percent Fission in Uranium and Plutonium Fuel (Neodymium-148 Method). ASTM International: West Conshohocken, PA.

[15] Moody KJ, Hutcheon ID, Grant PM. 2005. Nuclear Forensic Analysis. Boca Raton FL: CRC Press.

[16] Wlader AJ, Abell ID, Platzner I. 1993. Lead isotopic ratio measurement of NIST 610 glass by laser ablation-inductively coupled plasma-mass spectrometry. Spectrochimica Acta. 48B(3):397-402.

[17] Sylvester PJ. 2005. Laser Ablation ICP-MS Developments and Trends for 2003. Geostandards and GeoAnalytical Research. 29(1):41-52.

[18] Gruen DM. 1992. Transuranium Elements; A Half Century. Washington DC: American Chemical Society.

[19] Gray AL. Solid sample introduction by laser ablation for inductively coupled plasma source mass spectrometry. Analyst. 110:551-556.

[20] Gunther D, Horn I, Hattendorf B. 2000. Recent trends and developments in laser ablation-ICP-mass spectrometry. J Anal Chem. 368:4-14.

[21] Arrowsmith P, Hughes SK. 1988. Entrainment and transport of laser ablated plumes for subsequent elemental analysis. Appl. Spectroscopy Reviews. 42(7): 1231-1239.

[22] Heinrich CA, Pettke T, Halter WE, Aigner-Torres M, Audetat A, Gunther D, Hattendorf B, Bleiner D, Giullong M, Horn I. 2003. Quantitative multi-element analysis of minerals, fluid and melt inclusions by laser-ablation inductively-coupled-plasma mass-spectrometry. Geochimica et Cosmochimica Acta. 67(18): 3473-3496.

[23] Darke SA, Tyson JF. 1993. Interaction of laser radiation with solid materials and its significance to analytical spectrometry. A review. J. Anal. Atomic Spec. 8:145-209.

[24] Skoog D, Holler F. 2006. Principles of Instrumental Analysis, 6th ed. Canada: Thomson Learning.

[25] Russo RE, Mao X, Liu H, Gonzalez J, Mao SS. 2002. Laser ablation in analytical chemistry – a review. Talanta. 57:425-451.

[26] Guillong M, Gunther D. 2002. Effect of particle size distribution on ICP-induced elemental fractionation in laser ablation-inductively coupled plasma-mass spectrometry. J. Anal. At. Spectrom. 17:831–837.

[27] Horn I, Gunther D. 2003. The influence of ablation carrier gasses Ar, He and Ne on the particle size distribution and transport efficiencies of laser ablation-induced aerosols: implication for LA-ICP-MS. Applied Surface Science. 207:144–157.

[28] Mank AJG, Mason PD. 1999. A critical assessment of laser ablation ICP-MS as an analytical tool for depth analysis in silica-based glass samples. J. Anal. At. Spectrom. 14:1143-1153.

[29] Miliszkiewicz N, Walas S, Tobiasz A. 2015. Current approaches to calibration of LA-ICP-MS analysis. Anal. At. Spectrom. 30:327-338.

[30] Becker SJ. 2005. Recent developments in isotope analysis by advanced mass spectrometric techniques. J. Anal. At. Spectrom. 20:1173-1184.

[31] Storey CD, Smith MP, Jeffries TE. 2007. In situ LA-ICP-MS U-Pb dating of metavolcanics of Norrbotten, Sweden: Records of extended geological histories in complex titanite grains. Chemical Geology. 240(1-2):163-181.

[32] Jeffries TE, Jackson SE, Longerich HP. 1998. Application of a frequency quintupled Nd:YAG source (λ=213 nm) for laser ablation inductively coupled plasma mass spectrometric analysis of minerals. J. Anal. At. Spectrom. 13:935-940.

[33] Becker SJ, Dietze H-J. 1999. Determination of trace elements in geological samples by laser ablation inductively coupled plasma mass spectrometry. Fresenius J. Anal. Chem. 365(5):429-434.

[34] Becker SJ, Pickhardt C, Dietze H-J. 2000. Laser ablation inductively coupled plasma mass spectrometry for the trace, ultratrace and isotope analysis of long-lived radionuclides in solid samples. International J. of Mass Spec. 202(1-3):283-297.

[35] Leloup C, Marty P, Dall'ava D, Perdereau M. 1997. Quantitative Analysis for Impurities in Uranium by Laser Ablation Inductively Coupled Plasma Mass SpectrometryL Improvements in the Experimental Setup. J. Anal. Atomic Spec. 12:945-950.

[36] Palmer RA, Smith H, Smith G, Smith M, Russell R, Patello G. 2001. Chemical and Physical Characterization of the First West Valley Demonstration Project Hight-Level Waste Feed Batch. In Smoth GL, Sundaram SK, Spearing DR editors. Environmental Issues and Waste Management Technologies VII Proceedings of the symposium held at the 103rd Annual Meeting of The American Ceramic Society. Ceramic Transactions, Vol 132.

[37] Alexander ML, Smith MR, Hartman JS, Mendoza A, Koppenaal DW. 1998. Laser ablation inductively coupled plasma mass spectrometry. Applied Surface Science 127-129:255-261.

[38] Ha YK, Kim J, Jeon YS, Han SH, Seo HS, Song K. 2010. Local burnup characteristic of PWR spent nuclear fuels discharged from Yeonggwang-2 nuclear power plant. Nucl. Eng. And Tech. 42(1):79-88.

[39] Ha YK, Kim JG, Park YS, Park SD, Song K. 2011. Behaviors of molybdenum in UO_2 fuel matrix. Nucl. Eng. And Tech. 43(3):309-316.

[40] Horvath M, Guillong M, Izmer A, Kivel N, Restani R, Gunther-Leopold I, Coutureau JO, Hellwig C, Gunther D. 2007. Analysis of Xenon Gas Inclusion in Nuclear Fuel using Laser Ablation ICP-MS. J. Anal. At. Spectrom. 22(10):1266–1274.

[41] Koo YH, Oh J-Y, Lee B-H, Sohn D-S. 2003. Three-Dimensional Simulation of Threshold Porosity for Fission Gas Release in the Rim Region of LWR UO_2 Fuel. J. Nuclear Materials. 321:249-255.

[42] U. S. Joint Working Group of the American Physical Society and the American Association for the Advancement of Science. 2008. Nuclear Forensics: Role, State of the Art, and Program Needs. Printed in the United States of America ISBN 978-0-87168-722-7.

[43] Varga Z. 2008. Application of laser ablation inductively coupled plasma mass spectrometry for the isotopic analysis of single uranium particles. Analytica Chimica Acta. 625:1-7.

[44] Cizdziel JV, Ketterer ME, Farmer D, Faller SH, Hodge VF. 2008. ^{239,240,241}Pu fingerprinting of plutonium in western US soils using ICPMS: solution and laser ablation measurements. Anal Bioanal Chem. 390(2):521-522.

[45] Cagno S, Hellemans K, Lind OC, Skipperud LL, Janssens K, Salbu B. 2014. LA-ICP-MS for Pu source identification at Mayak PA, the Urals, Russia. Environ. Sci.: Processes Impacts.16:306-312.

[46] Lee JS, Lim HB. 2014. Improvement of Signal Stability by a Cyclone-type Particle Separator for Cermaic Analysis using Laser Ablation ICP-MS. Bull. Korean Chem. Soc. 35(8):2555-2558.

[47] Guillong M, Kuhn H-R, Gunther D. 2003. Application of a particle separation device to reduce inductively coupled plasma-enhanced elemental fractionation in laser ablation-inductively coupled plasma-mass spectrometry. Spectrochimica Acta Part B. 58(2):211-220.

[48] Venkata Krishnan R, Panneerselvam G, Singh BM, Kothandaraman B, Jogeswararao G, Antony MP, Nagarajan K. 2011. Synthesis, characterization and thermal expansion measurements on uranium-cerium mixed oxides. J. Nuclear Materials. 414(3):393-398.

[49] Dorr W, Hellmann S, Mages G. 1986. Study of the formation of UO_2-PuO_2 solid solution by means of UO_2-CeO_2 simulate. J. Nuclear Materials 140(1):7-10.
[50] Plaue J. 2013. Forensic Signatures of Chemical Process History in Uranium Oxides [dissertation].University of Nevada Las Vegas.

[51] Neeb KH. 1997. The Radiochemistry of Nuclear Power Plants with Light Water Reactors. NY: Walter de Gruyter.

[52] Nagayama K, Utsunomiya Y, Kajiwara T, Nishiyama T. 2011. Pulse Laser Ablation by Reflection of Laser Pulse at Interface of Transparent Materials. In: Jakubczak K editor. Lasers - Applications in Science and Industry. INTECH.

[53] Raith A, Hutton RC, Abell ID, Crighton J. 1995. Non-destructive sampling method of metals and alloys for laser ablation-inductively coupled plasma mass spectrometry. J. Anal. At. Spectrom. 10:591-594.

[54] Vais V, Li C, Cornett J. 2004. Preventing uranium hydride formation in standard uranium samples for determination of ^{239}Pu by ICP-MS. J. Anal. At. Spectrom. 19:1281–1283.

[55] Boulyga SF. Becker JS. 2001. Determination of uranium isotopic composition and ^{236}U content of soil samples and hot particles using inductively coupled plasma mass spectrometry. Fresenius J Anal Chem. 370:612–617.

[56] Gunther-Leopold I, Kivel N, Kobler Waldis J, Wernli B. 2008. Characterization of nuclear fuels by ICP mass-spectrometric techniques. Anal Bioanal Chem 390:503–510.

[57] Bagnall KW, Laidler JB. 1964. Neptunium and plutonium trioxide hydrates. J. Chem. Soc. 2693-6.

[58] Richter K, Sari C. 1987. Phase relationships in the neptunium-oxygen system. J. Nuclear Materials. 148:266-71.

[59] Dukes EK, Shuler WE. 1960. Report DP-543 Declassified. Dupont de Nemours Co.

[60] Wick OJ. 1980. Plutonium Handbook. La Grange Park, Ill.: American Nuclear Soc.

[61] Fultz B, Howe J. 2013. Transmission Electron Microscopy and Diffractometry of Materials. Heidelberg New York Dordrecht London: Springer.

[62] Whitmarsh CL. 1962. Review of Zircaloy-2 and Zircaloy-4 Properties Relevant to N. S. Savannah Reactor Design, Oak Ridge National Laboratory Report No. ORNL-3281, UC-80-Reactor Technology. TID-4500 (17th ed.).

[63] Nikulina AV, Markelov VA, Peregud MM. 1996. Zirconium alloy E635 as a material for fuel rod cladding and other components of VVER and RBMK cores. United States: American Society for Testing and Materials, West Conshohocken, PA.

[64] Yamanaka S, Tsujimoto K, Yamanaka T, Uno M, Miyake M, Katsura M. 1997. High-temperature reaction of $(U,Gd)O_2$ with zirconium. J. Nuclear Materials. 247: 252-257.

[65] Miyake M, Katsura M, Yamanaka S. 1988. A study of the reaction between UO_2 and Zr. J. Nuclear Materials. 154(1):123-127.

[66] Gong W, Lutze W, Ewing R. 2000. Zirconia ceramics for excess weapons plutonium waste. J. Nuclear Materials. 277:239-249.

[67] De Lima NB, Imakuma K. 1985. X-ray diffraction study of the formation of solid solutions in urania-thoria prepared by aqueous chemical processes. J. Nuclear Materials. 135:215-221.

[68] Das P, Choudhury R. 1992. Formation of peripheral porosity regions around urania in zirconia-urania mixed oxide powder compact sintering. J. Nuclear Materials. 187:272-277.

[69] Kohl F, Jakubowski N, Brandt R, Pilger C, Broekaert JAC. 1997. New strategies for trace analyses of ZrO_2 SiC and Al_2O_3 ceramic powders. Fresenius J. Anal. Chem. 359(4-5):317-325.

[70] Kennedy T, Hampshire S, Yaginuma Y. 1997. A Study of the Compaction Mechanism of Granulated Materials. J. European Ceramic Soc. 17:133-139.

[71] Krishnan RV, Nagarajan K. 2006. Heat capacity measurements on uranium-cerium mixed oxides by differential scanning calorimetry. Thermochimica Acta 440:141-145.

[72] Chen M, Hallstedt B, Gauckler LJ. 2004. Thermodynamic modeling of the ZrO_2-$YO_{1.5}$ system. Solid State Ionics. 170(3-4):255-274.

[73] Lucuta PG, Matzke H, Verrall RA. 1995. Thermal conductivity of hyperstoichiometric SIMFUEL. J. Nuclear Materials. 223:51-60.

[74] Fink JK. 1982. Enthalpy and heat capacity of the actinide oxides. Int'l J. of Thermophysics. 3(2):165-200.

[75] Durrant S. 1999. Laser ablation inductively coupled plasma mass spectrometry: achievements, problems, prospects. J. Anal. At. Spectrom. 14:1385-1403.

[76] Infante I, Kovacs A, La Macchia G, Rehaman A, Shahi M, Gibson JK, Gagliardi L. 2010. Ionization Energies for the Actinide Mono- and Dioxides Series, from Th to Cm: Theory versus Experiment. J. Phys. Chem. A. 114:6007–6015.

[77] Piacente V, Bardi G, Maraspina L, Desideri A. 1973. Dissociation energy of CeO_2 and Ce_2O_2 molecules. J. Chem. Phys. 59(31).

[78] Bohler R, Welland MJ, De Bruycker F, Boboridis K, Janssen A, Eloirdi R, Konings RJM, Manara D. 2012. Revisiting the melting temperature of NpO_2 and the challenges associated with high temperature actinide compound measurements. J. Applied Physics, 2012 111:113501.

[79] Murad E, Hildenbrand DL. 1975. Thermochemical properties of gaseous ZrO and ZrO_2. J. Chem. Phys. 63:1133.

[80] Nielsen R. 2000. Zirconium and Zirconium Compounds. Ullmann's Encyclopedia of Industrial Chemistry. Wiley Online Library.

[81] Capriotti L, Quaini A, Bohler R, Boboridis K, Luzzi L, Manara D. 2014. A laser heating study of the CeO_2 solid/liquid transition: challenges related to a refractory compound with a very high oxygen pressure. High Temperatures-High Pressures. 44:69–82.

[82] Kim JS, Jeon YS, Park SD, Han SH, Kim JG. 2007. Burnup Determination of High Burnup and Dry Processed Fuels Based on Isotope Dilution Mass Spectrometric Measurements. J. Nucl. Science and Tech. 44(7):1015-1023.

[83] Shannon, RD. 1976. Revised Effective Ionic Radii and Systematic Studies of Interatomic Distances in Halides and Chalcogenides. Acta. Cryst. A32(5): 751-767.

Curriculum Vitae

Graduate College
University of Nevada, Las Vegas

Keri Rachel Campbell

Degrees:
Bachelors of Science, Chemistry, 2009
University of Nevada, Las Vegas

Publications:

Campbell, Keri; Unger, Aaron; Rhoads, Zachary; Bertoia, Julie; Hartmann, Thomas; Czerwinski, Ken *Laser Ablation ICP-MS of (U,Pu)O2 as a Simulated Used Nuclear Fuel* Journal of Analytical Atomic Spectrometry. Submitted for review manuscript ID: JA-ART-04-2015-000117

Campbell, Keri; Bertoia, Julie; Hartmann, Thomas; Czerwinski, Ken *Minimizing elemental fractionation effects for analysis of uranium oxide materials, (U,Ce)O2 using LA-ICP-MS* Journal of Analytical Atomic Spectrometry. Submitted for review manuscript ID: JA-ART-03-2015-000103

Paviet-Hartmann, Patricia; Riddle, Catherine; Campbell, Keri; Mausolf, Edward *Overview of reductants utilized in nuclear fuel reprocessing /recycling* International Nuclear Fuel Cycle Conference, Salt Lake City, UT, United States, (2013) 1, 79-86.

Paviet-Hartmann, Patricia; Wright, Amber; Mausolf, Edward; Campbell, Keri; Poineau, Frederic *Application of formohydroxamic acid in nuclear processing: synthesis and complexation with technetium-99* International Conference on Nuclear Engineering, Proceedings, 18th, Xi'an, China, (2011) 1, 387-391.

Dissertation Title: Laser Ablation ICP-MS of Actinide Oxides as Simulated Used Nuclear Fuels

Dissertation Examination Committee:

Chairperson, Kenneth R. Czerwinski, Ph.D.
Committee Member, Patricia Paviet, Ph.D.
Committee Member, Peter Stark, Ph.D.
Committee Member, Gary Cerefice, Ph.D.
Graduate Faculty Representative, William Culbreth, Ph.D.